Karlsruhe Institute of Technology

Faculty of Physics
Institute of Nuclear Physics

Investigation of background processes of ions and Rydberg atoms in the KATRIN spectrometers

Master thesis
of

Woo-Jeong Baek

at the Institute of Nuclear Physics

Reviewer:	Prof. Dr. G. Drexlin
Second Reviewer:	Prof. Dr. U. Husemann
Advisor:	Dr. Florian Fränkle

15.11.2016 – 14.11.2017

Erklärung zur Selbstständigkeit

Ich versichere, dass ich diese Arbeit selbstständig verfasst habe und keine anderen als die angegebenen Quellen und Hilfsmittel benutzt habe, die wörtlich oder inhaltlich übernommenen Stellen als solche kenntlich gemacht und die Satzung des KIT zur Sicherung guter wissenschaftlicher Praxis in der gültigen Fassung vom 17.05.2010 beachtet habe.

Karlsruhe, den 14.11.2017, _____

Woo-Jeong Baek

Als Ansichtsexemplar genehmigt von

Karlsruhe, den 14.11.2017, _____

Prof. Dr. G. Drexlin

Abstract

This work focuses on the investigation of background processes induced by ions and Rydberg atoms in the spectrometers of the KArlsruhe TRitium Neutrino (KATRIN) experiment. A detailed understanding of the origins as well as the evolvement of such processes is mandatory for the achievement of the nominal background rate of 10 mcps which is a prerequisite to reach the neutrino mass sensitivity of $0.2\,\mathrm{eV/c^2}$ with a 90 % confidence level targeted by KATRIN.

The determination of the neutrino mass is of high interest, since it would not only provide information on small scales physics as the Grand Unified Theory in elementary particle physics but also allow a more detailed insight on cosmological scales and the evolution of the universe. The KATRIN experiment aims for the direct measurement of the (anti-)neutrino mass by investigating the kinematics of electrons which originate from β-decay processes of molecular tritium close to the endpoint energy E_0. According to the energy conservation law, the non-vanishing rest mass of the (anti-)neutrino leads to a change of the spectral shape in the endpoint of the spectrum.
Within the scope of this thesis, reduction methods of background processes occuring in the spectrometer section of KATRIN will be addressed.
Simulation of ion trajectories were performed with the event based Monte Carlo simulation software Kassiopeia which will be introduced in chapter 3. As a first step, studies of simulation settings have been conducted by verifying the impact of the step size control options on the accuracy of ion trajectory simulations.
In order to assess the measured data obtained through experiments during the First Light Plus measurement campaign, the D_3^+-ion transmission efficiency of the pre-spectrometer was simulated at different magnetic field settings. The comparison of the measured secondary electron rate to the transmitted ion rate in the simulation showed a difference in the behaviour of the rates on the magnetic field strength. It is assumed that this discrepancy is caused due to the neglection of the deuterium ion propagation in the main spectrometer.
Furthermore, the simulation software Kassiopeia was extended by implementing the cross section for the ionization of water molecules by protons. Simulations including the ionization of residual gas molecules by ions yielded a ionization efficiency of $k_{sim} = (2.55 \pm 0.06) \cdot 10^{-6}\,\frac{e^-}{ion}$ describing the relationship between the secondary electron rate on the focal plane detector and the rate of ions entering the main spectrometer at a pressure of $p = 1 \cdot 10^{-10}\,\mathrm{mbar}$. The comparison with the ionization efficiency obtained through measured data led to a discrepancy of a factor 1.86. Systematic uncertainties in the measurement are assumed to be the main cause for this difference.

In addition, simulations with respect to the quantification of T_3^+-ions by means of the measurement of the ion current onto the cone electrodes of the pre-spectrometer elevated on potential were carried out at different potential settings. According to the obtained results from simulations, the detection efficiency of T_3^+-ions on cone electrodes exceeds 80 %.

Apart from simulations with respect to background processes induced by ions, measurements targeting the investigation of the UV irradiation impact on the inner surface of the main spectrometer were carried out. It was pointed out in previous measurements that Rydberg atoms generated by the decay of ^{210}Pb-atoms and accompanying processes represent the root cause for the increased background rate. One goal of this work was to study the reduction efficiency with respect to the target mass for Rydberg atoms at the inner surface of the spectrometer by irradiating the spectrometer surface with a high intensity UV light source. Therefore, the light source was operated continuously for approximately 90 hours after baking of the main spectrometer. Comparing the background rate before and after the operation led to the conclusion that the background electron rate originating from the spectrometer volume remains unaffected while the background rate emerging from processes at the inner surface of the stainless steel-vessel increases by a factor of 3. The causality of this behaviour of the secondary electrons could not be identified. By categorizing such secondary electrons in single and cluster events[1], a correlation between the pressure in the main spectrometer volume and single events could be observed. In contrast, the rate of cluster events is not correlated to pressure.

[1] events with an interarrival time of $\Delta < 0.1\,\mathrm{s}$ were considered as cluster events

Contents

Abstract v

1. Neutrino Physics 1
1.1. The discovery of the neutrino . . . 1
1.2. Neutrinos in the Standard Model . . . 2
1.3. Neutrinos beyond the Standard Model . . . 3
1.3.1. The solar neutrino problem . . . 3
1.3.2. Neutrino oscillations . . . 5
1.4. The measurement of neutrino masses . . . 7
1.4.1. Indirect measurement methods . . . 8
1.4.2. Direct measurement methods . . . 10

2. The KATRIN Experiment 15
2.1. The source and transport section (STS) . . . 15
2.2. The Spectrometer and Detector Section (SDS) . . . 17
2.2.1. The MAC-E filter principle . . . 17
2.3. Background sources and reduction . . . 20
2.3.1. Ion-induced background processes . . . 21
2.3.2. Ionization of Rydberg atoms . . . 22
2.3.3. Magnetically stored particles . . . 23

3. Preparatory ion simulations with Kassiopeia 25
3.1. The simulation software Kassiopeia . . . 25
3.2. Particle generation and tracking . . . 27
3.2.1. Generators and Terminators . . . 28
3.2.2. Step size controls . . . 28
3.3. Particle interactions . . . 29
3.3.1. Scattering processes . . . 29
3.3.2. Software package KESS . . . 30
3.4. Preparatory simulations in the KATRIN pre-spectrometer . . . 30
3.4.1. The adiabaticity in the pre-spectrometer . . . 30
3.4.2. The influence of step size control options . . . 31
3.4.2.1. Simulations with activated control length . . . 32
3.4.2.2. Simulations with both control options . . . 34
3.4.3. Influence of the ion mass on the accuracy . . . 35

4. Blocking and transmission efficiency of the pre-spectrometer 37
4.1. Ion blocking measurements during First Light Plus . . . 37
4.2. Ion simulations in the pre-spectrometer . . . 40
4.2.0.1. Simulation of ions through the beamline . . . 40
4.2.0.2. Fit of simulation result to measurement data for different magnetic field settings . . . 41

4.3. The pre-spectrometer as ion detector . . . 44
4.3.1. Modification of the pre-spectrometer geometry . . . 44
4.3.2. Detection and Transmission efficiency of tritium ions . . . 45

5. Ion scattering simulations in the main spectrometer 49
5.1. Direct measurement of ions with Pulcinella . . . 49
5.2. Comparison of measured secondary electron rate to simulation result . . . 50
5.2.1. Implementation of the ionization cross section in Kassiopeia . . . 50
5.2.2. Determination of the ionization efficiency . . . 50

6. Measurements with the UV light source LightHammer 55
6.1. Measurement goals . . . 55
6.2. Commisioning of the Light Hammer . . . 56
6.3. Background measurements before and after Light Hammer operation . . . 56
6.3.1. Reference background measurement before Light Hammer operation 56
6.3.2. Operation of the Light Hammer . . . 58
6.3.3. Background measurement after Light Hammer operation . . . 58
6.4. Discussion of the results . . . 61

7. Conclusion 63

Appendix 67
A. The TRIMS Experiment . . . 67
B. Simulation of electrons in the silicon detector of the TRIMS experiment . . . 68
B.1. Implementation of the TRIMS geometry in Kassiopeia . . . 68
B.2. Simulation of electrons inside the silicon detector . . . 69
C. Data sheet of Light Hammer . . . 73
D. Parameter sets for ionization cross sections . . . 74

Bibliography 77

List of Figures

1.1. **The solar standard modelbe:** The energy spectrum of neutrinos created by reactions in the sun is shown for different elements. Figure adapted from [31]. 4

1.2. **Energy spectrum of electrons produced by double β-decay.** The energy spectrum of secondary electrons created by $2\nu\beta\beta$-decay is shown. In case of $0\nu\beta\beta$-decay, the corresponding electrons would appear as an additional peak on the right side of the spectrum. Figure adapted and modified from [26]. 10

1.3. **Energy spectrum of electrons produced by single β-decay:** The energy spectrum of secondary electrons created by single β-decay procsses is shown. The influence of the neutrino mass is dominant in the endpoint of the spectrum. Figure adapted and modified from [65]. 11

2.1. **The experimental setup of the KATRIN experiment:** The 70 m long KATRIN-beamline can be divided in the Source and Transport Section (STS), consisting of the Rear Section, the WGTS, the CPS and the DPS, and the Spectrometer and Detector Section (SDS) which includes both spectrometers and the focal plane detector system. 16

2.2. **Schematic overview of the pre-spectrometer with its electrode system:** The pre-spectrometer is shown with the corresponding electrode system. The superconducting solenoids PS1 and PS2 are installed at the upstream and the downstream side of the pre-spectrometer. 20

2.3. **Illustration of the penning trap between the pre- and the main-spectrometer: Left:** An electron generated in a potential U_0 is stored in a localized volume moving back and forth between two potential barriers with $U < U_0$. The radial confinement is caused by the B-field. Figure adapted from [41]. **Right:** A visualization of the penning trap, which is formed in the space between the pre- and the main-spectrometer. 22

2.4. **Depiction of a magnetic bottle formed in the main-spectrometer:** Electrons are reflected at both ends of the spectrometers and consequently are stored in the magnetic bottle, if they fulfill the condition in equation 2.9. Due to the magnetic field, electrons undergo magnetron as well as cyclotron motion. Electrons which do not obey equation 2.9 leave the magnetic bottle and create a ring-shaped pattern on the FPD. Figure adapted from [30]. . . 24

3.1. **The zonal harmonic expansion method:**The magnetic field at $p_1(z, r)$ and $p_3(z, r)$ can be calculated with the zonal harmonic expension method, since they lie within the central (green) or the remote convergence region (blue). The estimation of the magnetic field at point $p_2(z, r)$ is not possible by applying the zonal harmonic method. 26

3.2. **Step size control options in Kassiopeia:** The exact calculation method is depicted on the left side. In this case, the position of the particle is calculated according to the Runge-Kutta algorithm (reference). In contrast to it, the adiabatic calculation method, shown on the right part, refers to the corresponding magnetic field line. 28

3.3. **The magnetic field of the KATRIN beamline:** The magnetic field strength through the KATRIN beamline is illustrated. It can be seen that the B-Field drops steeply in the region of the pre-spectrometer. 31

3.4. **The length of different ion trajectories:** The path length was determined for different control length options. The blue curve corresponds to a control length of $1 \cdot 10^{-2}$ m, while the red curve belongs to a control length of $1 \cdot 10^{-3}$ m and the violet one to $1 \cdot 10^{-4}$ m. 32

3.5. **Trajectories of trapped ions: Left:**The simulation was performed with a control length of $1 \cdot 10^{-2}$ m. The ion hits the pre-spectrometer at the bottom side on the left after moving back and forth through the pre-spectrometer. **Right:** The trajectory corresponds to a control length of $1 \cdot 10^{-3}$ m. In contrast to the case on the left part, the ion hits the pre-spectrometer on the upper right part. 33

3.6. **Trajectory lengths of non-trapped ions:** The path length was determined for different control length options. By choosing the reference control length of 0.001 m, the difference between the final positions were calculated for the trajectories belonging to the other two control lengths. Ions which trajectory lengths greater than 20 were exlcluded. 34

4.1. **The ELIOTT ion source:** The ion source was installed in the Rear wall in order to create artificially created ions. Figure adapted and modified from [53]. 38

4.2. **Secondary electron rate over magnetic field strength:** The measurement data of secondary electrons originating from ions which scatter with residual gas molecules is shown over the magnetic field strength. 39

4.3. **The KATRIN beamline in Kassiopeia:** The red line illustrates the propagation of a D_3^+- ion the Rear Wall to the entrance of the pre-spectrometer. The geometry package The Global Bag was used for the corresponding simulations. 41

4.4. **The radial and angular distribution of D_3^+-ions which reach the PS1 magnet: Right:** The radial distribution of the ions is shown. **Left:** The distribution over the polar angle to B is shown. The direction of the B-field is antiparallel to the z-axis. 41

4.5. **The increase of the magnetic field strength and the measured electron rate: Right:** The schematic increase of the magnetic field over time is illustrated. Static measurements at 20%, 40% and 80% were performed for about 10 min. **Right:** The measured electron rate on the FPD during the elevation of the magnetic field from 20% to 40% is shown. 42

4.6. **Transmission efficiency and fit of simulation result to measurement data: Left:** The transmission efficiency of the pre-spectrometer over the initial radius of the ion beam is shwon for different magnetic field settings. **Right:** The simulation results were fit to the measurement data by employing ROOT. The black points depict the meausurement data while the black line illustrates the fit performed by ROOT. 43

4.7. **Ion detection with the cone electrodes:** A virtual surface was implemented in a distance of about 2 cm to the inner electrodes to enable the detection of tritium ions with the cone electrodes. The terminator was set on the virtual surface. The red curve shows the trajectory of a tritium ion. 45

5.1. **Total cross section and energy distribution of secondary electrons: Left:** The total cross section is depicted over the energy of the proton. **Right:** The energy distribution of electrons originating from scattering processes of protons on water molecules is shown. 51
5.2. **Illustration of the secondary electron distribution over the terminators:** The secondary electrons are categorized by their terminators. The error bars represent the error based on a Poisson distribution of the electrons. 54

6.1. **The Light Hammer at port 100:** The Light Hammer was installed at port 100 of the main spectrometer. 55
6.2. **Results of the residual gas analyzer during the commissioning measurements:** The partial pressure curves shown over the measurement time. It can be seen that CO_2-molecules dominate the total pressure inside the spectrometer. 57
6.3. **Secondary electron rate from the volume before Light Hammer operation: Left:** The pixel distribution of the focal plane detector is shown. Outer pixel have been excluded for the analysis of the volume background rate. **Right:** The logarithm of the secondary electron distribution is depicted over their interarrival time. 58
6.4. **Results of the residual gas analyzer:** The partial pressure curves shown over the measurement time. Each color corresponds to a molecule species. . 59
6.5. **Secondary electron rate on the outer pixels before and after Light Hammer operation: Left:** The secondary electron rate before Light Hammer operation is shown for electrons emerging from the wall of the main spectrometer. As can be seen, the rate is constant over time. **Right:** The secondary electron rate after Light Hammer operation over the measurement time. It is striking that the rate behaves differently from before. 60
6.6. **Secondary electron rate from the volume of the spectrometer before and after Light Hammer operation: Left:** Shown is the secondary electron rate over the time before the Light Hammer operation. The rate is constant. **Right:** The background rate after the irradiation process is illustrated. 60
6.7. **Single and cluster events originating from the region of the spectrometer wall:** The blue data points are single events, while the red points represent the cluster events. It can be seen that a correlation exists between the rate of single events and the pressure, while the cluster rate is not affected and therefore is constant. 61

A.1. **Schematic overview of the experimental setup of TRIMS:** Ions and electrons caused by the β-decay of tritium are detected in coincidence. The solid line illustrates the direction of the ion while the dashed line corresponds to the movement of the electron. Figure adapted from [51]. 68
B.2. **The TRIMS-geometry in Kassiopeia: Left:** The geometry of TRIMS consists of four cylinder spaces in Kassiopeia. It is divided into the world space and the TRIMS space, which in turn includes the silicon space with its sensitive space. **Right:** A visualization of the silicon space geometry in Kassiopeia with one electron trajectory is shown. 69

B.3. **The ratio between the energy loss in the dead layer and the initial electron energy:** The ratio between the energy loss in the dead layer and the initial energy was determined for each energy range by applying the software ROOT. 71
B.4. **Relative energy loss of electrons for different energy ranges:** The ratio between the energy loss of in the dead layer and the initial energy was determined for each energy range shown in table B.2. The mean value for each energy range was calculated via ROOT. 71

List of Tables

3.1. **Simulation parameters:** The overview of the parameters which were set before starting the simulation are presented. 32
3.2. **Energy conservation at different magnetic field settings:** The ratio between the initial kinetic energy and the final kinetic energy was calculated for 1000 simulated events at different magnetic field settings. The mean value was determined via ROOT and are shown below. 34
3.3. **Influence of the cyclotron control option:** The violation of energy conservation was determined for two different cyclotron control options. . . 35
3.4. **Violation of energy conservation for different ion species:** Here, the values of the ratio in equation 3.13 which is a measure for the violation of the energy were calculated for three different ion species. 36

4.1. **Detection and transmission efficiencies at different potential settings:** The simulation of T_3^+-ion trajectories with regard to the detection on the cone electrode and the transmission through the pre-spectrometer was carried out at different configurations. The voltage settings correspond to the potential on the downstream cone electrode. 46
4.2. **Settings for the simulation of D_3^+-ions at different magnetic fields:** The simulation of deuterium-ion trajectories was carried out at different magnetic field settings. Each simulation was performed with 10^6 ions. The applied parameter ranges are listed below. 47
4.3. **Settings for the simulation of T_3^+-ions:** An overview of the settings which were applied for the simulation of T_3^+-ion trajectories is shown. . . . 47

5.1. **Applied terminators for the simulation of secondary electron trajectories:** This table shows the settings of the terminators applied in the simulation of the secondary electron trajectories in the main spectrometer. . 53
5.2. **Secondary electrons categorized in terminators:** The termination of the secondary electrons categorized by the conditions. 53
5.3. **Settings for the scattering simulation:** The initial energy of the ions starting in the PS2 magnet, the magnetic field settings as well as the configuration of the electrode system is shown. 53

B.1. **Settings for the simulation of electrons in the silicon detector of TRIMS:** The parameter ranges and settings which were applied for the simulation of electron trajectories are shown. Each simulation was performed with 1000 electron. 70
B.2. **Allocation of simulation number to energy range:** Simulations were carried out for 5 keV ranges. The numbers represent the energy ranges in figure B.3. 72
D.3. **Ionization thresholds B_j, partitioning factors G_j and number of electrons N for different ionisation sub-shells in water vapour according to [63].** 74

D.4. **Parameter set for total cross section from [62].** 74

1. Neutrino Physics

Since its discovery in the last century, the neutrino which is the lightest known massive particle has gained high interest among physicists. It is known from theoretical investigations that the neutrino plays an important role in physics on small as well as on large scales. In particular the knowledge about its mass would provide further information in not only the field of particle physics but also with regard to cosmological aspects as the evolution of the universe [57].
However, experimental investigations of the neutrino turned out to be highly challenging due to its low interaction rate. The following chapter gives a short overview of neutrino physics by introducing the theoretical background and afterwards discussing different measurement methods.

1.1. The discovery of the neutrino

The existence of the neutrino was first postulated by Pauli in 1930 [57].
After the three radioactive decay modes α-, γ- and β- decay [64] had been discovered in the beginning of last century, energy spectra of these processes were investigated. In contrast to the discrete energy spectrum corresponding to the α-radiation, a continuous shape of the energy distribution was observed for the β-decay by J. Chadwick in 1914 [21]. Since the β-decay was assumed to be a two-body decay process, this process first seemed to violate the energy conservation law.
A few years later, Pauli suggested the existence of an electrically neutral, light particle with spin 1/2 [57]. This particle was assumed to be emitted with the electron thus turning the β-decay from a two-body to a three-body decay process:

$$\mathrm{n} \rightarrow \mathrm{p} + \mathrm{e}^- + \nu_\mathrm{e}. \tag{1.1}$$

In case of existence, the postulated particle would share its energy with the electron which would explain the continuity of the corresponding spectrum.
After Fermi's formulation of the coherent theory for a three-body decay in 1934 [32], Bethe and Peierls determined the interaction cross section of a MeV-scale neutrino of $\sigma < 1 \cdot 10^{-44}\mathrm{cm}^2$, corresponding to a penetration power of 10^{16} km in solid matter and a therefore low probability of detection [20]. About 20 years later, the "Project Poltergeist" performed by Cowan and Reines led to the experimental discovery of the neutrino [60]. Due to its low interaction rate, a nuclear reactor was used as a source. Employing a water tank, free protons of H_2O-molecules served as a target in order to enable the detection of electron antineutrinos. The annihilation process of the resulting positron e^+ with the electron led to the emission of two γ-rays with an energy of 511 keV each.
The addition of cadmium chloride $CdCl_2$ to the water tank allowed the capturing of the neutron a few μs later. The coincidence detection between the photons produced by the $e^+ - e^-$- annihilation process and the high energy γ-ray signal resulting from the transition

of the excited cadmium to its ground state was the conclusive evidence for the occurence of the inverse β- reaction and therefore for the existence of the electron-neutrino [23].
In 1962, a further type of neutrino ν_μ was discovered by Schwartz, Lederman and Steinberger at the Brookhaven National Laboratory BNL. By bombarding beryllium targets with high energy protons produced by the particle accelerator AGS, pions were produced which were observed to undergo a decay in flight according to

$$\begin{aligned} \pi^+ &\rightarrow \mu^+ + \nu_\mu \\ \pi^- &\rightarrow \mu^- + \nu_\mu. \end{aligned} \tag{1.2}$$

In contrast to muons, pions and neutrons, which were absorbed by the iron shielding located at a distance of approximately 21 m behind the target, the neutrinos ν_μ passed through the shield and reached the aluminium spark chamber detector. By demonstrating that only muons and no electrons were generated by reactions which took place inside the detector volume, the distinctness between the two neutrino flavours was proved [25].
The third leptonic particle state given by the τ was found in 1975. About 25 years later, the assumption of the existence of a corresponding neutrino flavor was experimentally validated. By employing the Tevatron accelerator at Fermilab and thus generating particle showers of D_S mesons which decayed according to

$$D_S \rightarrow \tau + \nu_\tau, \tag{1.3}$$

the DONUT collaboration was able to prove the existence of the ν_τ in a similar way as Schwartz and Lederman did for the ν_μ [48].

1.2. Neutrinos in the Standard Model

The standard model of particle physics describes all 17 elementary particles as well as three of four fundamental forces which are given by the following:

1. **Fermions:** The majority of elementary particles are fermions which have a half-integer spin of 1/2. The spin-statistics theorem shows that fermions respect the Pauli exclusion principle. Fermions are further divided into quarks and leptons: quarks carry color charges while leptons do not.

2. **Gauge bosons:** Gauge bosons act as force carriers and therefore describe interaction processes between elementary particles which underlie the gauge theory.
   The strong force is described by the gluon, the electromagnetic one by the photon. $W^\pm$ and Z^0 correspond to the electroweak interaction force. In constrast to fermions, bosons have an integer spin.

3. **Higgs Boson:** This scalar boson does not carry any charge or color and is responsible for giving mass to the elementary particles.

Neutrinos are spin 1/2 particles and do not carry color charge. They therefore belong to the group of leptons. Since neutrinos are electrically neutral, they only respect the weak interaction and thus couple to the bosons $W^\pm$ and Z^0.
The coupling behaviour of the weak interaction depends mainly on the helicity of a particle, which is defined as follows:

$$\mathcal{H} = \frac{\vec{\mathbf{s}} \cdot \vec{\mathbf{p}}}{|\vec{\mathbf{s}}| \cdot |\vec{\mathbf{p}}|}. \tag{1.4}$$

This quantity is the projection of the spin $\vec{s}$ to the momentum vector $\vec{p}$ and represents the parallel or antiparallel orientation of the spin with respect to the momentum of the

particle. If a particle does not possess mass, its helicity is clearly defined. In case of a massive particle, there exists always one reference system which is faster than the particle and therefore would lead to a change of the momentum direction and consequently the helicity.
From a theoretical point of view, each interaction is described by a matrix element including vectorial and/or the axial vectorial component. If the parity is conserved, the given force couples evenly on right-handed and left-handed particles. In this case, the force has either a completely axial or vectorial character, as for example the electromagnetic force, which is defined by only the vectorial component.
In contrast to it, forces which violate the parity show a matrix element including both, the axial as well as the vectorial component.
The discrepancy between the coefficients c_V and c_A represent the power of parity violation: the smaller their difference, the higher the violation. Accordingly, the violation becomes maximal for $|c_A| = |c_V|$.
The meausrement of the angular distribution of secondary electrons by for example the decay of muons allows the estimation of c_V and c_A. Experiments led to the result showing $c_V = -c_A = 1$ and thus a maximum violation of parity of the weak interaction [70]. At the same time, the massless character of neutrinos was indicated by the result of this measurement, since neutrinos are created by the exchange of W-bosons which only couple to fully right-handed antineutrinos and lefthanded neutrinos.
In 1957, the helicity of the neutrino was measured to $\mathcal{H}(\nu) = -1.0 \pm 0.3$ in the Goldhaber-experiment which also demonstrated the massless character of neutrinos [40].

1.3. Neutrinos beyond the Standard Model

During the first years after their discovery, neutrinos were assumed to be massless fermions as experiments hinted. However, further investigations led to the fact that neutrinos also play an important role in astroparticle physics acting as messenger particles. Experiments were carried out indicating that neutrinos possess non-zero mass since observed effects could only be explained by neutrino oscilations.
In the following, the solar neutrino problem and the corresponding measurements will be introduced. Afterwards, neutrino oscillations will be discussed which explain the effect observed in the measurements.

1.3.1. The solar neutrino problem

The standard solar model, shown in 1.1, was established by John Bahcall and describes physical processes which occur in the sun [18]. Making use of this model, the flux of neutrinos originating from the sun can be calculated.
Since neutrinos are electrically neutral, they propagate on a straight trajectory on the way to the earth. This property allows the determination of where the neutrino was created and therefore the position of stellar objects. The neutrino flux is a consequence of nuclear fusion processes in the core of the sun. Due to proton fusion which leads to the creation of helium, described by the following equation

$$4\mathrm{p} \rightarrow^4 \mathrm{He} + 2\nu_\mathrm{e} + 2\mathrm{e}^+ + 26.73\,\mathrm{MeV} \tag{1.5}$$

a high number of electron neutrinos are produced. This net reaction results from multiple reactions, which build the pp-chain [71]. Reactions within the pp-chain contributing to the creation of neutrinos, at different energy ranges, are depicted in 1.1.

The most important reaction of this chain is given by the first one, starting the chain:

$$\mathrm{p} + \mathrm{p} \rightarrow^2 \mathrm{H} + \mathrm{e}^+ + \nu_\mathrm{e}. \tag{1.6}$$

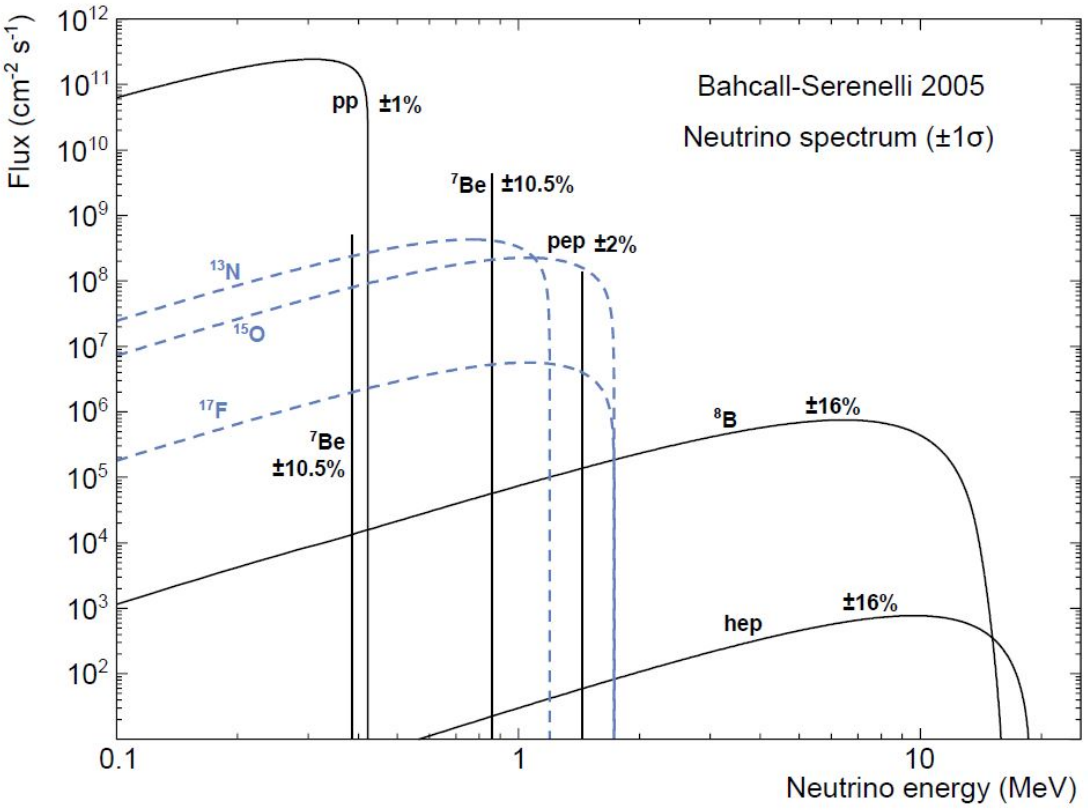

Figure 1.1.: The solar standard modelbe: The energy spectrum of neutrinos created by reactions in the sun is shown for different elements. Figure adapted from [31].

In order to validate the standard solar model, an experiment was carried out intending the measurement of the neutrino flux. The "Homestake experiment", named after the location of the Mine in South Dakota, where the experiment was performed, is based on the following reaction:

$$\nu_e + {}^{37}\mathrm{Cl} \rightarrow {}^{37}\mathrm{Ar} + e^{-}. \tag{1.7}$$

About 615 tons of liquid C_2Cl_4 was used as target material for the creation of neutrinos. After an exposition time of about 60-70 days, argon was created and extracted. With a half-life period of $T_{1/2} = 35$ days, the argon atoms decayed to excited $^{37}Cl^{*}$-atoms. By changing the state into the ground state, Auger electrons were emitted by Chlor, which then were detected by a proportional counter. By measuring the Auger electrons, the neutrino flux could be determined. The energy threshold of 814 keV for the reaction given in 1.7 allows the experiment to be sensitive for neutrinos created by ^{7}Be and ^{8}B.
Analyses led to the conclusion that the measured flux of neutrinos amounted to only $\frac{1}{3}$ of the theoretically expected value, which was called "the solar neutrino problem" [17].
However, the discrepancy could be explained by the experiments GALLEX [22], GNO, SAGE [1] and Kamiokande [34] by applying a different experimental concept. Observations in real time were enabled and the experiments allowed to be sensitive to more than one neutrino generation at the same time. In contrast to theoretical expectations, the missing neutrinos in the Homestake experiment reached the detector, but with a different neutrino flavor. This observation clearly demonstrated the occurence of neutrino flavor oscillations.
The SNO (Sudbury Neutrino Observatory)-experiment(1999-2006), led by Arthur Mc Donald, verified the existence of neutrino flavour oscillations of solar neutrinos [10]. In order to determine the total flux, 1000 t of heavy water (D_2O) was used and the following

reactions were observed:

$$\begin{aligned} \nu_e + {}^2\mathrm{H} &\rightarrow 2p + e^- \quad \text{(CC)} \\ \nu_i + {}^2\mathrm{H} &\rightarrow p + n + \nu_i \quad \text{(NC)} \\ \nu_i + e^- &\rightarrow \nu_i + e^- \quad \text{(ES)}. \end{aligned} \tag{1.8}$$

While radiochemical experiments only allowed the observations of charged current reactions, SNO was also sensitive on neutral current and elastic scattering processes. It was possible to measure neutrinos independent from the solar standard model. A non-zero flux of ν_e, ν_μ and ν_τ-neutrinos was observed which led to the conclusion that neutrinos change their flavors during their propagation to the earth. This process, the so-called "neutrino flavor oscillations" solved the problem of the "solar neutrino deficit" as will be discussed in more detail in the following subsection [71].

1.3.2. Neutrino oscillations

Neutrino flavour oscillations describe the transition of neutrino flavor states $\nu_\alpha \leftrightarrow \nu_\beta$ with $\alpha, \beta = e, \mu, \tau$ and only emerge in reactions involving the weak interaction force. B. Pontecorvo was the first one who formulated the theory of neutrino-antineutrino oscillations in 1957 [58]. This theory was later found to be applicable on neutrino flavors.
Flavor eigenstates do not show defined masses, but form a orthonormal basis and are correlated with the mass eigenstates ν_i which in contrast possess fixed masses:

$$|\nu_\alpha\rangle = \sum_{i=1}^{3} U_{\alpha_i} |\nu_i\rangle \quad \text{or} \quad |\nu_ß\rangle = \sum_{i=1}^{3} {U_{\alpha_i}}^* |\nu_\alpha\rangle \tag{1.9}$$

where U is the Pontecorvo-Maki-Nakagawa-Sakata (PMNS)- matrix with $U^\dagger U=1$. U is a 3x3 matrix with four free parameters: three weak mixing angles $\theta_{12}, \theta_{13}, \theta_{23}$ and the CP-violating phase δ. In case of Majorana neutrinos, two additional complex phases have to be considered.
As a neutrino is created, its flavor eigenstate is defined by a mixing of three mass eigenstates. The propagation of this neutrino requires the application of the time evolution operator $\exp(-\frac{i}{\hbar}Ht)$ on the state of the neutrino $|\nu_\alpha\rangle$ as follows:

$$|\nu_\alpha(t)\rangle = \exp(-iHt)\,|\nu_\alpha\rangle = \sum_{j=1}^{3} \exp\left(-\frac{i}{\hbar}E_j t\right) U^*_{\alpha_j} |\nu_j\rangle \tag{1.10}$$

with the energy $E_j = \sqrt{m_j^2 c^4 + p_j^2 c^2}$ and the Hamilton operator H.
Thus the probability to find a system in the state α' after the time t is given by:

$$P(\nu_\alpha \rightarrow \nu_{\alpha'}) = |\,\langle \nu'_\alpha|\exp\left(-\frac{i}{\hbar}Ht\right)\cdot|\nu_\alpha\rangle\,|^2 = |\sum_{j=1}^{3} U_{\alpha_j{}'} \exp\left(-\frac{i}{\hbar}E_j t\right) U^*_{\alpha_j}|^2 \tag{1.11}$$

Two-Neutrino flavor oscillations
In case of two neutrino flavor oscillations, for instance ν_e and ν_μ, the PMNS-matrix becomes a 2x2 matrix:

$$\begin{pmatrix} |\nu_e\rangle \\ |\nu_\mu\rangle \end{pmatrix} = \begin{pmatrix} \cos(\theta_{12}) & \sin(\theta_{12}) \\ -\sin(\theta_{12}) & \cos(\theta_{12}) \end{pmatrix} \cdot \begin{pmatrix} |\nu_1\rangle \\ |\nu_2\rangle \end{pmatrix}. \tag{1.12}$$

The transition probability is then given by:

$$P(\nu_e \rightarrow \nu_\mu) = \sin^2(2\theta_{12}) \cdot \sin^2\left(\frac{E_1 - E_2}{2\hbar}t\right) \tag{1.13}$$

for the so-called disapperance reaction. The probability for the apperance reaction is defined by the normalization condition with $P(\nu_e \to \nu_e) = 1 - P(\nu_e \to \nu_\mu)$. The charasteristic oscillation length is defined as follows

$$L_0 = \frac{4\pi\hbar}{c^3}\frac{E}{\Delta m^2}, \tag{1.14}$$

which turns the equation for the transition probability into

$$P_{\nu_\alpha \to \nu_\beta}(L, E) = \sin^2(2\theta) \cdot \sin^2\left(\frac{\Delta m^2 c^3 L}{4\hbar E}\right) \tag{1.15}$$

where θ is the amplitude of the oscillation and Δm^2 is defined by the oscillation length. The quantity L_0 plays an important role as the distance between the source and the detector given by L should be chosen targeting $L \approx L_0$ in order to get the maximum sensitivity with regard to the observation of the characteristic oscillation pattern. There exist in general two options which can occur:

- $L << L_0$**:** In this case, the distance between the detector and the source is too small. Consequently, the probability of a transition and thus for the observation of this effect is very low.

- $L >> L_0$**:** The detector is placed far away from the source. Due to the limited detector resolution or the source size, the transition probability which can be observed does not get higher than for $L \approx L_0$.

Measurement of neutrino oscillation parameters
The estimation of the three leptonic mixing angles θ_{ij} as well as the two independent squared neutrino mass differences Δm^2_{ij} can be accomplished by the investigation of neutrinos generated by different sources.
As discussed in 1.3.2, it is charasteristic for solar neutrinos to propagate over a long distance ($L \approx 150 \cdot 10^6$ km) and therefore undergo flavor oscillation processes. In order to investigate the type of neutrino flavor, the corresponding experiment must be generally sensitive to small mass differences or rather small mixing angles.

- **Solar neutrinos:** Besides SNO, which provided the proof for neutrino flavor oscillations, solar neutrinos are currently being investigated with the Borexino experiment [12]. Within the framework of this experiment, it was not only poissible to directly detect neutrinos from pep- and pp-chains in real time, but also to validate the Mikheyev-Smirnov-Wolfenstein (MSW)-effect, which refers to the survival probability of high energy electron neutrinos [56].

- **Atmospheric neutrinos:** Atmospheric muon-neutrinos are created by decay processes of pions originating from cosmic rays:

  $$\pi^+ \to \mu^+ + \nu_\mu. \tag{1.16}$$

  The muons further decay in neutrinos and positrons according to:

  $$\mu^+ \to \bar{\nu}_\mu + e^+ + \nu_e. \tag{1.17}$$

  In the upper layer of the earth atmosphere, the ratio of the different neutrino flavors is given by $\frac{N_{\nu_\mu}}{N_{\nu_e}} = 2$.

First measurements with regard to oscillation parameters were carried out by the Super-Kamiokande collaboration, which was led by Takaaki Kajita. In this experiment, 50000 tons of ultra-pure water in a stainless steel tank located 1000 m underground was used as a detector. Interaction processes of neutrinos with water molecules produce leptons, which are faster than light in water and thus generate Cherenkow radiation. In order to record this type of radiation, 1100 PMTs were applied. By considering the directional resolution it is possible to determine the propagation length of the neutrinos: Neutrinos, which enter the earth above the detector only have to pass through the atmosphere while those reaching the earth below the detector travel through the whole globe. Consequently, different propagation lengths correspond to different oscillation probabilities. Super-Kamiokande enabled the experimental determination of the discrepancy in the rate of neutrinos corresponding to these two cases θ_{12} and therefore proved the existence of neutrino oscillations.
Further experiments, for instance OPERA [27], Double Chooz, T2K [3] and KamLand [2] were performed for the determination of different mixing angles.

- **Particle accelerators:** Particle accelerators represent an artificial source of neutrinos. One advantage of this type of source is the possiblity to tune the neutrino energy which allows measurements of the mass difference with a higher precision. In this case, neutrino beams are generated by irradiating a target, for example aluminium with a proton beam. The resulting pions undergo decay processes and create neutrinos in the GeV range.

- **Nuclear fission reactors:** Employing nuclear fission reactors enable the investigation of neutrinos created by β-decays of neutron-rich fission products, for instance of uranium or plutonium fission. These processes lead to a total neutrino flux of approximately $\Phi_\nu = 2 \cdot 10^{20}/\mathrm{s}$ for a typical reactor. Such a method has been used by several collaborations, namely Daya Bay [14], Double Chooz [4] and RENO [11], with a consistent result given by $\sin^2(2\theta_{13}) = 0.093 \pm 0.008$.

Mass hierarchy of neutrinos
Since the absolute mass scale as well as the sign of the mass difference Δm^2_{23} is unknown, different scenarios regarding the mass-hierarchies are conceivable:

1. **Normal mass hierarchy:** This case refers to a positive sign of Δm^2_{23} which leads to $m_1 < m_2 << m_3$.

2. **Inverted mass hierarchy:** The mass hierarchy is given by $m_3 << m_1 < m_2$ and the sign of Δm^2_{23} thus positive.

The so-called quasi degenerated mass hierarchy based on the assumption that neutrino masses are relatively large compared to their difference ($m_1 \approx m_2 \approx m_3$) is applicable to both scenarios given above. However, the difference of neutrino masses do not provide any information with regard to the absolute mass scale.

1.4. The measurement of neutrino masses

There exist in general two methods that can be applied when it comes to the estimation of neutrino masses. After introducing indirect measurement methods in 1.4.1, the direct measurement method, which is used in the KATRIN-experiment will be discussed.

1.4.1. Indirect measurement methods

Indirect methods rely on theoretical models. Two approaches, namely the cosmological determination and the neutrinoless double β-decay will be introduced.

Cosmological determination

Currently, the description of the universe is based on the ΛCDM-model [52]. This model refers to a universe starting with a big bang, which has evolved from a hot dense state in the beginning to the cold era nowadays. According to ΛCDM, the dark energy (Λ) and the cold dark matter (CDM) dominate the universe today. Also, this model states the existence of cosmic neutrino background as well as cosmic microwave background (CMB). About $3.8 \cdot 10^5$ years after the big bang, neutral atoms were forming and the decoupling of photons and thus their free streaming started. The decoupling processes originate from the expansion and the emerging cooling process of the universe. Atoms which were ionized started recombining with free electrons at a temperature of approximately 3000 K.
Before these processes took place, the whole universe was in a thermal equilibrium so that the photons could be described by a characteristic black body spectrum with the temperature at the time of the decoupling. Due to the Hubble expansion, photons lost part of their energy which results in a shift of the spectrum and therefore a temperature of T=2.7 K [33].
In a similar way to the CMB model, the ΛCDM model predicts the existence of relic neutrino background with a temperature of T=1.95 K today and a density of $n_\nu = 336 cm^{-3}$ [71]. This abundant number of the density is crucial with regard to the formation of structures in the early universe, whereby the impact depends on the mass. Considering the sum of mass eigenstates of all non-relativistic neutrinos, the contribution of the energy density of the neutrinos Ω_ν to the total energy density can be calculated by the following equation

$$\Omega_\nu = \frac{\sum_i m_i}{93.14 H^3 \cdot eV/c^2} \tag{1.18}$$

with the dimensionless Hubble parameter H. Assuming neutrino masses of about 2 eV for each mass eigenstate would lead to a fraction of $> 10\%$ for the energy density of relic neutrinos of the total energy density in the universe. This would imply a lower contribution of baryonic matter content. Obviously, the determination of neutrino masses plays an important role with regard to the evolution of the universe.
Concerning large scale structures, the sum of all neutrino masses could be estimated by basically fitting parameters to different cosmological sets of data. An upper limit was released by the Planck collaboration [8] given by

$$\sum_i m_2 < 0.230 \frac{eV}{c^2} \quad (95\%CL). \tag{1.19}$$

This result was estimated by combining the measurements of CMB temperature fluctuations with the WMAP polarization measurement and large scale structure data from surveys referring to baryon acoustic oscillations [7].
However, limits which are based on cosmological observations depend strongly on the considered model.

Neutrinoless double β-decay

A further approach which allows the estimation of neutrino masses is given by the investigation of the neutrinoless double β-decay.
The Bethe-Weizsaecker equation generally defines the binding energies of nucleons in nuclei [69]. In case of isobars with a fixed number of nuclei A, the equation simplifies

to a parabola. For even A, the mass-parabola is split in two parabolas due to the spin coupling between the constituents of the nucleus. The lower-lying parabola represents nuclei with even-even configurations in terms of N and Z, while the other one describes binding energies with odd-odd configurations. Such a splitting of the parabola can lead to a forbidden single β-decay of an ee-nucles with regard to energy conservation, if the neighboring oo-nuclei possess higher binding energies than the considered ee-nucleus. In this case, the nucleus might undergo a double β-decay process directly changing into the next lower-lying ee-nucleus. This process can be described by the following equations:

$$\begin{aligned} {}^{\mathrm{A}}_{\mathrm{Z}}\mathrm{X} &\rightarrow {}^{\mathrm{A}}_{\mathrm{Z+2}}\,\mathrm{Y} + 2\mathrm{e}^- + 2\bar{\nu}_\mathrm{e} \\ {}^{\mathrm{A}}_{\mathrm{Z}}\mathrm{X} &\rightarrow {}^{\mathrm{A}}_{\mathrm{Z-2}}\,\mathrm{Y} + 2\mathrm{e}^+ 2\nu_\mathrm{e}. \end{aligned} \tag{1.20}$$

Since the double β-decay is a second-order process of weak interaction, it has a low decay rate and thus corresponds to relatively long half-lives ($\approx 10^{20}$ years) [71]. For this reason, the discovery of such a process was made several years after its postulation in 1935 in the geochemical experiment where a $2\nu\beta^-\beta^-$-decay of ^{82}Se into ^{82}Kr was observed.
Soon after the theory of E.Majorana, claiming that neutrinos occur as their own antiparticle [54] had been postulated, W. Furry [35] and G. Racah [59] suggested a further process yielding a double β-decay: The exchange of two Majorana-like neutrinos leading to the transformation of neutrons into protons and vice versa, according to:

$$\begin{aligned} {}^{\mathrm{A}}_{\mathrm{Z}} &\rightarrow {}^{\mathrm{A}}_{\mathrm{Z+2}}\,\mathrm{Y} + 2\mathrm{e}^-(0\nu\beta^-\beta^-) \\ {}^{\mathrm{A}}_{\mathrm{Z}}\mathrm{X} &\rightarrow {}^{\mathrm{A}}_{\mathrm{Z+2}}\,\mathrm{Y} + 2\mathrm{e}^+(0\nu\beta^+\beta^+). \end{aligned} \tag{1.21}$$

This process would lead to an additional discrete line in the energy spectrum at the endpoint representing a two-body process, as illustrated in figure 1.2.

As the equations above show, the neutrinoless double β-decay violates the lepton number conservation and thus is forbidden in the Standard Model. As a consequence, the observation of such a process would indicate physics beyond the Standard Model.
Considering the simplest case, represented by a purely left-handed V-A weak current and light massive Majorana neutrinos, the half-life time of the neutrinoless double β-decay can be calculated as follows:

$$(\mathrm{T}^{0\nu}_{1/2})^{-1} = \mathrm{G}^{0\nu}(\mathrm{E}_0, \mathrm{Z}) \cdot |\mathrm{M}^{0\nu}_{\mathrm{GT}} - \frac{\mathrm{g}_\mathrm{V}^2}{\mathrm{g}_\mathrm{A}^2} \cdot \mathrm{M}^{0\nu}_{\mathrm{F}}|^2 \cdot < \mathrm{m}_{\beta\beta} >^2 \tag{1.22}$$

where $\mathrm{G}^{0\nu}(\mathrm{E}_0, \mathrm{Z})$ is the phase-space integral, $\mathrm{M_{GT}}^{0\nu}$ and $\mathrm{M_F}^{0\nu}$ the Gamov-Teller and Fermi nuclear matrix elements, $\mathrm{g_V}(\mathrm{g_A})$ the vector (axial-vector) coupling constant of the electroweak interaction and $< m_{\beta\beta} >$ the effective neutrino mass.
The quantity given in the latter represents the coherent sum of neutrino mass eigenstates:

$$< \mathrm{m}_{\beta\beta} >^2 = |\sum_{\mathrm{k}=1}^{3} \mathrm{U}^2_{\mathrm{ek}} \mathrm{m_k}|^2 = \sum_{\mathrm{k}=1}^{3} |\mathrm{U_{ek}}|^2 \exp(\mathrm{i}\alpha_\mathrm{k}) \mathrm{m_k}|^2. \tag{1.23}$$

Here, α_k correspond to the CP-violating Majorana phases.
Applying equation 1.22 allows the estimation of the effective neutrino mass, if the half-life time of the $0\nu\beta\beta$-decay as well as the nulear matrix elements are known. Since the $0\nu\beta\beta$-decay has not been observed yet, it is only possible to calculate an upper limit for this quantity and thus for the effective neutrino mass.
Currently, several collaborations COBRA [29], EXO-200 [67], KamLAND-Zen [38], GERDA [6] and MAJORANA [5] are focusing on the investigation of the $0\nu\beta\beta$-decay, employing

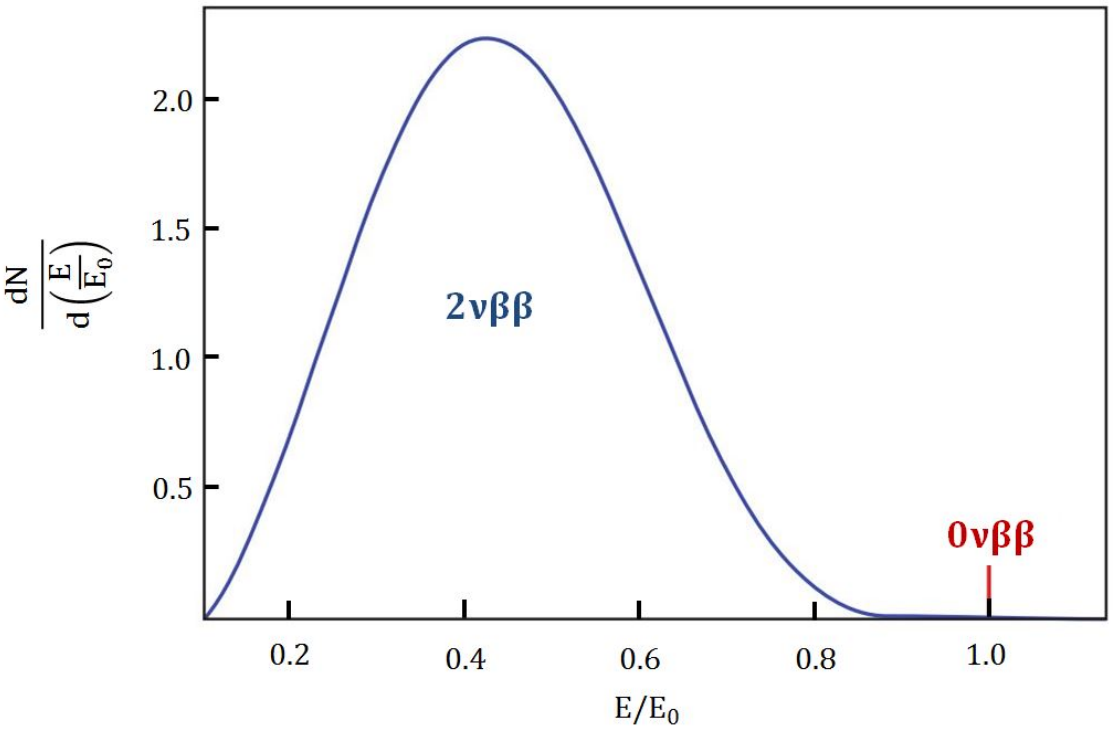

Figure 1.2.: Energy spectrum of electrons produced by double β-decay. The energy spectrum of secondary electrons created by 2νββ-decay is shown. In case of 0νββ-decay, the corresponding electrons would appear as an additional peak on the right side of the spectrum. Figure adapted and modified from [26].

different 2νββ-isotopes as a source/detector. With a detector mass of 375 kg ^{76}Ge, GERDA-II determined an upper limit of the half-life time to

$$T^{0\nu}_{1/2} > 5.3 \cdot 10^{25}\,\mathrm{y} \quad (90\%\mathrm{CL}). \tag{1.24}$$

Combining this result with the value obtained by phase I [9], the upper limit for the effective neutrino mass was calculated to

$$< m_{\beta\beta} > \; < 160 - 260\,\mathrm{meV} \quad (90\%\mathrm{CL}). \tag{1.25}$$

1.4.2. Direct measurement methods

Direct measurement methods are distinguished by the fact that they purely rely on kinematics of the β-decay, described by the relativistic energy-momentum relation

$$E^2 = p^2c^2 + m_0^2c^4. \tag{1.26}$$

Here, E describes the energy, p the momentum and m_0 the rest mass of the particle. In comparison to indirect measurement methods, direct measurements are independent from models and do not include theoretical assumptions.
The KATRIN experiment makes use of this method by investigating the kinematics of single β-decay.

Kinematics of single β-decay

Single upbeta-decay processes, described by the following equation, allow investigations of the neutrino mass in a model-independent way.

$$n \rightarrow p + e^- + \bar{\nu}_e. \tag{1.27}$$

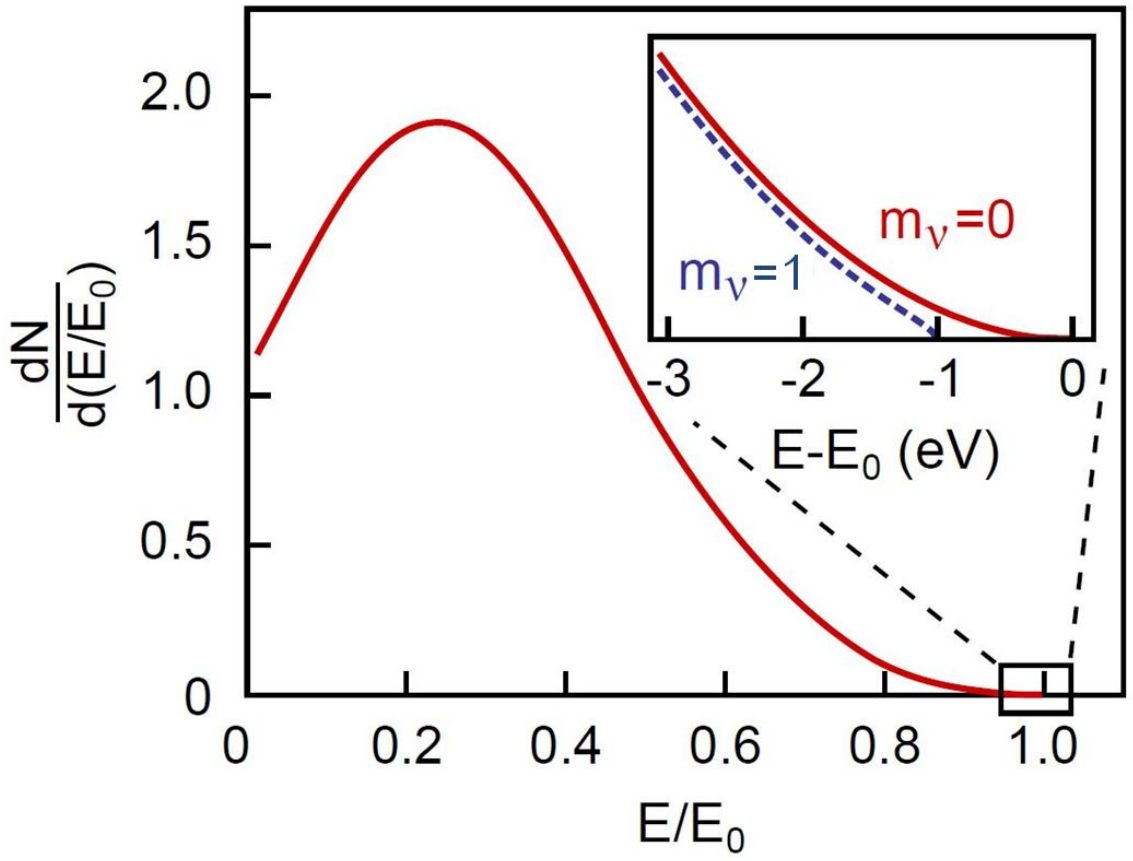

Figure 1.3.: Energy spectrum of electrons produced by single β-decay: The energy spectrum of secondary electrons created by single β-decay procsses is shown. The influence of the neutrino mass is dominant in the endpoint of the spectrum. Figure adapted and modified from [65].

The corresponding energy spectrum of the emitted electron, which is shown in 1.3, contains information on the energy and thus for the mass of the electron antineutrino. Though the momentum of the released antineutrino is close to zero, it reduces the maximal kinetic energy of the electron with its finite rest mass. Hence, making use of the energy as well as the momentum conservation law, precise spectroscopy of the kinetic energy of the outgoing electron enables the determination of the electron antineutrino mass. Nevertheless, it must be considered that the uncertainty on the neutrino mass scales with the Lorentz factor γ. Due to this reason, experimental investigations on the neutrino mass are very challenging. The corresponding uncertainty is given by

$$\delta m_\nu = \frac{E_\nu}{m_\nu} \cdot \delta E_\nu = \gamma \cdot \delta E_\nu. \tag{1.28}$$

Since the rest mass of the neutrino is hidden due to its relativistic movement, the investigation must be focused on the endpoint of the β-spectrum considering non-relativistic neutrinos.
Fermi's golden rule describes the process of the β-decay from theoretical point of view:

$$\frac{d\dot{N}}{dE} = \Gamma_{i\to f} = 2\pi \cdot |M_{fi}|^2 \rho(E_f) \tag{1.29}$$

where $\Gamma_{i\to F}$ refers to the transition rate from the initial state $|i\rangle$ to the final state $|f\rangle$, M_{fi} represents the transition matrix element between the two states, $\rho(E_F)$ stands for the densitiy of the final states corresponding to the energy E_f.

In order to obtain the rate of the β-decay as a function of the electron energy, the integral over all discrete and continuous final states has to be calculated, considering the relativistic energy-momentum relation. This leads to the following equation with the Fermi coupling constant G_F, the Cabbibo angle θ_c, the energy-independent nuclear matrix element of super-allowed transitions M and the Fermi-function F(Z+1,E), which takes the Coulomb interaction of the released electron with its daughter nucleus and shell electrons in account:

$$\begin{aligned}\frac{dN^2}{dEdt} = \frac{G_F^2 \cdot \cos^2(\theta_c)}{2\pi^3} \cdot |M|^2 \cdot F(Z+1,E) \cdot p \cdot (E + m_e c^2) \times \\ (E_0 - E)\sqrt{(E_0 - E)^2 - m_{\bar{\nu}_e}^2} \cdot \Theta\left(E_0 - E - m_{\bar{\nu}}^2\right).\end{aligned} \tag{1.30}$$

The Heaviside step function Θ is responsible for the energy conservation, since the neutrino can only be generated if the available energy of the decay is high enough.
Different isotopes can be employed in order to investigate the electron (anti-)neutrino mass by making use of the direct measurement method. In the following, two examples will be introduced.

Tritium experiments
The β-decay of tritium is described as follows:

$$^3H \rightarrow ^3He^+ + e^- + \bar{\nu}_e. \tag{1.31}$$

The use of tritium for the estimation of the neutrino mass offers several advantages:

- **Short half-life time:** Tritium has a relatively short half-life time of $T_{1/2} = (12.33 \pm 0.02)$ years yielding a high specific activity.

- **Low endpoint energy:** The endpoint of the energy-spectrum of the electrons is $E_0 = (18.577 \pm 0.007)\,\text{keV}$. Since the energy is relatively low, the number of decays in this range and therefore the statistics get higher.

- **Gaseous state of tritium:** Since tritium remains in the gaseous phase even at cryogenic temperatures, effects as cluster formation processes do not occur by employing the WGTS which will be introduced in chapter 2.

- **Super-allowed nuclear transitions:** The advantage of super-allowed nuclear transitions is given by its independence on energy.

- **Simple structure of the nucleus:** Tritium has a nuclear charge of Z=1 and therefore allows the investigation of the electron behaviour with a relatively high accuracy. In addition, interactions with shell electrons are not as likely as for other elements with higher nuclear charges.

However, the disadvantage when using tritium as a source is the fact, that it exists in a molecular and not atomic state. Due to this fact, the molecule resulting from the tritium-decay is in a vibrational or rotational state. As a consequence, the energy of the β-electron is reduced which leads to a systematic uncertainty in the investigation of the (anti-)neutrino mass.
Experiments in Mainz [49] and Troitsk [15] have been carried out applying tritium as a source and led to the upper limits of

$$\begin{aligned}\text{Mainz(gaseous source)} : m_{\nu_e} < 2.3\,\text{eV} \quad (95\%CL) \\ \text{Troitsk(solid source)} : m_{\nu_e} < 2.05\,\text{eV} \quad (95\%CL)\end{aligned} \tag{1.32}$$

In contrast, the Project 8 Collaboration targets the development of an atomic tritium source in order to determine the neutrino mass based on the Cyclotron Radiation Emission Spectroscopy (CRES) [16]. Thereby, a sensitivity down to

$$m_{\nu_e} \leq 40\,\text{meV}(90\,\%\text{C.L.}) \tag{1.33}$$

can be achieved. The electron created by the β-decay of tritium atoms in a uniform magnetic field executes a cyclotron motion. The observation of the emitted cyclotron radiation allows the determination of the frequency which is directly related to the electron energy since it only depends on the magnetic field strength, the mass and the charge of the electron. In order to enable the experiment, an operating temperature near $T = 1\,K$ is required [28].

Rhenium and Holmium experiments

The employment of cryogenic kalorimeters of isotopes ^{187}Re(rhenium) or ^{163}Ho (holmium) represent a further direct method to measure the secondary electron energy. In this case, the isotope acts both as a source and a detector. The energy of the electrons is determined by measuring the increase of the temperature.

One disadvantage of kalorimeters is, that two simultaneous signals occuring in one detector volume can not be distinguished. For this reason, a low decay rate is required when applying this method.

To achieve this, the detector volume is split and a high number of single detector modules, which are thermally isolated from each other, are implemented. The measurement methods applied by employing ^{187}Re and ^{163}Ho isotopes can be distinguished as follows:

- **Investigation of β-decay processes:** The investigation of β-decay processes of ^{187}Re according to

  $$^{187}\text{Re} \rightarrow ^{187}\text{Os}^{+} + e^{-} + \bar{\nu}_e \tag{1.34}$$

  allows the derivation of an upper limit on the (anti-) neutrino mass. In doing so, the MILANO [66] experiment determined the currently best upper limit of

  $$m_{\nu_e} < 15\,\text{eV} \quad (90\%\text{CL}). \tag{1.35}$$

- **Investigation of electron capture processes:** Due to solid-state effects that occur in kalorimeters based on ^{187}Re, a further method is applied in order to determine the neutrino mass. By employing ^{163}Ho-isotopes, the ECHo (Electron Capture ^{163}Holmium) collaboration targets the direct measurement of the neutrino mass with a sensitivity of $<1\,$eV by a precise investigation of the energy spectrum corresponding to the electron capture process

  $$^{163}\text{Ho} + e^{-} \rightarrow ^{163}\text{Dy} + \nu_e. \tag{1.36}$$

2. The KATRIN Experiment

The aim of the KATRIN (KArlsruhe TRItium Neutrino)-experiment, located at the Karlsruhe Institute of Technology (KIT) in Karlsruhe, is the direct measurement of the effective electron (anti-)neutrino mass with a sensitivity of

$$m_{\bar{\nu}_e} \leq 0.2\,\mathrm{eV/c^2} \quad (90\%\mathrm{CL}) \tag{2.1}$$

based on precise kinematic investigations of the energy spectrum of electrons originating from β-decay processes of molecular tritium.
In order to achieve this goal, the sensitivity of previous experiments is improved by one order of magnitude. For this purpose, KATRIN makes use of a spectrometer with relatively large dimensions applying the MAC-E filter technique which will be explained in section 2.2.1.
First beamline commissioning measurements have been carried out in October 2016 where the source, the transport and spectrometer section were operated simultaneously for the first time. Electrons and ions which were created by a photo-electric electron source propagated through the whole 70 m long KATRIN beamline for the first time.
The experimental setup, depicted in figure 3.3 as well as the measurement method applied in the KATRIN experiment will be described in the following. After introducing the different components of the experimental setup, the main background processes occuring in the KATRIN experiment will be highlighted.

2.1. The source and transport section (STS)

The source and transport section which will be addressed with STS in the following, includes the Windowless Gaseous Tritium Source (WGTS), the Differential Pumping Section (DPS) and the Cryogenic Pumping Section (CPS). The main functions of this section are the adiabatic transport of electrons emitted by the β-decay of tritium to the spectrometer section and the reduction of the tritium flow rate by 14 orders or magnitude. These requirements have to be fulfilled in order to achieve of the targeted sensitivity of the KATRIN experiment which corresponds to a tritium flow rate of $10^{-14}\mathrm{mbar} \cdot 1/\mathrm{s}$ at the end of the Cryogenic Pumping Section (CPS). The components of the STS will be described in the following.

The Windowless gaseous tritium source (WGTS)
The WGTS is assembled with an injection chamber with a length of 10 m and a diameter of 90 mm which is connected to the transport section on the one end while a gold-coated rearwall can be found on the other end. The back side of this rearwall, the so called Rear Section, is used for the activity monitoring of the tritium source and in addition enables the emission of electrons.
In KATRIN operation mode, gaseous tritium is introduced into the injection chamber with

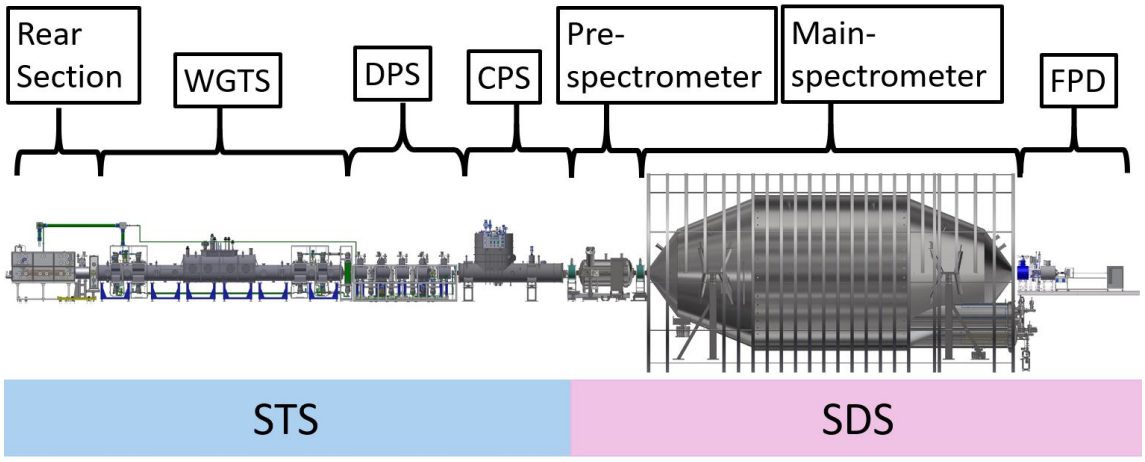

Figure 2.1.: The experimental setup of the KATRIN experiment: The 70 m long KATRIN-beamline can be divided in the Source and Transport Section (STS), consisting of the Rear Section, the WGTS, the CPS and the DPS, and the Spectrometer and Detector Section (SDS) which includes both spectrometers and the focal plane detector system.

a pressure of $p = 3.4 \cdot 10^{-3}$ mbar which is then distributed along the whole WGTS due to diffusion processes. At both ends of the WGTS tritium molecules are pumped out by different pumping systems. Six turbo molecular pumps (TMPs) are installed at each end in order to collect tritium gas and to feed it into the so-called inner loop system. This part ensures the stabilization of the tritium injection rate with a purity of higher than 95 %. In this way, a molecular tritium throughput of approximately 40 g/day can be obtained. This flow rate yields a constant column density given by $\rho \cdot d = 5 \cdot 10^{17}$ molecules/cm^2 in the WGTS at a fixed temperature of about $T = 27$ K. Electrons originating from β-decay processes are guided adiabatically to the end of the WGTS by a magnetic field of $B = 3.6$ T generated by seven superconducting soledoids.

The Differential Pumping Section (DPS)
The achievement of the total sensitivity in the KATRIN experiment requires the minimization of background processes as effective as possible. Thus the suppression of the tritium flow rate along the beamline is desirable to prevent tritium molecules from entering the spectrometer section. Apart from the contamination of the spectrometers, tritium molecules would contribute to a higher background rate by generating positive ions as will be explained in section 2.3.1. Since tritium is not completely pumped in the WGTS, a further reduction mechanism is required. The Differential Pumping Section (DPS) is responsible for a reduction of five orders of magnitudes. It consists of pipe segments which are tilted to 20° and therefore build horizontal chicanes. Four TMPs are mounted along the chicanes with a pumping power of 2400 l/s. The pipe segments are surrounded by five superconducting solenoids which generate a magnetic field of $B = 5.0$T ensuring the adiabatic transport of signal electrons to the spectrometer section. Since ions are not affected by the pumping processes and should be prevented from entering the spectrometer section, the following subsytems have been installed:

- **FT-ICR modules:** Two so-called FT-ICR (Fourier Transform-Ion Cyclotron Resonance) can be found at the entry and the exit of the DPS. These modules allow the identification of ion species by fourier transformation of the corresponding cyclotron motion and thus provide information about occuring ionization processes in the WGTS.
- **Dipole electrodes:** Four dipole electrodes are installed in the DPS in order to deflect ions to the surface of the pipe segments where they are neutralized immediately. The

neutral molecules are eliminated by TMPs of the DPS or the CPS.

- **Ring-shaped blocking electrode:** Blocking electrodes are located in the last pipe segment of the DPS ensure the confinement of ions in the region between source and electrode and therefore prevent them from further propagation along the beamline.

The Cryogenic Pumping Section (CPS)
The tritium flow rate of $10^{-7}\text{mbar} \cdot 1/\text{s}$ is further reduced by 7 orders of magnitude in this section. This reduction factor is achieved by means of the cryogenic pumping technique. Molecules hitting the surface of the argon frost layer are adsorbed immediately. The CPS is built of seven pipe segments, whereby two of them are tilted in an angle of 15° and to guide tritium molecules onto the cold surface layer. Seven superconducting solenoids, mounted along the CPS provide the transport of the flux tube given by $191\,\text{T} \cdot \text{cm}^2$ along the beamline.

2.2. The Spectrometer and Detector Section (SDS)

The spectrometer and detector section contains the pre- and the main spectrometer as well as the focal plane detector (FPD). The main tasks of this section are given by precise filtering of electrons with regard to their energy and the determination of the rate of signal electrons with an energy above the threshold of the main spectrometer. Making use of the so-called MAC-E filter technique explained below, the setup allows the measurement of the integral electron energy at the endpoint of the spectrum with an energy resolution of $\Delta\text{E} = 0.93\,\text{eV}$ that is required for the targeted sensitivity. Since the tritium flow rate is reduced efficiently by 14 orders of magnitude after passing the pumping sections, the background arising due to the partial pressure of tritium is negligibly small for both spectrometers. Nevertheless, it is yet crucial to prevent signal electrons from scattering processes with residual gas molecules. For this reason the pre- as well as the main spectrometer are operated at Ultra High Vacuum (UHV) condition with a pressure of about $\text{p} \approx 10^{-11}\,\text{mbar}$.

2.2.1. The MAC-E filter principle

A precise filtering of signal electrons with respect to their kinetic energy is prerequisite for the achievement of the total sensitivity in the KATRIN experiment. The MAC-E (Magnetic Adiabatic Collomation combined with an Electrostatic) filter technique has already been applied in previous experiments for neutrino mass measurements. This method is distinguished by a high resolution and a large angular acceptance at the same time [19], [50]. Combined with the high luminosity of the source, this property enables the resolution of tiny distortions in the electron energy spectrum caused by the non-vanishing rest mass of the antineutrino.
In the following, the principle of the MAC-E filter principle will be explained.

Electrostatic Filtering
The electrostatic filtering of signal electrons represents one of the key features of the MAC-E filter. By generating a potential barrier, an energy threshold for electrons is created. Electrons with a longitudinal kinetic energy

$$\text{E}_{\parallel} > |\text{e} \cdot \text{U}_0| \tag{2.2}$$

are transmitted while the electrons with energies lower than the barrier potential energy are reflected and do not reach the detector. In equation 2.2, U_0 is the applied potential and $\text{E}_{\parallel}$ describes the longitudinal component of the kinetic energy.
Since the potential barrier is sensitive to only the longitudinal component of the electrons

which in turn are emitted isotropically from β-decay processes, the adiabatic collimation of the electrons' momentum into longitudinal direction is desirable for a precise investigation of the resulting energy spectrum.

Magnetic-Adiabatic Collimation

The MAC-E filter technique requires strong magnetic fields. They are generated by superconducting solenoids in the KATRIN experiment. The goal is the adiabatic transport of electrons originating from β-decay processes of tritium and being emitted isotropically from the source.

The momentum $\vec{p}$ of an electron can be split into its longitudinal component $\vec{p}_{\parallel} = \cos\theta \cdot \vec{p}$ and a transversal component $\vec{p}_{\perp} = \sin\theta \cdot \vec{p}$ where θ defines the polar angle to the corresponding magnetic field line. The kinetic energy can then be written as

$$E_{kin} = \frac{|\vec{p}|^2}{2m} = E_{\parallel} + E_{\perp}. \tag{2.3}$$

The transverse component of the momentum causes a cyclotron motion around the corresponding magnetic field line, which results from the Lorentz force while the longitudinal component is responsible for the propagation of the electron along the field line.

The first adiabatic invariant of an electron with energy 18.6 keV propagating through an inhomogeneous magnetic field is defined by its magnetic momentum

$$\mu = \frac{E_{\perp}}{B} = \text{const.} \tag{2.4}$$

According to this equation, a decrease of the magnetic field leads to a drop of the transverse kinetic electron energy and thus to an increase of the longitudinal component. Hence, the transverse component of the kinetic energy transforms into the longitudinal component $E_{\perp} \rightarrow E_{\parallel}$, if the gradient of the corresponding magnetic field is kept sufficiently small. In this case, the collimation of the electron's momentum into the longitudinal direction is enabled. In order to allow a large number of electrons reaching the analyzing plane, a large drop of the magnetic field is required. The collimation of the electron energy and therefore the energy resolution depends on the fraction between the maximum and the minimum value for the occuring magnetic field given by

$$\frac{\Delta E}{E} = \frac{B_{min}}{B_{max}}. \tag{2.5}$$

As pointed out above, an energy resolution of $\Delta E = 0.93\,\text{eV}$ is prerequisite in order to achieve the total sensitivity in KATRIN. Considering the electron energy of 18.6 keV in the endpoint of the spectrum yields

$$\frac{\Delta E}{E} = \frac{0.93\,\text{eV}}{18.6\,\text{keV}} = 5.0 \cdot 10^{-5}. \tag{2.6}$$

A further quantity, which is constant at all times is given by the magnetic flux Φ defined by

$$\Phi = \int_A \vec{B} \cdot d\vec{A} = const. \tag{2.7}$$

Accordingly, a decrease of the magnetic field results in the increase of the radius of the flux tube. Hence, the diameter required at the analyzing plane for the main spectrometer can be calculated as follows:

$$d_{AP} = d_S \cdot \sqrt{\frac{B_S}{B_{min}}} \tag{2.8}$$

where d_{AP} describes the diameter of the flux tube at the analyzing plane and d_S the radial extension of the flux tube at the source.
Equation 2.8 and 2.6 make clear, that the desired energy resolution can only be achieved with sufficiently large diameters, which justifies the dimensions of the KATRIN spectrometers.

Magnetic Mirror Effect
The magnetic mirror effect refers to the opposite scenario of the adiabatic collimation. In this case, electrons are magnetically reflected when propagating from a region with a weak into a strong B-field. In the KATRIN experiment, the maximum magnetic field strength is not given in the source, but in the region between the spectrometer and the detector section ($B_{source} < B_{max}$). For this reason, a certain amount of signal electrons will be reflected back. The relation $|\tilde{p}_{s_\perp}| = \sin(\theta)$ in the source in combination with the condition that in the region of B_{max} the kinetic energy is completely represented by its transverse component ($E_{max_\perp} = E_{kin}$), an equation describing the maximum polar emission angle θ_{max} of electrons which are emitted from the source with a magnetic field B_S and not reflected by the maximum B-field B_{max} can be derived to

$$\theta_{max} = \arcsin\left(\sqrt{\frac{B_S}{B_{max}}}\right). \tag{2.9}$$

The Pre-Spectrometer
The pumping sections are followed by the pre-spectrometer with a diameter of approximately 1.70 m and a length of 3.38 m. Superconducting solenoids can be found at each end, which generate a maximum magnetic field of $B = 4.5\,T$. The pre-spectrometer is the first component in the KATRIN beamline that is located outside the Tritium Laboratory Karlsruhe (TLK). Due to the high tritium activity of $A = 10^{11}$ Bq in the WGTS, a further reduction of the β-electron flow rate is desired in order to reduce ionization processes of residual gas molecules, which would lead to a high background rate. For this reason, the pre-spectrometer is set on a potential which amounts to $U = -18.3\,kV$ and enables a pre-filtering of electrons, since the endpoint of the β-electron energy spectrum lies at $E = 18.6\,keV$. In addition, two turbo molecular pumps and getter pumps are with a total length of about 200 m are installed, which guarantee the ultra high vacuum condition at a pressure of $p = 10^{-11}$ mbar as well as a further reduction of the tritium flow rate.
A schematic overview with the electrode system of the pre-spectrometer is shown in figure 2.2. The ground electrodes are set to 0 V at all times while the wire electrode system, the cone electrodes and the vessel can be elevated on high potential. Two superconducting solenoids (PS1 and PS2) are responsible for the generation of the magnetic field in the pre-spectrometer.

The Main Spectrometer
The main spectrometer represents the largest component in the KATRIN beamline with a length of 23.2 m and a diameter of 9.8 m, resulting in a total volume of approximately $1240\,m^3$. The magnetic field in the main spectrometer is generated by the pinch magnet providing a maximum field of $B = 6\,T$, which is mounted at the downstream side and the PS2 magnet with $B_{max} = 4.5\,T$, connecting the pre- and the main spectrometer with each other.
The minimum magnetic field in the analysis plane located at the center of the spectrometer amounts to $B_{min} = 3 \cdot 10^{-4}\,T$.
14 air coils are installed around the vessel of the main-spectrometer in order to fine-shape the magnetic flux tube into its center. In addition, several vertical and horizontal cosine coils are used to compensate the earth magnetic field. A wire electrode system is installed

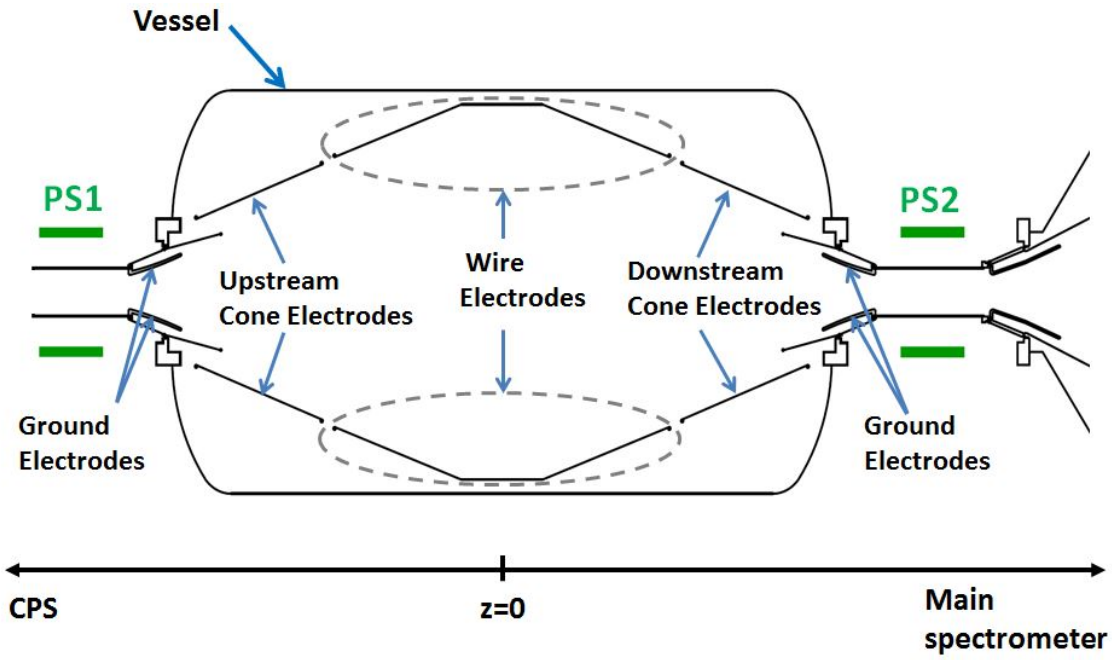

Figure 2.2.: Schematic overview of the pre-spectrometer with its electrode system: The pre-spectrometer is shown with the corresponding electrode system. The superconducting solenoids PS1 and PS2 are installed at the upstream and the downstream side of the pre-spectrometer.

on the inner side of the vessel which is responsible for the fine-shaping of the electric potential. Making use of turbo molecular pumps, a pressure of $p = 10^{-11}$ mbar is achieved. During the neutrino-mass-measurements, the retarding potential given by $q \cdot U_0$ of the main spectrometer is supposed to be varied in a small range which allows a precise scanning of the endpoint region of the β-electron energy spectrum.

The Focal-Plane Detector System

The focal-plane detector system is installed at the downstream end of the experimental setup and therefore completes the KATRIN beamline. Electrons, which have overcome the retardation potential of the main-spectrometer propagate through the focal plane detector system along the magnetic field lines provided by the pinch magnet and the detector magnet with $B = 3.6\,T$. When finally reaching the PIN (positive-intrinsic-negative doted silicon)-diode array, electrons are detected and their energy is determined. The PIN-diode array works with a high efficiency and is almost free of background.

The detector is a $500\,\mu m$ wafer with 148 radially distributed pixels, that allows a precise analysis of measurement data since spatial inhomogeneities of the $191\,T \cdot cm^2$ flux tube are considered.

The post acceleration electrode (PAE), is located upstream of the detector wafer is responsible for an energy boost of the β-electrons to an energy level at which the instrinsic detector background is sufficiently low. This leads to a detection efficiency of 95% with an energy resolution of $\Delta E = (1.52 \pm 0.01)\,keV$ (FWHM) at the endpoint of the spectrum at 18.6 keV [13].

2.3. Background sources and reduction

A detailed knowledge of background sources and processes is mandatory in order to develop appropriate reduction mechanisms and to achieve the targeted sensitivity on the neutrino mass measurement.

In the following, four major background sources occuring in the KATRIN experiment will be outlined.

2.3.1. Ion-induced background processes

This type of background mechanism is dominated by the following three processes:

1. **Ionization and β-decay processes in the WGTS:** According to theoretical expectations, the flux of positive tritium ions which will propagate from the WGTS into the transport section amounts to A $\approx 10^{11}$ 1/s (ref). Considering recombination processes of ions which originate from β-decay and ionization processes lead to this value whereby the primarily created ion rate amounts to $2 \cdot 10^{12}\, ions/s$ and thus is one order of magnitude smaller. Expected species of positive ions are given by $^3HeT^+$,$^3He^+$; T^+andT_2^+. Among those, T^+- and T_2^+-ions undergo charge exchange interactions with T_2-ions and thereby immediately transform to T_3^+-ions [47]:

$$T_2 + T_2^+ \rightarrow T_3^+ + T. \tag{2.10}$$

   Furthermore, recombination reactions of positive ions with thermalized secondary electrons created by ionization processes of β-electrons can occur. The corresponding dissociative recombination of T_3^+-ions can be described by the following equation:

$$T_3^+ + e^- \rightarrow T_2 + T. \tag{2.11}$$

   In case of collisions of positive ions, cluster ions such as T_5^+, T_7^+, T_9^+, showing relatively high dissociative recombination coefficients are created.

2. **Electrons stored in the inter-spectrometer Penning trap:** Specific configurations of electric and magnetic fields can lead to the storage of charged particles within a volume. In the KATRIN-experiment, a Penning trap is generated between pre- and main-spectrometer. As depicted in 2.3 an electron with a low energy created within a lower electric potential U_0 is then stored between two cathodes with $U < U_0$. The storage in the Penning trap results in a bouncing-movement, back and forth between the two cathodes. Electrons that are affected by this penning trap mechanism will undergo ionization processes with residual gas molecules and thus contribute to the generation of secondary electrons, as well as positive ions.

3. **β-electrons in the main spectrometer:** Finally, signal electrons that reach the main-spectrometer propagate through the volume and thereby ionize residual gas molecules. This process again leads to the creation of positive ions.

These three background sources generate positive ions which in turn create background electrons due to scattering processes with residual gas molecules in the volume of the main spectrometer. Secondary electrons resulting from such processes would reach the focal plane detector with a similar energy as the β-electrons which would contribute to the background of the neutrino mass measurement.
As pointed out in 2.1, ion prevention systems as the ring and dipole electrodes have been installed in the KATRIN beamline. Since voltage fluctuations on these devices would also affect the measurement of the neutrino mass in a negative way, it is of high importance to ensure their functionality. To do so, artificially created positive ions were transported through the whole experimental setup for the first time during the first beamline measurement campaign in November 2016.
The main goal of these ion measurements was the verification of the functionality of the blocking devices by measuring the ion flux in the spectrometer directly as well as indirectly by detecting the corresponding secondary electrons, as will be discussed in more detail in chapter 5.

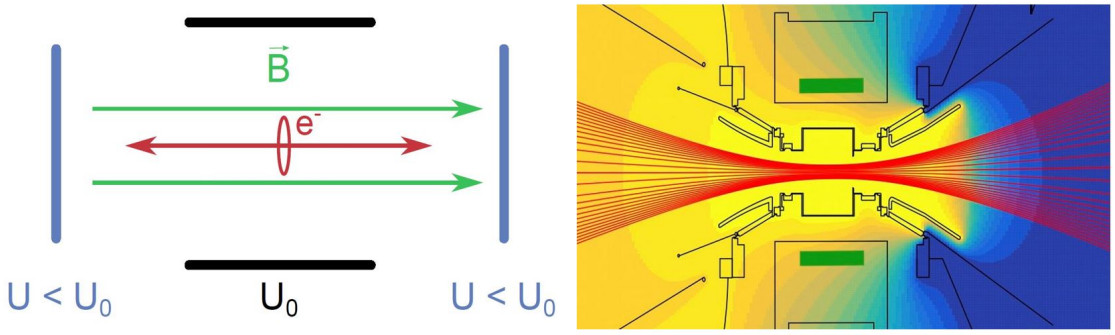

Figure 2.3.: Illustration of the penning trap between the pre- and the main-spectrometer: Left: An electron generated in a potential U_0 is stored in a localized volume moving back and forth between two potential barriers with $U < U_0$. The radial confinement is caused by the B-field. Figure adapted from [41]. **Right:** A visualization of the penning trap, which is formed in the space between the pre- and the main-spectrometer.

2.3.2. Ionization of Rydberg atoms

A further background source in the spectrometer section is ionization of Rydberg atoms. Rydberg atoms are characterized by their loosely bound valence electrons which possess high quantum numbers [36]. Such atoms can easily be ionized by either collision processes or the presence of strong electric fields, as for example the field of black-body radiation [45].
The generation of Rydberg atoms in the main spectrometer could be due to the impact of ^{206}Po-recoil ions originating from decay processes of ^{210}Pb-atoms which are implanted in the stainless steel vessel, as indicated in previous measurements. It is assumed that the inner surface of the spectrometer after a bake-out process is dominated by adsorbed hydrogen atoms. Since ^{206}Po-recoil ions possess kinetic energies of approximately 100 keV, they contribute to desorption as well as to excitation processes of hydrogen atoms when leaving the spectrometer vessel. Since the created hydrogen Rydberg atoms do not carry electrical charge, they are not affected by the shielding mechanisms provided by the inner electrodes and the magnetic field of the main spectrometer and thus enter the sensitive volume. Due to thermal black body radiation at room temperature of $T \approx 300\,K$, the Rydberg atoms are ionized and split into protons H^+ and electrons which possess energies in the meV-range [37]. Such electrons contribute to the background rate since their relatively small ionization rate of $R < 1500\,1/s$ keeps the probability of an ionization process for a propagating hydrogen Rydberg constant [42].
Thermal ionization processes are assumend to be dominant in the center of the spectrometer because the strength of the static electric field is very low in this region. In contrast, the influence of the electric field is strong on both ends of the spectrometer as well as in the region between the spectrometer vessel and wire layers of the inner electrode system. High electric fields lower the Coulomb potential of Rydberg atoms and therefore lead to higher ionization rates. This effect corresponds to the so-called selective field ionization which does not happen symmetrically [43].
Electrons, resulting from ionization processes of Rydberg atoms are detected by the FPD as they possess energies in the same energy region as the signal electrons created by tritium β-decay. In order to verify such an indication, the inner surface of the spectrometer was contaminated with ^{212}Pb by making use of a ^{228}Th-source during the SDS3 measurement campaign. ^{212}Pb provides similar properties as ^{210}Pb but shows a relatively short half life time of $T_{1/2}^{^{212}Pb} \approx 10\,h\,38\,min$ and therefore is appropriated to be employed for the measurement. Analysis of the results led to the identification of ^{210}Pb-atoms as a main background source and as a initiator of Rydberg atoms since the rate of the induced background was in

good agreement with the reference background rate.
Consequently, it can be stated that Rydberg atoms are candidates for the dominant background processes. For this reason, it is essential to minimize this type of background source as far as possible. As will be explained in more detail in chapter 6, measurements have been performed targeting the elimination of molecules from the inner surface of the spectrometer making use of a high intensity UV irradiation source.

2.3.3. Magnetically stored particles

As explained in 2.2.1, electrons generated in a weak magnetic field B_{min} are likely to get reflected due to the magnetic mirror effect while propagating to a region with a higher magnetic field B_{max}. This process corresponds to a turn-over of the momentum vector of the electron. According to equation 2.9, electrons with a polar angle $\theta > \theta_{max}$ are reflected at both sides at the bottle within a certain radius defined by their cyclotron motion around the field line. Such electrons can originate from α-decay processes of radon atoms in the volume of the main spectrometer [42]. Electrons which respect the equation

$$\theta > \theta_{max} = arcsin\left(\sqrt{\frac{qU(\vec{r}_s)}{E_{kin}(\vec{r}_s)} \cdot \frac{B(\vec{r}_s)}{B_{max}}}\right) \tag{2.12}$$

where $U(\vec{r}_s)$ and $B(\vec{r}_s)$ describe the electrostatic potential and the magnetic field at the position $\tilde{r}_s$, B_{max} the maximal magnetic field and θ the initial polar angle of the electron to the B-field, are trapped. Hence, the initial energy of the electron created in the Rn-decay plays a decisive role. Considering an initial magnetic field of 0.5 mT in the analyzing plane, a maximal magnetic field of 5 T and a potential of $U_0 = -18.6\,kV$, an electron with an energy of 10 eV leaves the magnetic bottle if its initial polar angle is smaller than 25.5° [42]. Therefore, low-energy electrons in particular those which possess energies below the energy resolution of $\Delta E = 0.93\,eV$ are not magnetically stored.
However, electrons with high initial energies can also leave the magnetic bottle: once the condition for the adiabaticity in equation 2.4 is not fulfilled, the electron leaves the trap. Besides the homogeneous electric field which causes the axial movement, trapped electrons underlie the impact of the non-homogenoues magnetic field. Hence, their motion result in a azimuthal path around the symmetry axis of the spectrometer accompanied by the cyclotron motion around the field line.
The spectrometer has the function of a magnetic bottle for a high number of electrons which are generated in its center, originating from nuclear decay of tritium or atomic relaxation processes of excited atoms. Secondary electrons created by scattering-off processes on residual gas show the same magnetron radius as the primary electron. Once the storage condition is not fulfilled anymore, electrons leave the magnetic bottle and reach the FPD where they cause a ring-shaped pattern which is charasteristic for such type of background electrons. This scenario is shown in figure 2.4.

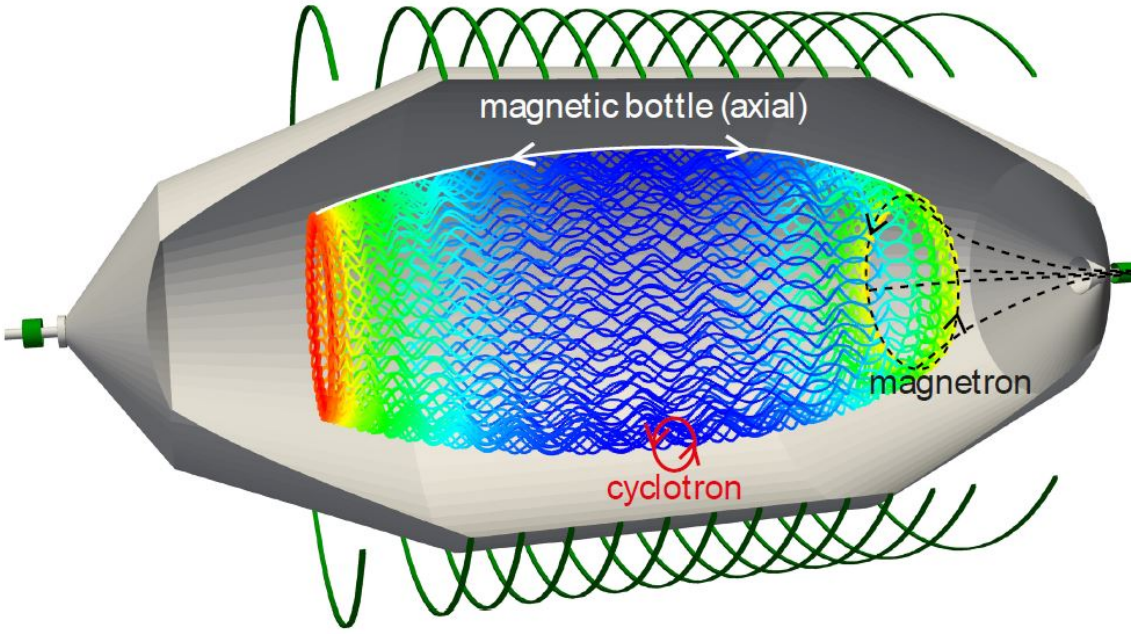

Figure 2.4.: Depiction of a magnetic bottle formed in the main-spectrometer: Electrons are reflected at both ends of the spectrometers and consequently are stored in the magnetic bottle, if they fulfill the condition in equation 2.9. Due to the magnetic field, electrons undergo magnetron as well as cyclotron motion. Electrons which do not obey equation 2.9 leave the magnetic bottle and create a ring-shaped pattern on the FPD. Figure adapted from [30].

3. Preparatory ion simulations with Kassiopeia

One focus of this thesis lies on ion simulations in the KATRIN spectrometers, which were performed with the simulation software Kassiopeia. Kassiopeia, primarily developed to meet the needs of the KATRIN collaboration, allows detailed tracking simulations of particles moving through complex electromagnetic field configurations [24].
This chapter gives an overview of the simulation settings and the available techniques of Kassiopeia. After introducing the calculation methods for electromagnetic fields in the first section, the particle generation and tracking in Kassiopeia will be discussed in 3.2. The interaction of particles will be addressed in section 3.3.

3.1. The simulation software Kassiopeia

In order to compare the experimental data obtained through measurements, with the simulation, precise calculations and thus a detailed modeling of electromagnetic fields in the corresponding region is desired. In the following, the calculation methods which are applied in Kassiopeia will be discussed.

Magnetic fields
Magnetic fields occuring in the KATRIN experiment originate from both axialsymmetric and non-axialsymmetric coils. The calculation of the latter one is performed according to the Biot Savart Law, which is given by the following equation:

$$d\vec{\mathrm{B}} = -\frac{\mu_0}{4\pi} \cdot \frac{I\vec{\mathrm{r}} \times d\vec{s}}{\mathrm{r}^3}. \tag{3.1}$$

Here, μ_0 stands for the magnetic permeability, $d\vec{\mathrm{B}}$ the magnetic field through the surface segment $d\vec{s}$ and I the electric current generating the magnetic field. The vector $\vec{\mathrm{r}}$ defines the displacement between the wire element and the point where the field is supposed to be computed.
In axialsymmetric systems, the absence of azimuthal dependency allows the calculation of magnetic fields making use of the zonal harmonic expansion method. This method is a special case of the expansions of spherical harmonics, which are proportional to the associated Legendre polynoms and used for field calculations in vacuum. In order to determine the magnetic field at a point $\mathrm{p(z, r)}$, the choice of an arbitrary reference point $\mathrm{z_0}$ on the symmetry axis z is required. This point is called the "source point". Considering this source point as the center of the spherical region inside the coils, the components of the magnetic field within the central convergence region $\rho < \rho_{\mathrm{cen}}$ can be calculated as follows:

$$\mathrm{B_z} = \sum_{\mathrm{n}=0}^{\infty} \mathrm{B_n^{cen}} \cdot \frac{\rho}{\rho_{\mathrm{cen}}}^{\mathrm{n}} \cdot \mathrm{P_n(u)} \tag{3.2}$$

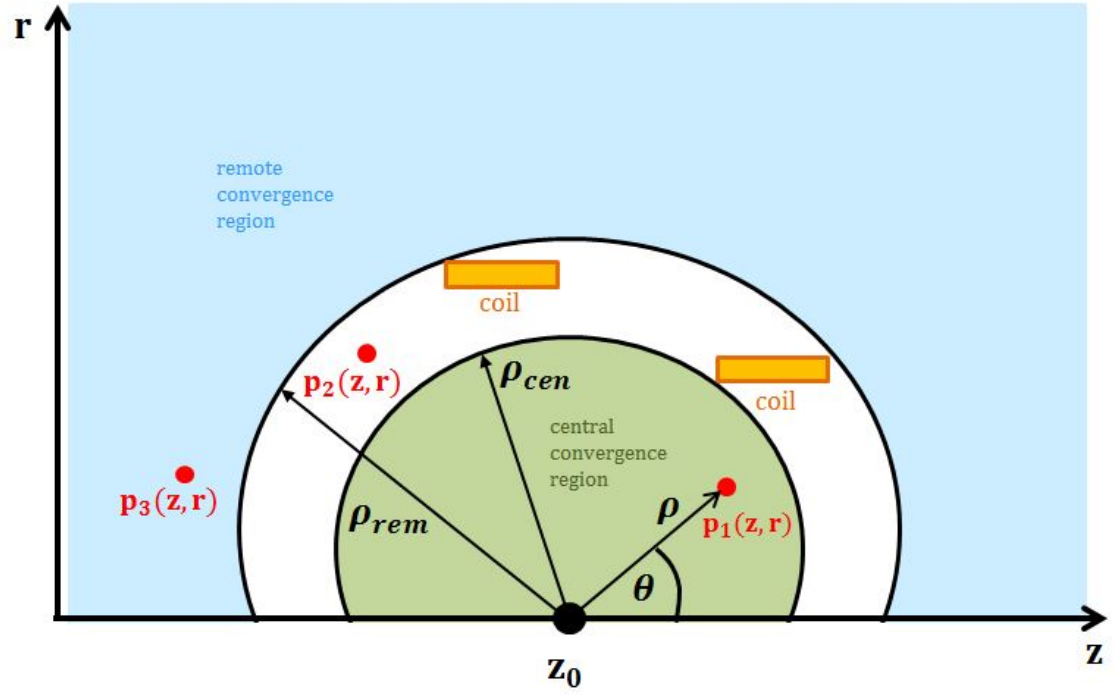

Figure 3.1.: The zonal harmonic expansion method: The magnetic field at $p_1(z,r)$ and $p_3(z,r)$ can be calculated with the zonal harmonic expension method, since they lie within the central (green) or the remote convergence region (blue). The estimation of the magnetic field at point $p_2(z,r)$ is not possible by applying the zonal harmonic method.

$$B_r = -\sin(\theta) \cdot \sum_{n=1}^{\infty} \frac{B_n^{cen}}{n+1} \cdot \frac{\rho}{\rho_{cen}} \cdot P_n'(u). \tag{3.3}$$

As depicted in 3.1, ρ defines the distance between $p_1(z,r)$ and z_0, ρ_{cen} the minimal distance between the source point and the coil and θ the angle between the symmetry axis and the line connecting z_0 with $p_1(z,r)$. The magnetic field at z_0 is given by $B_n^{cen}(z_0)$. The central magnetic source constants $B_n^{cen}(z)$ in general behave proportional to the higher derivatives of on-axis field function $B_0(z)$ at the source point.
However, the central expansion method is only applicable within the convergence region. Defining the greatest distance between the source point and the coil as ρ_{rem}, the remote expansion method can be used for calculations of magnetic fields for the region $\rho > \rho_{rem}$:

$$B_z = \sum_{n=2}^{\infty} B_n^{rem} \cdot \frac{\rho_{rem}}{\rho}^{n+1} \cdot P_n(u) \tag{3.4}$$

$$B_r = -\sin(\theta) \cdot \sum_{n=2}^{\infty} \frac{B_n^{rem}}{n} \cdot \frac{\rho_{rem}}{\rho}^{n+1} \cdot P_n'(u). \tag{3.5}$$

The remote source constants B_n^{rem} (n=2,3,...) refer to the magnetic field sources (coils, magnetic materials) within the remote region. This method of zonal harmonic expansions is equivalent to the multipole expansion in axialsymmetric systems, whereby the first term describes the magnetic dipole, the second one the quadrupole etc.
The rate of convergence in the given cases is dependent on the distance to the source point: smaller distances in the central method and larger distances in the remote method yield higher convergence rates.
Although close spacing of source points allow the field estimations at many points, the magnetic fields can not be calculated in all regions by applying the zonal harmonic expansion

method. In those cases, the magnetic field is determined by solving elliptic integrals. In contrast to the zonal harmonic method, no discretization of the coils is needed.
Nonetheless, the elliptic integral method leads to a large computation time due to the high number of integration steps. For this reason, elliptic integrals are only evaluated in regions where the zonal harmonic methods are not applicable [39].

Electric field calculation
In contrast to the case of magnetic fields, where the inductive current can be meausured directly, charge densities cannot be determined experimentally. The calculation of this quantity is required to enable the determination of the electric field. Discretizing the surface S into N elements leads to a system of linear equations:

$$S = \sum_{j=1}^{N} S_j \tag{3.6}$$

With the following relation between the electrostatic potential

$$U_i = \sum_{j=1}^{N} C_{ij}\sigma_j, \tag{3.7}$$

the individual charge densities σ_j of each surface element j can be estimated. The Coulomb-matrix elements $C_{ij} = C_j(r_i)$ are given by

$$C_j(r_i) = \frac{1}{4\pi\epsilon_0} \cdot \int_{S_j} \frac{1}{|r_i - r_S|} d^2 r_S. \tag{3.8}$$

In the last step, a direct or iterative method, for example the Gauss-Jordan-algorithm [55] has to be applied to solve the linear algebraic equation system.
The software package KEMField, which is included in Kassiopeia, is responsible for electromagnetic field calculations. It uses the boundary element method (BEM) to compute static electric fields. Compared to other methods such as the finite difference method (FDM) or the finite element method (FEM), a high accuracy at relatively short computation time can be achieved by applying BEM. The special feature of this method is the direct calculation of potentials and fields at arbitrary points from charged sources without requiring a discretization of the whole volume. Due to the fact that only a 2dimensional surface has to be split into segments instead of a 3dimensinal volume, a smaller number of degrees of freedom has to be considered which leads to a shorter computation time.
In case of axially symmetric electrodes, the boundary element method would lead to the numerical calculation of elliptic integrals, which is time consuming. For this reason, the zonal harmonic expansion method, which was explained before is used instead. The computation time is 2-3 orders of magnitude faster compared to the calculation of elliptic integrals.
In KEMField, both Dirichlet boundary conditions (metal surfaces) and Neumann boundary conditions (dielectrics) can be considered for electric field computations.

3.2. Particle generation and tracking

At the beginning of each simulation, the corresponding particles have to be initialized. Additionally, it is necessary to set terminators to stop the simulation at a certain point. In addition, Kassiopeia requires the selection of calculation methods in order to track the given set of particles. These settings will be discussed in the following subsections.

3.2.1. Generators and Terminators

The type of particle, and thus the inherited properties (mass, charge), are specified by either the particle identification number (pid) or the string identification. Adjusting the four generators time, position, energy and direction in addition allows the creation of particles in a user-defined region in a specified configuration. There exist several possibilities of value generators available in Kassiopeia, for example the uniform or the gauss distribution. The termination conditions for the simulated particles are defined by the so-called terminators. Once a given condition is met, the simulation is stopped. Kassiopeia offers different sorts of terminators, that for example stop the particle tracking when a specific z-position is reached or when the kinetic energy of the particle increases below a certain value.

3.2.2. Step size controls

To finally enable the propagation of the given particle, a calculation method has to be selected. The accuracy of the particle tracking/propagation depends on the calculation method of the corresponding trajectory. Kassiopeia allows different algorithms for the computation which will be introduced in this section. Either the exact calculation or the adiabatic method can be selected for the computation of the particle track. The first method calculates the trajectory by solving the equation of motion according to the Runge-Kutta algorithm, while the second one refers to the guiding center along the corresponding magnetic field line, as depicted in 3.2.
The adiabaticity decreases rapidly in the region of the pre-spectrometer, where the simulations were carried out for the most part. For this reason, it is recommended to apply the exact calculation method for the simulation of ions. An energy conservation in the order of 10^{-8} is prerequisite for a sufficient accuracy of the performed simulations. In order to achieve this, the control options must be adjusted respectively. Due to the fact that the computation time increases with accuracy, a compromise between these two parameters must be found. Kassiopeia allows the adjustment of two options: the control length and the control cyclotron. The control length defines a fixed step size between two calculation points. For a given control length, the accuracy decreases with higher magnetic fields. In contrast to it, the control cyclotron sets the number of steps per cyclotron period. In this case, the accuracy increases with lower magnetic fields. Simulations with different settings

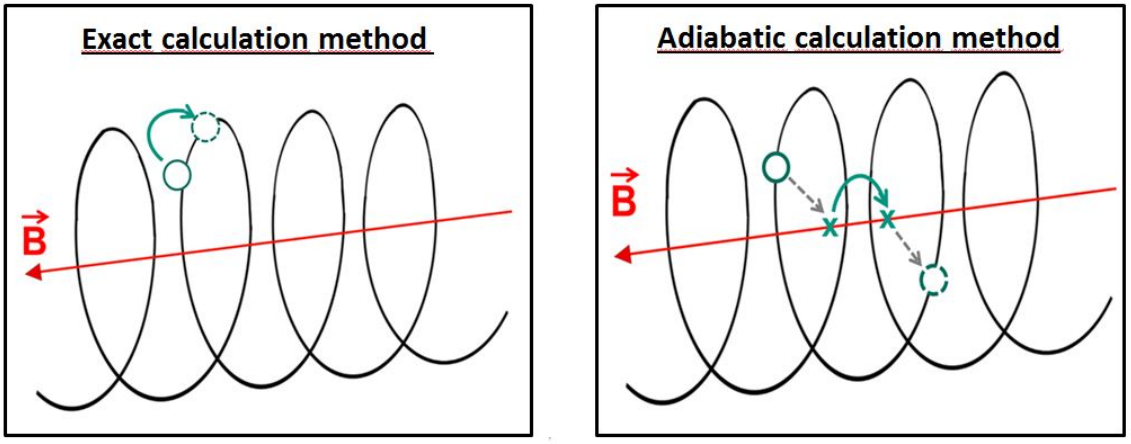

Figure 3.2.: Step size control options in Kassiopeia: The exact calculation method is depicted on the left side. In this case, the position of the particle is calculated according to the Runge-Kutta algorithm (reference). In contrast to it, the adiabatic calculation method, shown on the right part, refers to the corresponding magnetic field line.

were performed to find the appropriate parameter range within a reasonable computation time as will be treated in more detail in section 3.4.

3.3. Particle interactions

Interactions, which are expected to occur during the tracking process of the particle of interest, can also be considered in Kassiopeia. Using the software package KESS [61], which is included in the Kassiopeia framework, simulations of electrons in silicon including interaction processes is enabled. This section gives an overview of the interactions processes which were applied to the performed simulations.

3.3.1. Scattering processes

In general, interaction processes can be categorized into volume and surface interactions. In order to make a decision on the scattering type, a so-called scattering calculator is implemented. It is responsible for the evaluation of the cross section considering the particle's state and therefore for the decision, which interaction process is supposed to be executed.
A volume interaction process is executed considering the probability which is given by:

$$\mathrm{P(t)} = 1 - \exp(-\frac{\mathrm{t \cdot v}}{\lambda}) \tag{3.9}$$

with the mean free path

$$\lambda = \frac{1}{\mathrm{n} \cdot \sigma} \tag{3.10}$$

where λ is the mean free path and σ the cross section. Considering the initial and final position of the particle on step, Kassiopeia evaluates the mean values for n,v and σ, where a separate density module is responsible for the calculation of the density of the given medium. The total cross section defines the sum of all individual cross sections of interaction processes for the given scattering module.
The time between two scattering processes is determined by the formula

$$\mathrm{T_{scat}} = -\ln(1 - \mathrm{P})\frac{\lambda}{/}\mathrm{v}. \tag{3.11}$$

Here, the value for P is drawn from a uniform distribution between 0 and 1. Comparing the scattering time with the time it takes the particle to complete the current step leads to one of the two following cases:
1) $\mathrm{T_{scat}} > \mathrm{T_{step}}$: No scattering takes place.
2) $\mathrm{T_{scat}} < \mathrm{T_{step}}$: In order to determine the properties of the particles as exactly as possible at the time just before the scattering process, its trajectory is recalculated by considering a step size identical to the scattering time.
Afterwards, the contribution of each scattering process to the cross section is determined. Thus, the decision on the process to be executed (basically elastic or inelastic scattering) is made. Once the scattering process takes place, the properties of the particle are modified and new particles optionally created.
The dominant gas species in the KATRIN spectrometers, where most of the simulations were performed, are molecular hydrogen and water vapor. The ionization cross sections for these two targets are implemented, as well as the angular and energy distribution of the corresponding secondary electrons.
The second process available in Kassiopeia is given by the surface interaction. In contrast to the surface interaction process, which takes place stochastically, this sort of interaction

is only enforced, when the particle reaches a specific surface. Such an interaction can lead either to a transmission through the surface or a reflection. Both cases will result in a change of the particle properties accordingly. The scattering type, as well as the energy and angular change when crossing an interface between different materials are of interest. Especially the scattering processes of electrons between the vacuum and the solid silicon detector play an important role in KATRIN. For this purpose, a specific software package called KESS (KATRIN Electron Scattering in Silicon) was implemented in Kassiopeia, which will be introduced in the next subsection.

3.3.2. Software package KESS

To achieve the required sensitivity in the KATRIN experiment, it is necessary to assess the detection efficiency of the focal plane detector, since it affects the systematic and statistical errors on m_ν^2. This quantity is not fully included in the current treatment of uncertainties. Therefore, it is desirable to model the backscattering as well as the dead layer effects of the FPD precisely. For this reason, the Monte Carlo simulation software package KESS (KATRIN Electron Scattering In Silicon) was developed. It is embedded into Kassiopeia and enables the modeling of surface interactions in more detail and allows the evaluation of energy loss and angular changes of the tracked particles [61]. KESS was primarily written to fulfill the needs of the KATRIN experiment. However, it is also possible to apply KESS for simulations which are not related to the KATRIN-experiment. As will be discussed in appendix B, electron scattering simulations using KESS are also performed for the TRIMS-experiment.

3.4. Preparatory simulations in the KATRIN pre-spectrometer

Within the scope of this thesis most part of the simulations were carried out in the pre-spectrometer of KATRIN with regard to ion trajectories.
Besides electrons created by β-decay processes, ions occur in the KATRIN experiment which in the first place distinguish from electrons by their mass. In addition, electrons that reach the main-spectrometer typically are high energetic and therefore possess mass in the keV range, while ions show energies in the range of $E \in [1; 100]\,\mathrm{eV}$.
Within the scope of previous works, simulations with Kassiopeia were performed mainly for electrons. For this reason it is crucial to determine appropriate simulation settings with regard to the movement of ions in the spectrometer section beforehand.
After highlighting the properties of the pre-spectrometer with respect to the trajectory of ions in subsection 3.4.1, an overview of the preparatory simulations is given in subsections 3.4.2 and 3.4.3.

3.4.1. The adiabaticity in the pre-spectrometer

An adiabatic invariant of a physical system describes a property that stays constant while changes occur slowly. In the KATRIN experiment, such a property plays an important role in the MAC-E filter with the adiabatic invariant of the orbital magnetic moment pointed out in equation 2.4.
Since the KATRIN experiment aims a precise investigation of the energy spectrum of β-electrons from tritium decay, it is crucial to control the trajectory of electrons. As shown in figure 3.3, the curve of the magnetic field drops steeply in the spectrometer section. Once the transformation of the transversal energy component of the particle $E_\perp$ into its parallel component $E_\parallel$ is not proportional to the change of the magnetic field within one cyclotron motion, the adiabaticity is violated. In this case, a sudden change of the angular motion of the particle is initiated. Such an uncoltrolled change can lead to the storage of

the particle in the spectrometer section, which would lead to a higher background rate and therefore is not desired. In order to ensure the adiabatic guidance of electrons through the spectrometer section, the focus of the MAC-E filter design was laid respectively. The movement of ions however differ from those of the electrons. For this reason, the adiabatic guidance of ions is not guaranteed.
The goal of the simulations performed in the frame of this work is not the investigation of ions which are stored in the spectrometer section, but of those that start at the front of the pre-spectrometer and are transmitted into the main spectrometer. In order to allow sufficiently high statistics for such simulations, it is desired to avoid ions from being trapped. Hence, the corresponding simulation settings have to be adjusted respectively. Since the adiabatic calculation method does not apply to ions, all preparatory simulations were carried out by making use of the exact calculation method.

3.4.2. The influence of step size control options

Apart from the calculation method, the appropriate adjustment of step size control options is crucial in order to reach a sufficiently high accuracy. At the same time, it is desired to perform simulations within an adequate computation time. In order to find a reasonable compromise between these two parameters, studies targeting the determination of appropriate simulation parameters are required.
As mentioned in subsection 3.2.2, the step size control in Kassiopeia is categorized in two options: the control length and the control cyclotron. One condition for a sufficiently high accuracy is given by the energy conservation in the range of 10^{-8}.
In order to study the influence of the control options on the trajectories and finally the accuracy, simulations were as a first step performed with only activating the control length. Afterwards, the control cyclotron was applied in addition.

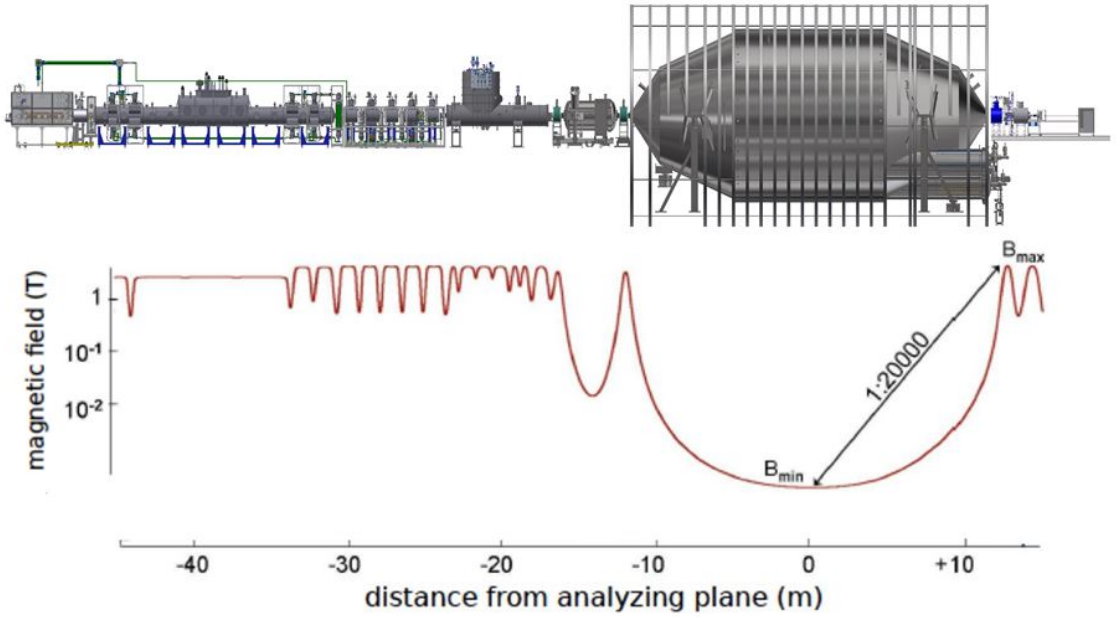

Figure 3.3.: The magnetic field of the KATRIN beamline: The magnetic field strength through the KATRIN beamline is illustrated. It can be seen that the B-Field drops steeply in the region of the pre-spectrometer.

Table 3.1.: Simulation parameters: The overview of the parameters which were set before starting the simulation are presented.

simulated events	1000
initial energy (fixed)	100 eV
initial polar angle to B	35°
initial radius (fixed)	0.01 m

3.4.2.1. Simulations with activated control length

By performing simulations with different control lengths and comparing the corresponding results, the influence of this setting on the accuracy was investigated.
Among other factors, the dimension of the spectrometer plays a decisive role when it comes to the adjustment of the control length. The size of the spectrometer determines the range of the trajectory lengths which in turn limit the scale of the control length. Since the diameter of the pre-spectrometer amounts to approximately 1.7 m, it seems reasonable to allow a maximum control length of

$$\Delta_{\mathrm{CL,max}} = 0.01\,\mathrm{m}. \tag{3.12}$$

Starting with this value, the quantity was stepwise reduced by one order of magnitude. The influence of this property was investigated by comparing the trajectories respectively with regard to their path length. Figure 3.4 shows the path lengths of three trajectories which belong to three different control lengths. The simulation settings are shown in table 3.1.

It can be seen that the difference in the path lenghts for simulations with control lenghts of $1 \cdot 10^{-3}$ m and $1 \cdot 10^{-4}$ m do not differ much from each other while the blue curve

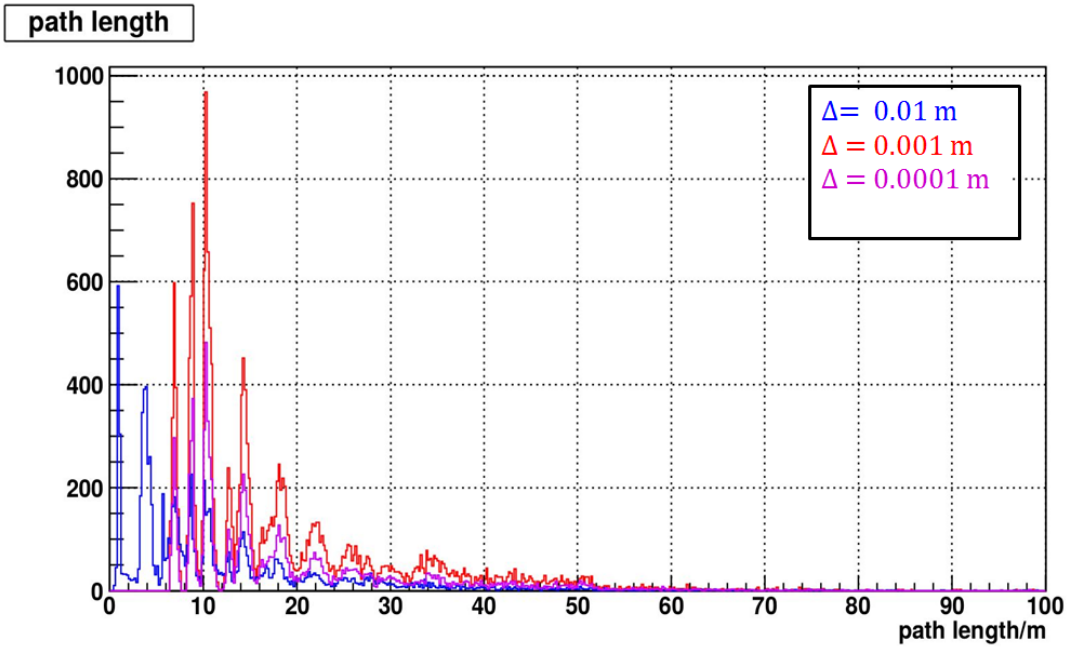

Figure 3.4.: The length of different ion trajectories: The path length was determined for different control length options. The blue curve corresponds to a control length of $1 \cdot 10^{-2}$ m, while the red curve belongs to a control length of $1 \cdot 10^{-3}$ m and the violet one to $1 \cdot 10^{-4}$ m.

corresponding to a control length of $1 \cdot 10^{-2}$ m shows in contrast relatively short path lenghts. Considering the diameter of the pre-spectrometer of approx 1.6 m and a length of around 4.5 m, it can be concluded that trajectories with path lengts of greater than 20 m correspond to trapped ions.
Such a situation is depicted in figure 3.5. In case of a trapped ion, the movement evolves to a chaotic movement. Thus, the final position of the ion only depends on stochastic processes. The goal of this investigation lies not in the behaviour of trapped ions, but on the influence of the control length on ions which are supposed to either be transmitted or to hit the vessel of the pre-spectrometer on the inner side. For this reason, ions indicating path lengths of greater than 20 m were excluded for further analysis. In order to visualize the comparison, the reference control length was chosen to $1 \cdot 10^{-3}$ m. In doing so, the difference between the final position corresponding to trajectories simulated with different control lengths was calculated. The outcome is illustrated in figure 3.6. It is striking that final position of trajectories with a control length of $1 \cdot 10^{-2}$ m show more discrepancies to the reference trajectories. In contrast, simulations which were performed with a control length of $1 \cdot 10^{-4}$ m mostly show differences in the order of <0.1 m.
The computation time was found out to scale proportional to the chosen control length: by performing a simulation with a control length of $1 \cdot 10^{-3}$ m, the computation time is reduced by a factor of ten compared to a simulation with $\Delta_{\mathrm{CL}} = 1 \cdot 10^{-4}$ m.
Since a difference of <0.1 m with regard to the final positions was considered acceptable in the pre-spectrometer, the energy conservation for this control length was checked in the next step.
To do so, the ratio between the initial energy of an ion and its final energy was calculated. The energy conservation is assumed to be satisfied if the condition

$$\mathrm{E}_{\mathrm{ratio}} = \frac{\mathrm{E}_{\mathrm{initial}}}{\mathrm{E}_{\mathrm{final}}} = 10^{-8} \tag{3.13}$$

is fulfilled. In addition, simulations were carried out at different magnetic field settings in the pre-spectrometer. The obtained results are shown in table 3.2.

It can be seen that the violation of the energy conservation increases with higher magnetic fields. These results match with the expectations since the radius of the cyclotron motion of an ion in a higher magnetic field is larger than in a region with a low magnetic field. At the same time, this observation demonstrates the need of the cyclotron control which was turned on in the next step.

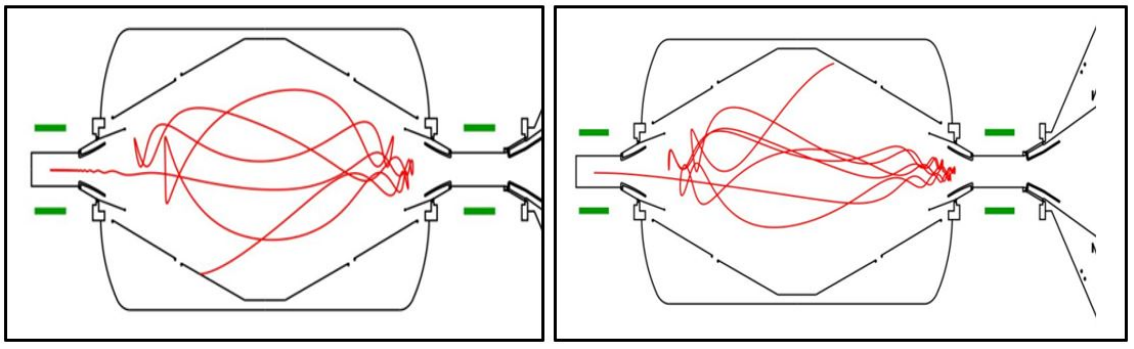

Figure 3.5.: Trajectories of trapped ions: Left: The simulation was performed with a control length of $1 \cdot 10^{-2}$ m. The ion hits the pre-spectrometer at the bottom side on the left after moving back and forth through the pre-spectrometer. **Right:** The trajectory corresponds to a control length of $1 \cdot 10^{-3}$ m. In contrast to the case on the left part, the ion hits the pre-spectrometer on the upper right part.

Table 3.2.: Energy conservation at different magnetic field settings: The ratio between the initial kinetic energy and the final kinetic energy was calculated for 1000 simulated events at different magnetic field settings. The mean value was determined via ROOT and are shown below.

Magnetic field	E_{ratio}
20 %	10^{-8}
40 %	10^{-4}
80 %	10^{-2}

3.4.2.2. Simulations with both control options

It is known from previous simulations that a cyclotron control of

$$\Delta_{CC} = \frac{1}{16} \tag{3.14}$$

satisfies the energy conservation and thus is an appropriate value to be set for electron tracking simulations. Since ions possess higher masses, they show larger cyclotron radii. Therefore, a smaller value must be chosen for the cyclotron control in order to reach a sufficiently high accuracy.
In order to investigate the influence of the cyclotron control option, simulations were carried out applying two settings. In both cases, the control length was set to $1 \cdot 10^{-3}$ m. The obtained results are shown in the table 3.4 below.

As can be seen, the energy conservation is satisfied for the stepsize control options is

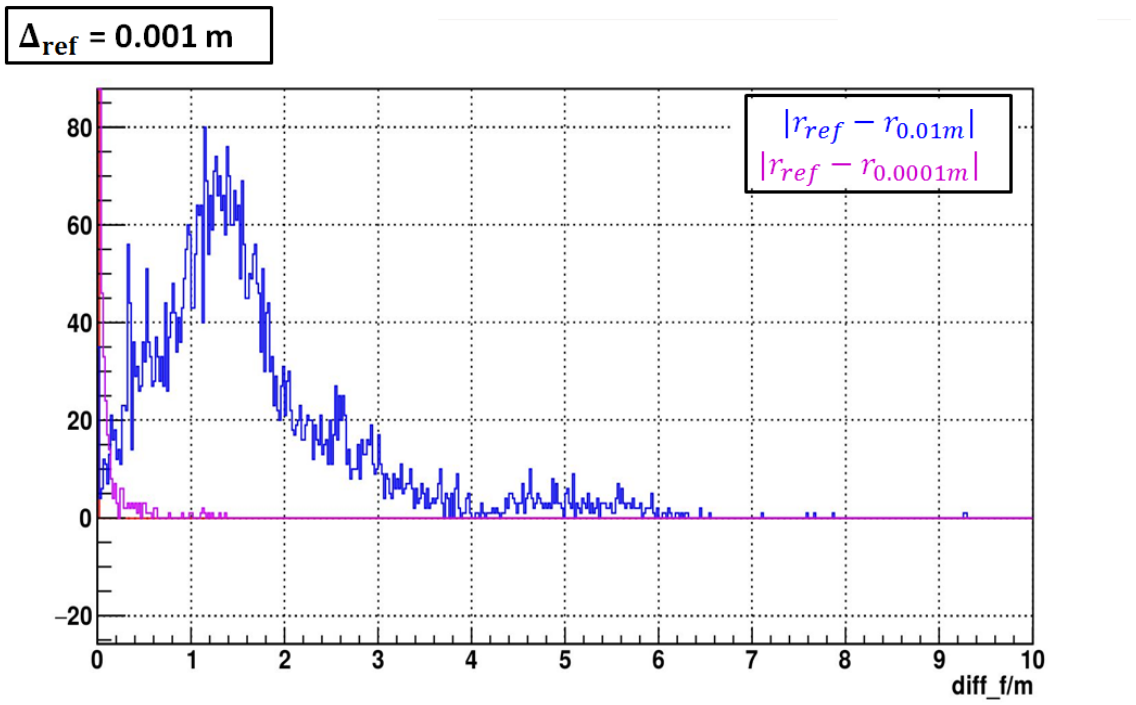

Figure 3.6.: Trajectory lengths of non-trapped ions: The path length was determined for different control length options. By choosing the reference control length of 0.001 m, the difference between the final positions were calculated for the trajectories belonging to the other two control lengths. Ions which trajectory lengths greater than 20 were exlcluded.

Table 3.3.: Influence of the cyclotron control option: The violation of energy conservation was determined for two different cyclotron control options.

Magnetic field setting	$\Delta_{CC} = 1/20$	$\Delta_{CC} = 1/40$
20 %	10^{-8}	10^{-9}
40 %	10^{-7}	10^{-10}
80 %	10^{-5}	10^{-11}

activated with

$$\begin{aligned} \Delta_{CC} &= \frac{1}{40} \\ \Delta_{CL} &= 0.001\,\mathrm{m}. \end{aligned} \tag{3.15}$$

The computation time for ion tracking simulations performed with these settings amounts to

$$t_{comp} \approx 82.18\,\mathrm{s} \tag{3.16}$$

for 1000 events which is acceptable.
As a last check with regard to the energy, the output values of Kassiopeia which are stored in a ROOT file was verified by a short analytical calculation. To do so, one ion simulation was carried out with a seed providing an ion trajectory which equals a straight line through the spectrometer. Considering the mass m of the simulated ion (D_2^+) and its initial energy E, the corresponding velocity v was calculated via

$$v = \sqrt{\frac{2E}{m}}. \tag{3.17}$$

Comparing the obtained value with the corresponding output of the ROOT file led to the conclusion that the calculation was performed properly by the simulation software.
Thus, it was decided to perform all ion simulations in the pre-spectrometer with the values given in equation 3.15.

3.4.3. Influence of the ion mass on the accuracy

A further parameter that was investigated with regard to the energy conservation and thus the accuracy in the simulation is the ion mass. As will be referred to in the following chapters, different ion species were simulated through the spectrometer section. It was mentioned in subsection 3.2.2, that the cyclotron control is defined by a fraction and therefore behaves relatively to the performed gyration, which in turn depends on the particle mass. Hence, it is expected that an ion with higher mass and thus showing a greater cyclotron radius leads to a higher degree of violation of the energy conservation due to a smaller number of steps.
In order to study the influence of the ion mass, D^+-ions were simulated at the same conditions and the same seed. Again, simulatios were carried out at three different magnetic field settings. The corresponding results are displayed in table 3.4.
It can be seen that the violation of the energy conservation increases with the ion mass. This observation agrees with the theoretical expectation above. The influence of the particles mass on the accuracy of the calculation of the trajectory in Kassiopeia was demonstrated. However, it is also clearly shown that the condition with regard to the accuracy of the tracking simulation in equation 3.13 is fulfilled for all three ion species D^+, D_2^+ and D_3^+. Thus, all simulations corresponding to such particles which will be the topic of the following chapter were carried out with

$$\begin{aligned} \Delta_{CL} &= 0.001\,\mathrm{m} \\ \Delta_{CC} &= 1/40 \end{aligned} \tag{3.18}$$

Table 3.4.: Violation of energy conservation for different ion species: Here, the values of the ratio in equation 3.13 which is a measure for the violation of the energy were calculated for three different ion species.

Magnetic field setting	D^+	D_2^+	D_3^+
20 %	10^{-11}	10^{-9}	10^{-8}
40 %	10^{-12}	10^{-10}	10^{-9}
80 %	10^{-11}	10^{-11}	10^{-8}

4. Blocking and transmission efficiency of the pre-spectrometer

As explained in section 2.3, different types of ion induced background processes occur in the KATRIN experiment. It is crucial to prevent ions from entering the main spectrometer in order to reach the required background rate. A maximum residual ion flux of $2 \cdot 10^2$ions/s into the main spectrometer is desired. At the same time, the number of ions which enter the main spectrometer must be reduced by at least two orders of magnitude compared to the amount of ions entering the pre-spectrometer.
Besides ions which originate from processes within the spectrometer section, a high number of ions are created in the WGTS. Different from electrons, ions are not affected by the pumping processes. Hence, it is of high interest to investigate the ion blocking efficiency of the pre-spectrometer. To do so, measurements have been performed during the "First Light Plus" measurement campaign in November 2016. By employing an ion source, deuterium ions were artificially created and transported through the KATRIN beamline. Different parameters as the magnetic field and potential settings on the electrodes of the pre-spectrometer were varied, while the rate of the ions which reached the main spectrometer was estimated by measuring the corresponding secondary electron rate on the FPD.
Within the scope of this thesis, simulations of ion trajectories have been performed focusing on different aspects. In section 4.1, a short overview about the ion blocking measurements will be given. Section 4.2 deals with simulations of deuterium ion trajectories targeting the estimation of parameters that could not be determined experimentally. In contrast, section 4.3 refers to simulations with the goal to suggest configurations for measurements which are planned to be performed during future measurements.

4.1. Ion blocking measurements during First Light Plus

One goal of the first KATRIN beamline commissioning measurements which were carried out in November 2016 was the validation of the functionality of the ion blocking devices mentioned in chapter 2. For this purpose, an ion source was installed at the Rear Wall which will be introduced in the following.
The assessment of the measurement data can be made by comparing them with the corresponding simulation results. Discrepancies between the measured and simulated data would indicate that processes had not been taken into account which in turn would demonstrate the need for more studies in this field, as will be discussed in chapter 5. The software Kassiopeia provides a highly accurate model of the KATRIN experiment, as had been investigated in previous works. Hence, all simulations in the following were carried out by making use of Kassiopeia.
As pointed out in chapter 3, the start of each simulation requires the adjustment of certain parameters. However, the corresponding quantities cannot be measured directly. For this reason, such parameters have been determined by means of Kassiopeia simulations which will be discussed in more detail in subsection 4.2. In order to create ions, the ELIOTT

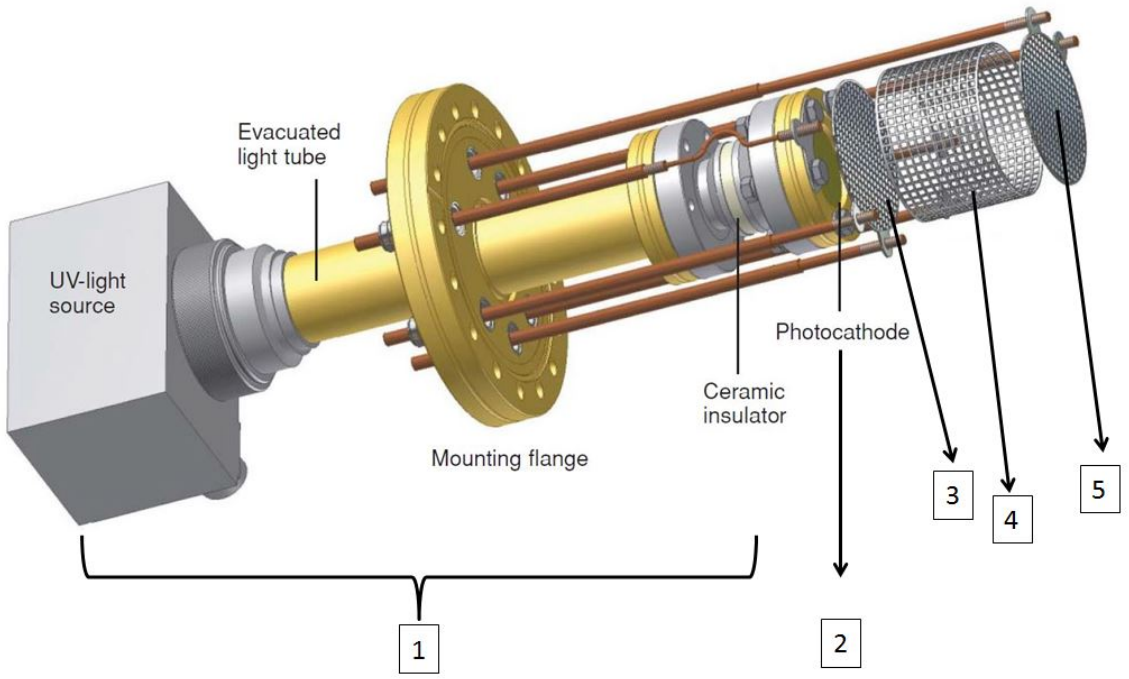

Figure 4.1.: The ELIOTT ion source: The ion source was installed in the Rear wall in order to create artificially created ions. Figure adapted and modified from [53].

(ELectron impact IOn source To Test the DPS) ion source [53] was employed for the ion measurement phase in November 2016. A schematic overview of this ion source is shown in figure 4.1.

In the following, the components of ELIOTT will be introduced:

1. **Light Source:** The first section includes the light source which is followed by a tube, a mounting flange and a ceramic instulator. Vacuum-sealed deuterium-discharge processes take place in the Hamamatsu L10366 lamp that lead to the emission of UV Light.

2. **Photocathode:** Due to photons hitting the cathode, electrons are created by the photoeffect.

3. **Electron acceleration grid:** A potential difference between the photocathode and this grid is applied in order to accelerate the electrons.

4. **Cylindrical shaped electrode:** This component is coaxial with the beam tube and is kept at a slightly lower potential than the acceleration grid. The main function of this electrode is the creation of additional volume for ionization processes by screening the ground potential of the beam tube.

5. **Ion-extraction grid:** The experimental setup of ELIOTT is completed by the ion-extraction grid, connected to a slightly more negative potential than the photocathode. In order to confine the electrons into the space between 2 and 3, the ions are forwarded in forward direction.

During the First Light measurement campaign, ELIOTT was installed at the Rear Wall of the KATRIN setup. In this way, deuterium ions were created and propagated through the whole beamline.
Besides the validation of the functionality of dipole systems which were installed into the DPS as explained in chapter 2, one goal of the measurements was to investigate the ion

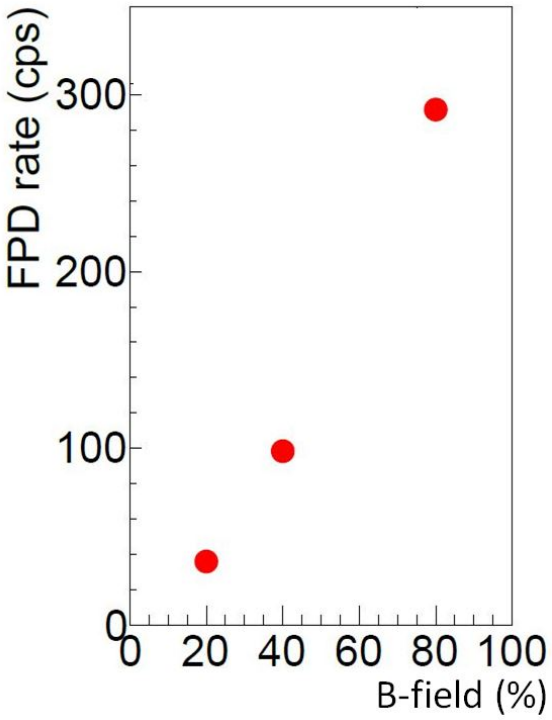

Figure 4.2.: Secondary electron rate over magnetic field strength: The measurement data of secondary electrons originating from ions which scatter with residual gas molecules is shown over the magnetic field strength.

transmission efficiency of the pre-spectrometer. The investigation of the ion transmission efficiency of the pre-spectrometer requires a good understanding of the movement of ions in this section. In contrast to electrons, ions are not guided by adiabatically in the spectrometer section. For this reason, measurements with respect to the dependency of the ion transmission on the magnetic field were performed.
Figure 4.2 shows the secondary electron rate on the FPD at different magnetic field settings for the pre-spectrometer magnets, where B = 100 % corresponds to a magnetic field strength of B = 4.5 T. Since the experimental setup of KATRIN does not enable the direct measurement of the ion rate, conclusions are drawn by means of the rate on the FPD caused by secondary electrons originating from scattering processes of ions on residual gas molecules.
It can be seen in figure 4.2 that the secondary electron rate increases at higher magnetic field. This observation agrees with the expectation from a analytical point of view based on the conservation of the magnetic flux:

$$\Phi = \int_{\mathrm{A}} \vec{\mathrm{B}} \mathrm{dA}. \tag{4.1}$$

Assuming a circle with radius r for the cross section of the flux tube yields

$$\mathrm{B} \propto \frac{1}{\sqrt{\mathrm{r}}}. \tag{4.2}$$

Increasing the magnetic field strength leads to a smaller initial radial distribution of the ions. Due to such a confinement of the ions in radial direction, more ions would move in straight forward direction at a higher magnetic field which leads to a higher probability of transmission.
The measurement data do not provide detailed information with respect to the correlation between the applied magnetic field and the secondary electron rate which in turn is a

measure of the ions. For this reason, simulations are needed, which will be discussed in the following subsection 4.2.

4.2. Ion simulations in the pre-spectrometer

In order to propose configurations for future ion measurements based on simulation results, it is essential to verify the reliability of simulations. All simulations that will be discussed in the following were performed with the KATRIN simulation software Kassiopeia which was introduced in chapter 3.
As discussed in section 3.2, the start of each simulation requires a selection of certain settings and parameters. In addition, it was pointed out that a sufficient accuracy of the simulation is assumed to be reached by an energy conservation in the order of 10^{-8}. The appropriate settings with regard to the step size control options were investigated in section 3.4 and applied in the following simulations.

In order to compare the simulation results with the measurement data, it is also crucial to match the parameter range in the simulation as well as possible. However, the setup of the KATRIN experiment does not provide the possibility to determine the radius and angle of the ion beam in the PS1 magnet. For this reason, such parameters had to be estimated through simulations.
The determination of the approximate radius and the angular distribution of ions that started in the PS1 magnet was made by means of the following approaches.

4.2.0.1. Simulation of ions through the beamline

The geometry package "The Global Bag" has been implemented in January 2016 in Kassiopeia and represents the experimental setup of the whole KATRIN beamline. In contrast to the former developed package The Bag, it takes misalignments of the components which were experimentally estimated into account and therefore provides a more detailed setup of KATRIN for simulations.
For this reason, this package was employed for the simulation of deuterium ions in the region between Rear Wall to the PS1 magnet located at the entrance of the pre-spectrometer. Since the calculation of electromagnetic fields is not enabled in The Global Bag yet, simulations in the spectrometer section were performed with The Bag.
The diameter of the hole in the Rear Wall is

$$\mathrm{d_{RW}} = 5\,\mathrm{mm}. \tag{4.3}$$

This value defines the initial radius of the ion beam created by ELIOTT. Simulations were performed based on a homogenous spatial distribution of D_3^+-ions covering an energy range of $E \in [1; 100]$.. Figure 4.3 shows the trajectory of an ion beam through the KATRIN beamline. The radius of the ion beam at the entrance of the pre-spectrometer was calculated with

$$\mathrm{r_{global,i}} = \sqrt{\mathrm{x^2_{global,i}} + \mathrm{y^2_{global,i}}} \tag{4.4}$$

where $\mathrm{x_{global,i}}$ and $\mathrm{y_{global,i}}$ are the x- and y- coordinates of the ion beam terminated in the PS1 magnet which are stored in a ROOT file. The obtained results for the radius and the angular distribution of the ions in the PS1 magnet are given by

$$\begin{aligned} \mathrm{r_{global,i}} &= (4 \pm 2) \cdot 10^{-3}\,\mathrm{m} \\ \theta_{\mathrm{global,i}} &\in [0°; 65°]. \end{aligned} \tag{4.5}$$

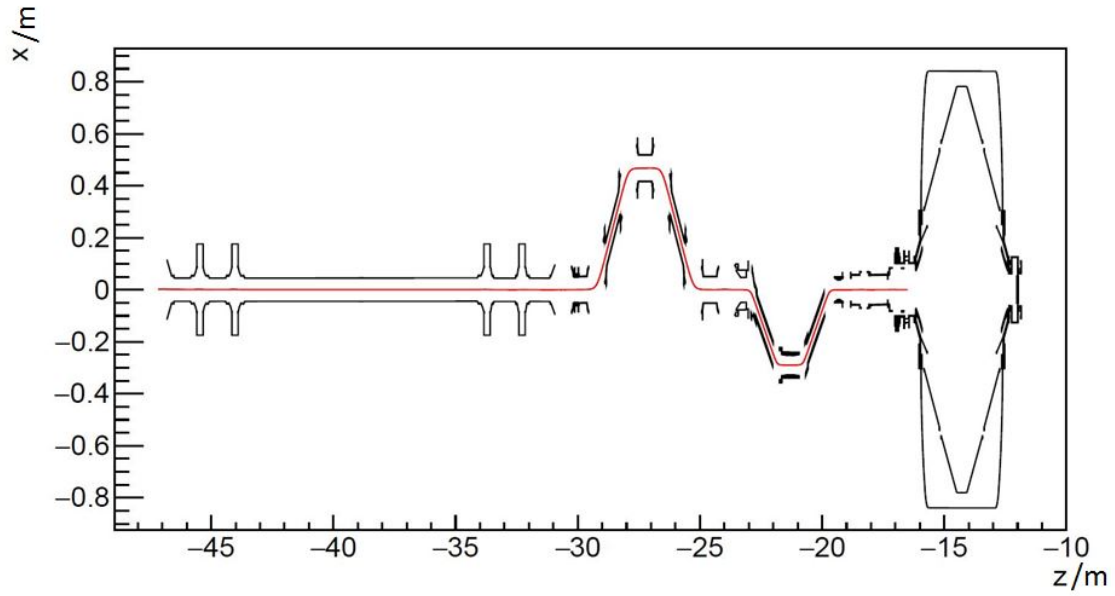

Figure 4.3.: The KATRIN beamline in Kassiopeia: The red line illustrates the propagation of a D_3^+- ion the Rear Wall to the entrance of the pre-spectrometer. The geometry package The Global Bag was used for the corresponding simulations.

4.2.0.2. Fit of simulation result to measurement data for different magnetic field settings

As mentioned above, ion measurements were performed at three different magnetic field settings in the pre-spectromter. The magnetic field setting was kept constant for a certain measurement time and afterwards increased. In order to consider more data points, the secondary electron rate was estimated subsequently for B-field settings in between the static measurements. Figure 4.5 illustrates a schematic increase of the magnetic field and the electron rate measured at the FPD. It is required to determine the relation between the secondary electron and the magnetic field in order to allow a comparison with the simulation result. Since the magnetic field was not kept at a constant value but increased linearly, it is important to find an appropriate binning for the considered time period for the allocation of the measured values to each other.

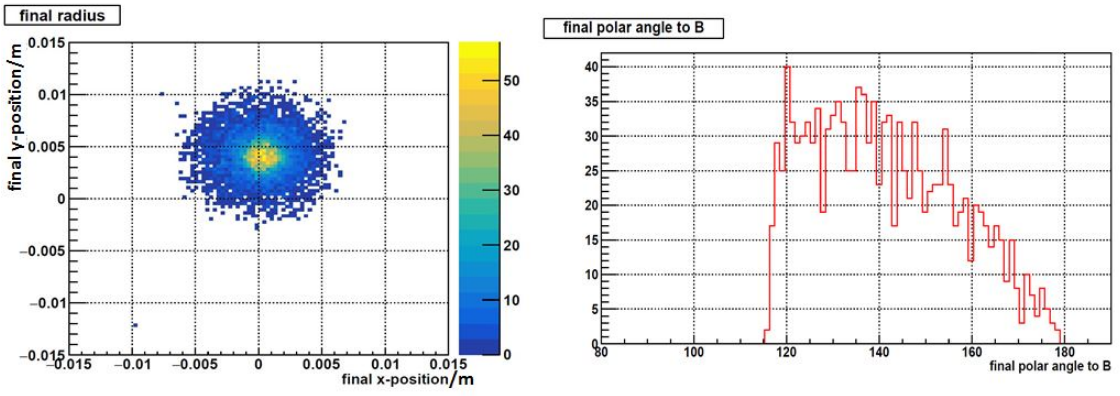

Figure 4.4.: The radial and angular distribution of D_3^+-ions which reach the PS1 magnet: Right: The radial distribution of the ions is shown. **Left:** The distribution over the polar angle to B is shown. The direction of the B-field is antiparallel to the z-axis.

As can be seen in the right part of figure 4.5, the increase within a time period of 200 s seems nearly linear. Based on this assumption, the binning was chosen to

$$\Delta t_{\mathrm{bin}} = 60\,\mathrm{s}. \tag{4.6}$$

In doing so, more than three values could be considered from the measurement.
In order to compare the measurement data with corresponding simulations, D_3^+-ions were started in the center of the PS1 magnet. Again, the distribution of the ions was assumed to be homogenous over the radius of the flux tube. Detailed settings of this simulation are shown in table 4.2.
As a first step, the dependency of the D_3^+-ion transmission probability through the pre-spectrometer on the radius of the flux tube was calculated for different magnetic field settings. As figure 4.6 illustrates, the form of the curves change with the applied magnetic field. This plot allows to estimate the transmission probability at a certain initial radius of the ion beam.
Afterwards, a fit function was written in ROOT with the purpose to fit the simulation results to the measurement data, namely the transmission probability from the simulation to the secondary electron rate from the measurement. Therefore, the measured secondary electron rate at the FPD for non-static magnetic fields was obtained by considering equation 4.6. The data points in the right part of figure 4.6 represent the measured data while the line refers to the simulation results.
By performing a fit with ROOT with three parameters listed below it was targeted to determine the initial radius of the D_3^+-ion beam in the PS1 magnet. Taking into account the radial dependency of the transmission probability illustrated on the left part of figure 4.6 from simulation results, the measured secondary eletron rate was fit to the simulated transmission rate.

To do so, the following parameters which are independent from each other were passed to the fit function:

- **Normalization constant C:** Since the amount of ions which entered the pre-spectrometer in the measurement is not known, the determination of this quantity is

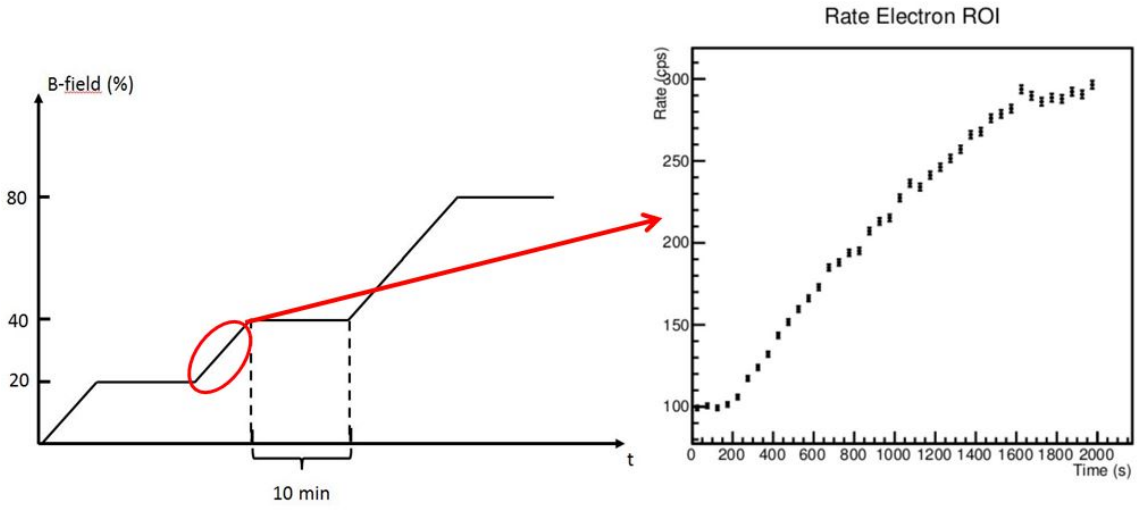

Figure 4.5.: The increase of the magnetic field strength and the measured electron rate: Right: The schematic increase of the magnetic field over time is illustrated. Static measurements at 20%, 40% and 80% were performed for about 10 min. **Right:** The measured electron rate on the FPD during the elevation of the magnetic field from 20% to 40% is shown.

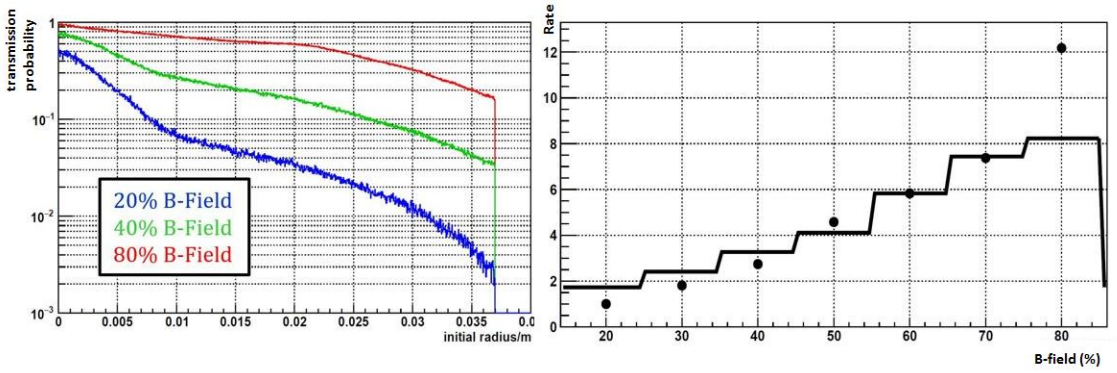

Figure 4.6.: Transmission efficiency and fit of simulation result to measurement data: Left: The transmission efficiency of the pre-spectrometer over the initial radius of the ion beam is shwon for different magnetic field settings. **Right:** The simulation results were fit to the measurement data by employing ROOT. The black points depict the meausurement data while the black line illustrates the fit performed by ROOT.

required. The results for the transmission efficiency in the simulation are multiplied by the obtained value.

- **Initial radius of the ion beam**: By assuming a Gaussian beam profile described by the equation

$$\frac{1}{\sigma \cdot \sqrt{2\pi}} \cdot \exp^{-\frac{1}{2}\left(\frac{x-\mu}{\sigma}\right)^2}, \tag{4.7}$$

two parameters were treated as fit parameters:

1. Mean value of the radius/beam profile μ
2. The FWHM (Full Width at Half Maximum) of the ion beam, which is defined as follows:

$$\mathrm{FWHM} = 2 \cdot \sqrt{2 \cdot \ln(2)}\sigma. \tag{4.8}$$

Here, the range of the radius is limited to the maximum radius of the flux tube of 0.037 m.

The corresponding fit and therefore the estimation of the three parameters in the given ranges above was performed by ROOT[1], employing the minimization method MINUIT2[2]. The illustration of the fit is shown in figure 4.6. The obtained values with uncertainties are given by:

$$\begin{aligned} \mathrm{C} &= 10.76 \pm 0.03 \\ \mathrm{r_{fit}} &= (7 \pm 0.43) \cdot 10^{-3}\,\mathrm{m} \\ \theta_{initial} &= [0°; 35°]. \end{aligned} \tag{4.9}$$

The obtained values for the initial radius of the ion beam in equation 4.5 and equation 4.9 are in the same range, but do not agree within the range of uncertainties.
The determination of the parameter ranges with ROOT was performed by only considering the secondary electron rate in the measurement. Since the secondary electrons were not distinguished by their origin, processes apart from scattering processes of ions on residual gas molecules could have been contributed to the measured rate. This is assumed to be one of the reasons causing the difference in the trend of measured and simulated data: while the data points in figure 4.6 seem to indicate an exponential increase of the secondary electron rate over the magnetic field, the black line shows a rather linear increase. One conceivable

[1] `https://root.cern.ch/`
[2] `https://seal.web.cern.ch/seal/snapshot/work-packages/mathlibs/minuit/`

reason for this discrepancy is the movement of the ions in the main spectroemter. Since deuterium ions were terminated in the center of the PS1 magnet, their propagation through the main spectrometer was neglected in the simulations. In contrast, secondary electrons which were experimentally detected originate from scattering processes of ions on residual gas molecules in the main spectrometer. Further studies on this topic could be performed by taking into account the movement on deuterium ions in the main spectrometer. Scattering processes of hydrogen ions on residual gas molecules will be addressed in chapter 5.
Discrepancies of the two values in equation 4.5 and equation 4.9 could further originate from the magnetic mirror effects in the global simulation. In addition, misalignments in the KATRIN beamline which have been neglected could also contribute to the discrepancy as well as the mass composition of ions, that were not known to full extent.

4.3. The pre-spectrometer as ion detector

Besides simulations on measurements that have been carried out, it is of high interest to perform simulations for future measurements in order to suggest configurations for the experimental setup.
Apart from employing the pre-spectrometer as an ion blocking device, its electrode system is considered to provide a method to measure the current of ions directly. Such a method is highly desired since the regular setup of the KATRIN experiment does not offer such a possibility.
As pointed out in chapter 2, a high number of T_3^+-ions is created in the WGTS. As these ions are not guided adiabatically along the magnetic field lines, they could propagate through the beamline and enter the spectrometers. In addition, tritium molecules could also propagate through the beamline and undergo decay processes in the spectrometer section which would lead to the generation of further tritium ions and thus contribute to a higher background rate.
Within the scope of the given thesis, the detection and transmission efficiency of T_3^+-ions was investigated at different voltage settings on the cone electrodes of the pre-spectrometer by performing Kassiopeia simulations respectively. After introducing the simulation settings in subsection 4.3.1, the corresponding studies will be discussed in subsection 4.3.2.

4.3.1. Modification of the pre-spectrometer geometry

Different potential settings with respect to the electrode system of the pre-spectrometer are conceivable. In order to make statements about the detection efficiency from simulation point of view, ions are filtered by the terminators respectively. In addition to terminators that have been implemented and consider ions that hit the beam tubes or the electrode system, a further terminator was added to treat the ions neutralizing on the cone electrodes seperately. As a first step, test simulations targeting the validation of the functionality of this terminator were performed which led to gsl-error messages created by Kassiopeia. Such error messages generally occur in cases where the field calculation can not be carried out with the required accuracy. Through detailed tracking simulations it was found that the gsl-error messages are generated once the ion approaches the electrode.
For this reason, an additional so-called Virtual Surface was implemented on the inner part of the pre-spectrometer in a distance of 2 cm from the electrodes as shown in figure 4.7. All simulations in the following were performed by employing the virtual surface. It is assumed that ions which hit the virtual surface would reach the cone electrode since the distance of 2 mm is negligable compared to the dimemsion of the pre-spectrometer with a diameter of approximately $d_{PS} \approx 1.7\,\mathrm{m}$.
An overview of the simulation settings, including the applied terminators is shown in table 4.3.

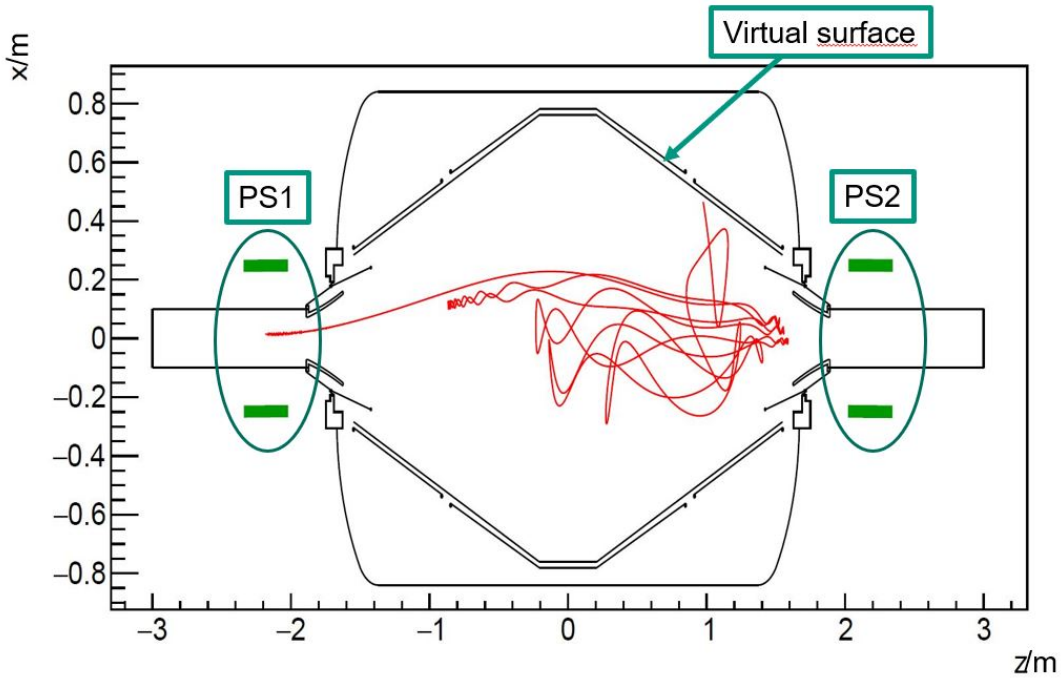

Figure 4.7.: Ion detection with the cone electrodes: A virtual surface was implemented in a distance of about 2 cm to the inner electrodes to enable the detection of tritium ions with the cone electrodes. The terminator was set on the virtual surface. The red curve shows the trajectory of a tritium ion.

4.3.2. Detection and Transmission efficiency of tritium ions

The efficiency with regard to the detection of T_3^+-ions with cone electrodes of the pre-spectrometer has not been investigated yet. Hence, it is desirable to perform simulations at different potential settings and to thus make suggestions for configurations for the upcoming measurements phase which will take place in the beginning of 2018.
The measurement device that will be employed for the measurement of the ion current on the cone electrode only operates if the condition

$$|U_{vessel} - U_{cone}| < 0.4\,V \tag{4.10}$$

is fulfilled, where U_{vessel} corresponds to the potential on the vessel and U_{cone} to the voltage applied on the cone electrode. The measurement device is a picoamperemeter that measures the current caused by electrons originating from neutralization processes of ions that reach the cone electrodes. The trajectories of T_3^+-ions were simulated for three different potential configurations in the pre-spectrometer. Different initial conditions for the ion beam were set for the investigation of the detection and transmission efficiency as shown in table 4.3:

- **Detection efficiency:** In order to investigate the detection efficiency of ions on the cone electrodes, ions were homogeneously distributed over a radius of 3.7 cm. The number of events in the simulation is to 10^4.
- **Transmission efficiency:** In contrast, the initial radius of the ion beam was set to 5 mm for the determination of the transmission efficiency targeting the investigation of the initial radius on the detection efficiency. Here, 10^5 ions were simulated in order to get a sufficient statistics.

Table 4.1 demonstrates that the simulated suppression efficiency of tritium ions in the pre-spectrometer is in the order of 80 %. Hence, it can be concluded that the elevation

Table 4.1.: Detection and transmission efficiencies at different potential settings: The simulation of T_3^+-ion trajectories with regard to the detection on the cone electrode and the transmission through the pre-spectrometer was carried out at different configurations. The voltage settings correspond to the potential on the downstream cone electrode.

Terminator	**-0.5 kV**	**-0.4 kV**	**-0.4 kV**
Downstream cone electrode	0.86	0.82	0.83
Geometry collision	0.14	0.18	0.17
Max. z-position (PS2)	$2 \cdot 10^{-5}$	$<1 \cdot 10^{-4}$	$6 \cdot 10^{-5}$
Min. z-position (PS1)	$1 \cdot 10^{-4}$	$2 \cdot 10^{-4}$	$2 \cdot 10^{-4}$

of the cone electrodes on potential represents a reasonable method for the prevention of ions entering the main spectrometer. However, measurements have to be taken in order to validate the reliability of the simulation.

Table 4.2.: Settings for the simulation of D_3^+-ions at different magnetic fields: The simulation of deuterium-ion trajectories was carried out at different magnetic field settings. Each simulation was performed with 10^6 ions. The applied parameter ranges are listed below.

Paramter	Value/Range
initial radius	$r_{initial} \in [0; 0.037]\,m$
initial polar angle to B	$\theta_{initial} \in [0°; 90°]$
initial energy	$E \in [1; 100]\,eV$
term min z	z=-2.15 m
term max z	z=2.15 m

Table 4.3.: Settings for the simulation of T_3^+-ions: An overview of the settings which were applied for the simulation of T_3^+-ion trajectories is shown.

Setting	**Detection**	**Transmission**
simulated events	10^4	10^5
initial energy (fixed)	10 meV	10 meV
initial polar angle to B	$\theta_{initial} \in [0°, 90°]$	$\theta_{initial} \in [0°, 90°]$
initial radius (fixed)	$r_{initial} \in 0.037\,m$	$r_{initial} \in 0.005\,m$
terminators	term min z	term min z
	term max z	term max z
	term vs	term vs
	term exit death	term exit death
control length	0.001 m	0.001 m
control cyclotron	1/60	1/60

5. Ion scattering simulations in the main spectrometer

Measurements with respect to the ion blocking efficiency which were performed during the First Light Plus measurement campaign were already addressed in the previous chapter 4. The ion current was determined by a direct measurement with Pulcinella and additionally by detecting the corresponding secondary electrons from scattering processes of ions on residual gas molecules on the FPD. The relation of these two rates can be written as

$$R_{ms} = k \cdot R_{mi}, \tag{5.1}$$

where R_{ms} describes the rate of the secondary electrons on the FPD and R_{mi} the ion current directly measured.
This chapter will give a short overview of the direct measurements in section 5.1. Simulations that have been carried out respectively will be highlighted in section 5.2, which will be followed by the comparison of the deuterium ion measurement data with the simulation results.

5.1. Direct measurement of ions with Pulcinella

The measurement device called Pulcinella was installed at the exit side of the main spectrometer in order to enable a direct measurement of the ion current. As pointed out in section 4.1, deuterium ions were created by the source ELIOTT which was mounted on the Rear Wall. The rate of the ions was determined by measuring the corresponding current with the device Pulcinella. The FPD in contrast detected the secondary electrons created by scattering processes of ions on residual gas molecules.
The measurements were carried out with an unbaked main spectrometer at high voltage. The pressure in the main spectrometer during the ion measurements amounted to

$$p_{meas} \approx 2 \cdot 10^{-9}\,\text{mbar}. \tag{5.2}$$

Measuring the ion current with Pulcinella under above conditions led to a value of

$$I_{pul} \approx 10\,\text{pA}. \tag{5.3}$$

However, it must be mentioned that the systematic uncertainty of this measurement device is not known in detail. Considering the measured rate of secondary electrons on the FPD, applying equation 5.1 yields

$$k_{meas} = (4.75 \pm 0.17) \cdot 10^{-6}\,\frac{e^-}{\text{ion}}. \tag{5.4}$$

for a pressure of $p = 1 \cdot 10^{-10}\,\text{mbar}$[1]. The majority of residual gas molecules in the main spectrometer in an unbaked condition are water molecules (H_2O). Hence, it can be assumed that secondary electrons mainly originate from ionization processes of deuterium ions on H_2O-molecules.

[1] pressure expected in the KATRIN operating mode.

5.2. Comparison of measured secondary electron rate to simulation result

In oder to compare the measurement data obtained during First Light Plus with simulation results, the factor k in equation 5.1 has to be determined for the simulation result. To do so, scattering processes of deuterium ions on H_2O-molecules were performed which in turn required the implementation of the corresponding cross section in Kassiopeia as will be discussed in the following.

5.2.1. Implementation of the ionization cross section in Kassiopeia

Scattering processes of ions on residual gas molecules had been implemented for hydrogen (H_2) as target molecule. In order to allow scattering processes of H^+-ions on H_2O-molecules, the corresponding cross section was implemented in Kassiopeia as part of this thesis.
To do so, the differential cross section $\frac{d\sigma}{dE}$ as well as the total cross section σ which was obtained by a numerical integration of the differential cross section were considered. According to the suggestion of Rudd et al, the singly differential cross section $\frac{d\sigma}{dE}$ written as

$$\frac{d\sigma}{dE} = \sum_{all,i} G_j \frac{d\sigma^j}{dW_j} \tag{5.5}$$

where $W_j = E - I_j$ describes the kinetic energy of the secondary electron, I_j the ionisation energy of sub-shell j and G_j the partitioning factor which adjusts the contribution of different subshells. The secondary electron energy distribution for single ionisation of sub-shell j is given by the following equation

$$\frac{d\sigma^j}{dw} = \frac{S}{B_j} \cdot \frac{F_1(\nu) + wF_2(\nu)}{(1+w)^3 \cdot [1 + \exp \alpha(w - w_c)/\nu]}. \tag{5.6}$$

Here, w denotes the scaled secondary electron energy, B_j the binding energy of sub-shell j and ν^2 the scaled speed squared of a particle($\nu^2 = T/B_j$). The two functions F_1 and F_2 consist of different low and high energy parts, which are represented in more detail in D. The total cross section was also implemented according to the Rudd model based on following relationships between high energy part σ_{high} and low energy part σ_{low}:

$$\begin{aligned} \sigma(\tau) &= \left(\frac{1}{\sigma_{low}} + \frac{1}{\sigma_{high}} \right)^{-1} \\ \sigma_{low}(\tau) &= 4\pi a_0^2 \left[C \cdot \left(\frac{T}{Ry} \right)^D + F \right] \\ \sigma_{high}(\tau) &= 4\pi a_0^2 \left(\frac{Ry}{T} \right) \left[A \cdot \ln \left(1 + \frac{Ry}{T} \right) + B \right]. \end{aligned} \tag{5.7}$$

The values for the dimensionless coefficients A,B,C,D and F can be found in appendix D. Due to a lack of literature, the angular distribution of secondary electrons is assumed to be isotropic as a first approach. The illustration of the total cross section and the secondary electron energy distribution are shown in figure 5.1.

5.2.2. Determination of the ionization efficiency

In order to determine k_{sim} which refers to the factor in equation 5.1 from simulation point of view, simulations of deuterium ions starting in the PS2 magnet were performed. To avoid long computation times, the pressure in the main spectrometer was set to $3 \cdot 10^{-6}$ mbar. As the pressure in the simulation is 500 times higher than in the corresponding measurements, the probability for the occurence of the ionization process is increased by the same factor in the simulation.

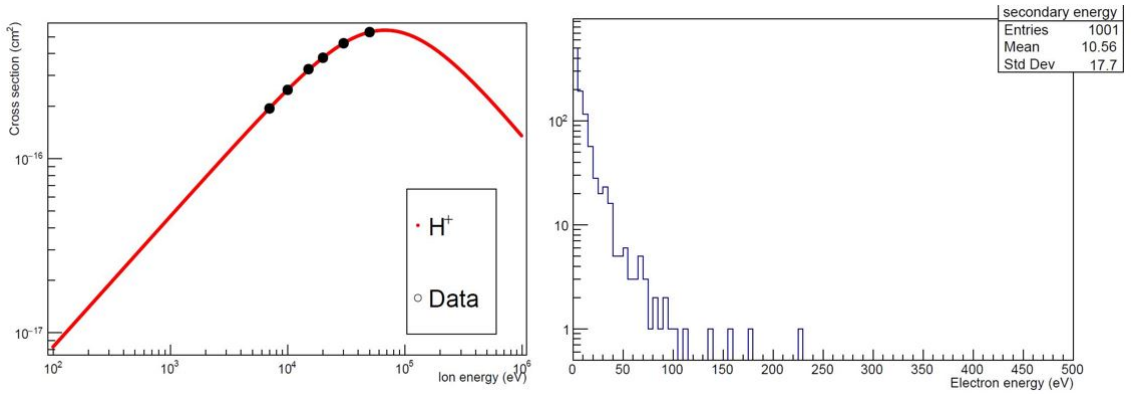

Figure 5.1.: Total cross section and energy distribution of secondary electrons: Left: The total cross section is depicted over the energy of the proton. **Right:** The energy distribution of electrons originating from scattering processes of protons on water molecules is shown.

Since the number of hydrogen atoms in the main spectrometer can be neglected compared to the amount of water molecules, only the ionization process of protons on water molecules was enabled for the simulations. The distribution of the initial radius of the ions were set according to the results obtained as the final radial distribution in simulations of deuterium ions in the pre-spectrometer. The magnetic field settings as well as the settings on the electrodes are shown in table 5.3.
The calculation of the ionization efficiency k_{sim} requires the simulation of the created secondary electrons from their point of generation to the FPD. To do so, the simulation was carried out in two stages: in the first stage, protons were started in the center of the PS2 magnet with an energy of 30 eV. The employment of the terminator term secondaries ensures that the tracking of the ion is stopped once an ionization process takes place. In the second stage of the simulation, the positions and energies of the secondary electrons created in the scattering process were read in with the generator ks generator simulation. The electrons were tracked by applying the terminators presented in table 5.2. The terminator term secondaries ensures that the calculation of the track is stopped once a secondary electron is created. The position of the secondary electron as well as its energy is stored in the corresponding ROOT file.
The generator ks generation simulation allows to consider the positions from a ROOT file and to start a further simulation. Since electrons which are stored in the main spectrometer would lead to a large computation time, a further terminator term trapped was employed in the secondary electron simulation ensuring that the tracking process is stopped once the electron undergoes five reflections.
Applying the terminators shown in table 5.1, the number of secondary electrons which were terminated due to term max z was determined to

$$N_{e^-,sec} = 160. \tag{5.8}$$

Figure 5.2 shows the distribution of the electrons over the terminators..
As explained in chapter 2 electrons that respect the condition

$$\theta_{max} = \arcsin\left(\sqrt{\frac{B_S}{B_{max}}}\right) \tag{5.9}$$

are trapped in a so-called magnetic bottle. According to , such electrons will leave the magnetic bottle at some point and therefore reach the detector. Since the terminator term trapped in the simulation stops the tracking of the secondary electron once its number

of turns equals to 5, it is assumed that a certain fraction of the trapped electrons in the simulation reach the focal plane detector. By considering the different magnetic fields generated by the PS2 magnet and the pinch magnet at shown in table 5.3, the rate of electrons that will leave the magnetic bottle at the downstream and the upstream side of the spectrometer can be distinguished: by assuming the surface of the sphere which represents the isotropic distribution of the secondary electron emission, the areas corresponding to the magnetic field strength can be calculated each for the downstream and the upstream side of the spectrometer. The contribution of each area to the total area represents a measure of secondary electrons that will leave the magnetic bottle at some point:

$$\begin{aligned} \Phi_{\text{trapped,DS}} &= 0.44 \\ \Phi_{\text{trapped,US}} &= 0.56. \end{aligned} \tag{5.10}$$

Since 56 % of the ions which are trapped in the simulation can be added to the amount of ions which reach the focal plane detector, the ionization efficiency calculated from simulated data amounts to

$$\mathrm{k_{sim}} = (7.66 \pm 0.18) \cdot 10^{-2} \, \frac{\mathrm{e^-}}{\mathrm{ion}}. \tag{5.11}$$

In order to compare this value with the corresponding value obtained through measurement data in equation 5.4, the difference in the pressure has to be considered. Since the simulation was performed at a pressure of

$$\mathrm{p_{sim}} = 3 \cdot 10^{-6} \, \mathrm{mbar}, \tag{5.12}$$

the ionization efficiency from the simulation has to be multiplied with a factor of $\frac{1}{3} \cdot 10^{-4}$ which leads to

$$\mathrm{k_{sim}} = (2.55 \pm 0.06) \cdot 10^{-6} \, \frac{\mathrm{e^-}}{\mathrm{ion}}. \tag{5.13}$$

By considering the values obtained in equation 5.4 and equation 5.13 it can be concluded that the measured and simulated data differ from each other by a factor of 1.86. Conceivable reasons for this discrepancy are given by the following:

- **Unknown configuration of the electrode system:** The simulation was performed at symmetric potential settings on the electrodes. However, the detailed settings during the measurements are not known. In case of the symmetric potential setting, the rate of secondary electrons exiting the main spectrometer on the upstream side is the high since in other conceivable asymmetric settings the potential on the upstream cone electrodes is higher.
  Hence, the obtained value for the secondary electrons which reach the FPD can be interpreted as a minimum rate.
- **Not all ions reach Pulcinella:** As mentioned before, Pulcinella is installed at the downstream side of the main-spectrometer. Ions could have hit the inner wall of the main spectrometer and neutralized immediately instead of propagating to the ion measurement device.
- **Unknown systematic uncertainties:** Systematic uncertainties of the measurement devices including the pressure measurement device and Pulcinella are unknown.
- **Composition of ions in the main-spectrometer:** No information on the species of ions which entered the main-spectrometer in the measurement is available. The implementation of further cross sections would be required for other ion species than proton (deuterium) scattering on water molecules.
- **Neglected processes:** Finally, other processes that have not been considered yet could contribute to the creation of electrons that reach the FPD and cause a higher secondary electron rate.

Table 5.1.: Applied terminators for the simulation of secondary electron trajectories: This table shows the settings of the terminators applied in the simulation of the secondary electron trajectories in the main spectrometer.

Terminator	**Condition**
Term min z	$z = -12.2\,\mathrm{m}$
Term trapped	turns = 5
Term max z	$z = 12.2\,\mathrm{m}$
Term death	Collision with beam tubes, vessel, electrodes
Term max r	$r = 4.5\,\mathrm{m}$

Table 5.2.: Secondary electrons categorized in terminators: The termination of the secondary electrons categorized by the conditions.

Terminator	**Number of secondary electrons**
Term min z	1154 ± 34
Term trapped	1082 ± 33
Term max z	160 ± 13
Term death	134 ± 12
Term max r	48 ± 7
Gsl error	44 ± 7

Table 5.3.: Settings for the scattering simulation: The initial energy of the ions starting in the PS2 magnet, the magnetic field settings as well as the configuration of the electrode system is shown.

Setting	**Value/Range**
initial energy (H^+)	30 eV
PS1 magnet	1.8 T (40 %)
PS2 magnet	1.8 T (40 %)
Pinch magnet	1.2 T (20 %)
Upstream cone el.	-0.1 kV
Wire Electrondes	-0.1 kV
Downstream cone el.	-0.1 kV

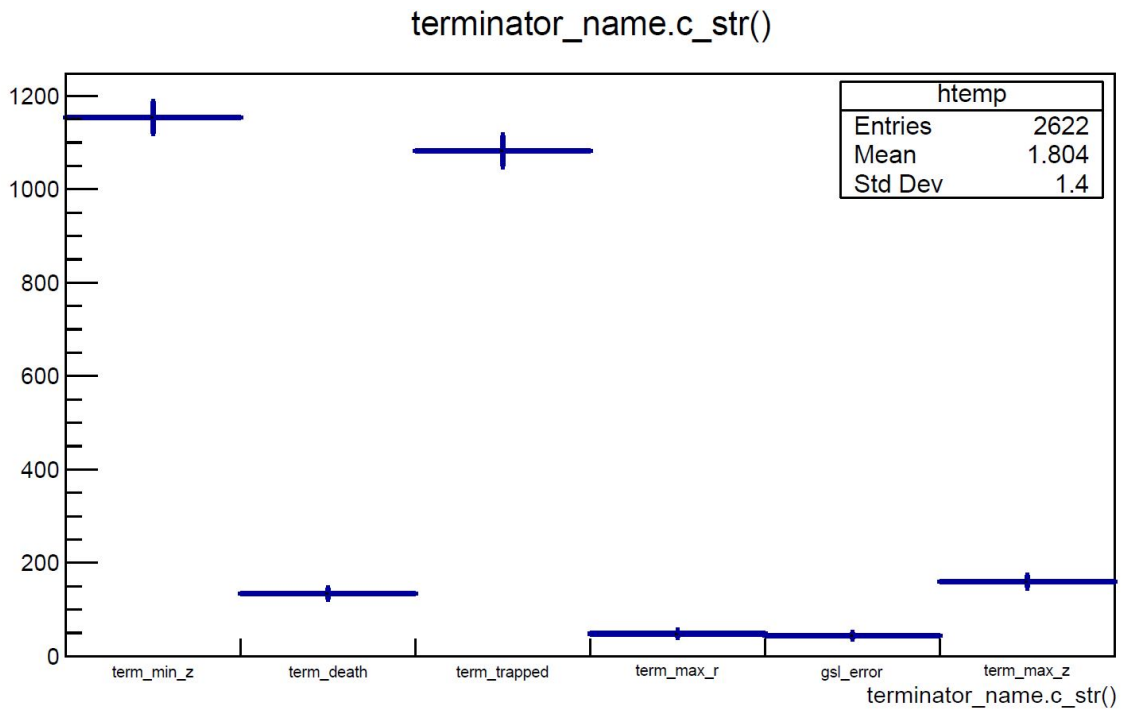

Figure 5.2.: Illustration of the secondary electron distribution over the terminators: The secondary electrons are categorized by their terminators. The error bars represent the error based on a Poisson distribution of the electrons.

6. Measurements with the UV light source LightHammer

Besides ion background sources, ionization processes of Rydberg atoms also contribute to a higher background level in the main spectrometer, as mentioned in 2.3. In order to reduce this type of background source by cleaning the inner wall of the main-spectrometer, a high intensity Ultra-Violet irradiator, the so-called Light Hammer, was installed at the main spectrometer.
This chapter provides an overview of the performed measurements and the results. The outline of the measurement goals and descriptions will be followed by the discussion of the results focusing on the background rates before and after the Light Hammer operation.

6.1. Measurement goals

As mentioned in chapter 2, the sensitivity of the KATRIN experiment is limited by an elevated background rate. The contamination of the main spectrometer with a ^{228}Th source led to the conclusion that decay processes of ^{210}Pb- atoms mainly contribute to the background rate. The detailed process leading to the creation of secondary electrons could not be verified. However, Rydberg atoms which enter the sensitive volume of the main spectrometer due to their electric neutrality, thus being ionized by the black body radiation of the spectrometer by emitting secondary electrons are assumed to be one of the main background causing candidates. Measurements with the Light Hammer were carried out in order to test the removement of H_2O- and H_2-molecules from the inner surface of the spectrometer which represent the target mass for the creation of Rydberg states. Previous measurements after bake-out phases of the spectrometer indicated the dominance of hydrogen molecules on the inner surface of the vessel accompanied by iron, nickel and chromium atoms.

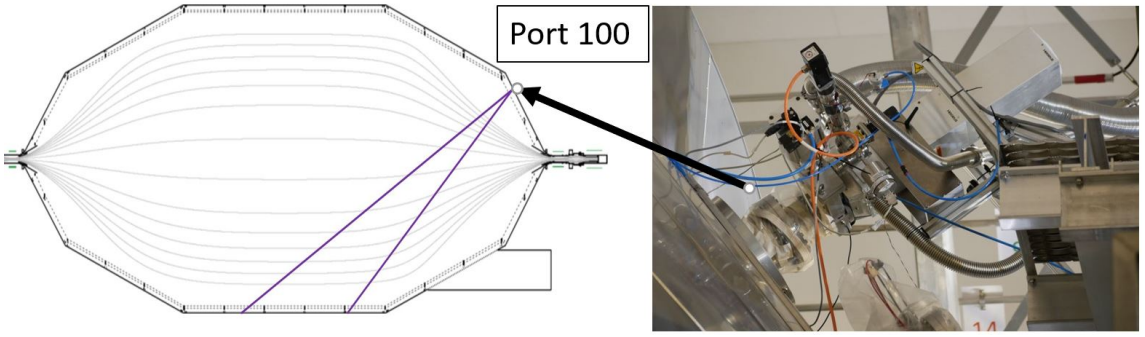

Figure 6.1.: The Light Hammer at port 100: The Light Hammer was installed at port 100 of the main spectrometer.

6.2. Commisioning of the Light Hammer

The Light Hammer MK6 is a microwave-powered UV irradiator manufactured by Heraeus Noblelight [1]. It emits high intensity UV light and consists of an independent irradiator unit with a corresponding power supply. One feature of the Light Hammer is given by its electrodeless bulb with a relatively long live time of approximately 8000 hours. Since the system is powered by high frequency microwaves, a radiofrequency (RF) detection device is employed. If dangerous levels of radiofrequency occur outside of the irradiator, the system is automatically shut down immediately. In addition, the Light Hammer is surrounded by a UV shielding and connected to a blower system for cooling. The power of the UV light source can be varied between 35 % and 100 %. Detailed information can be found in appendix D. In order to irradiate the inner wall of the stainless steel-vessel of the main spectrometer, the Light Hammer was installed at port 100. A 63CF sapphire window mounted on the corresponding gate valve shows a risk of a leak due to thermal stress. For this reason, two temperature sensors were employed: one sensor was attached directly on the sapphire window while the second sensor was installed on the flange. In addition, the sapphire window was cooled by a compressed air line. While increasing the power of the Light Hammer from 50 % to 100 % level in 10 % steps with a closed gate valve, the temperature on the sapphire window increased up to 150°C. In order to prevent the windows from breaking and thus enabling the inlet of air into the main spectrometer, the unbaked spectrometer was irradiated with a power of 60 % corresponding to a temperature of 90° C on the sapphire window flange. The investigation of the influence of the UV radiation on the pressure inside the main spectrometer, was performed by opening the gate valve at port 100 and turning on the Light Hammer at 60 % power level.
After an irradiation time of about 14 h, the pressure in the main spectrometer decreased from $1 \cdot 10^{-7}$ mbar to $2.1 \cdot 10^{-8}$ mbar. Figure 6.2 demonstrates that CO_2-molecules dominate the total pressure inside the main spectrometer. However, it can be seen that corresponding curve decreases over the whole measurement time. In contrast, the partial pressure of H_2O-molecules shows a slight increase within the first four hours of the irradiation. As can be seen at the black curve the partial pressure of H_2-molecues remains constant at approximately $3 \cdot 10^{-11}$ mbar over the whole measurement time.

6.3. Background measurements before and after Light Hammer operation

Measurements of the background in the main spectrometer were performed before and after the operation of the Light Hammer in order to investigate the influence of the high intensity irradiation.
The background level was determined by observing the electron rate and the corresponding pixel distribution at the focal plane detector.
The measurement data was analyzed by applying the software BEANS [44].

6.3.1. Reference background measurement before Light Hammer operation

Before irradiating the inner walls of the main spectrometer, the main spectrometer was baked. In order to investigate the impact of the Light Hammer irradiation, a reference background measurement was taken at nominal magnetic field (70 % of the maximum field) (3.15 T) at the PS2-magnet, the pinch- and the detector magnet. The inner electrodes of the pre-spectrometer were grounded while the vessel of the main spectrometer was elevated to 18.5 kV. The valve between the pre-spectrometer and the CPS was closed, in contrast to

[1] https://www.heraeus.com/de/hng/products_and_solutions/uv_lamps_and_systems/microwave_powered_uv_lamp_systems.aspx

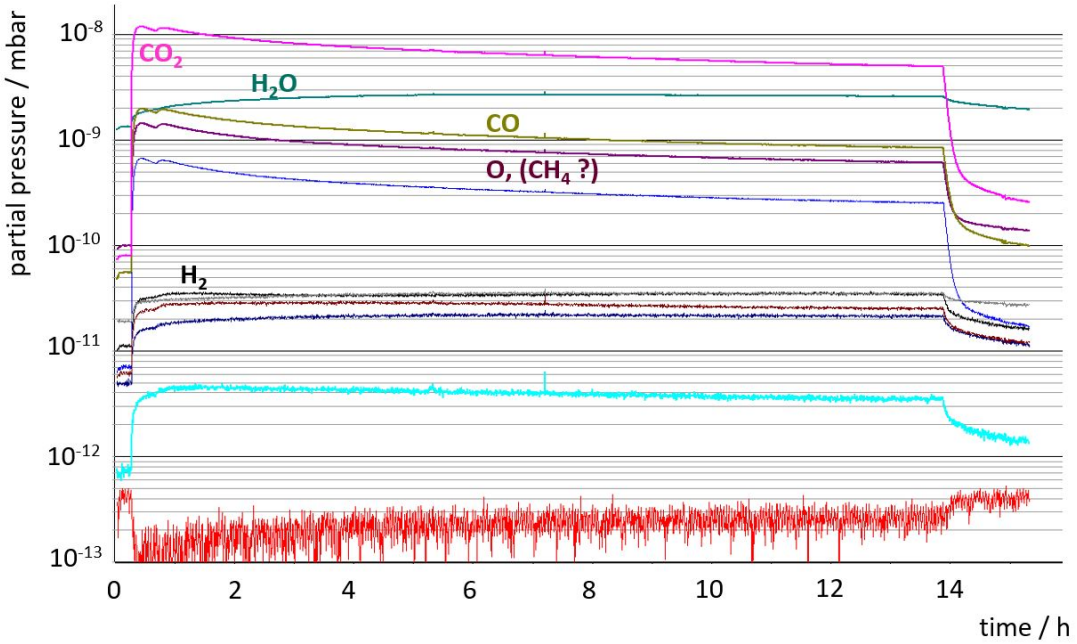

Figure 6.2.: Results of the residual gas analyzer during the commissioning measurements: The partial pressure curves shown over the measurement time. It can be seen that CO_2-molecules dominate the total pressure inside the spectrometer.

the valve between the pre- and the main-spectrometer and the FPD gate valve, which both were opened during the measurement.
The background rate was estimated seperately for electrons in the volume and electrons emerging from the inner wall of the main spectrometer. With respect to the radial arrangement of the pixels on the FPD, this equals to dedicated pixel selections depending on the desired origin of the background electrons.

Background rate from the main spectrometer volume

The pixel distribution and the secondary electron rate over their interarrival time[2] are shown in figure 6.3. The linear behaviour of the background electron rate on a logarithmic scale over this quantity originates from Poisson-distributed decays in the main-spectrometer. Since radioactive decays are assumed, it is in accordance with theoretical expectations.
The rate of background electrons created in the volume of the main spectrometer amounts to

$$\mathrm{R}_{\mathrm{volume,before}} = (495 \pm 3)\mathrm{mcps} \tag{6.1}$$

and is constant over time within the scope of uncertainties.

Background rate of the main spectrometer vessel

Pixels which were excluded from the analysis of the volume are assumed to originate from secondary electrons generated on the vessel and therefore were investigated seperately. Here, the rate of the secondary electrons increases rapidly over the interarrival time. This effect originates from so-called cluster events which take place on the inner wall of the vessel. Cluster events are characterized by secondary electrons created within a short, clearly defined time period initiated by one singular cause at the wall. Since this effect emerges mainly on the vessel surface, it is reasonable to analyze the rate of electrons seperately. As in the case of the background electrons created in the volume, the rate of the signals apparently is constant over time. The corresponding rate is given by (15.40 ± 0.01)cps.

[2]The interarrival time describes the time period between two detected FPD events.

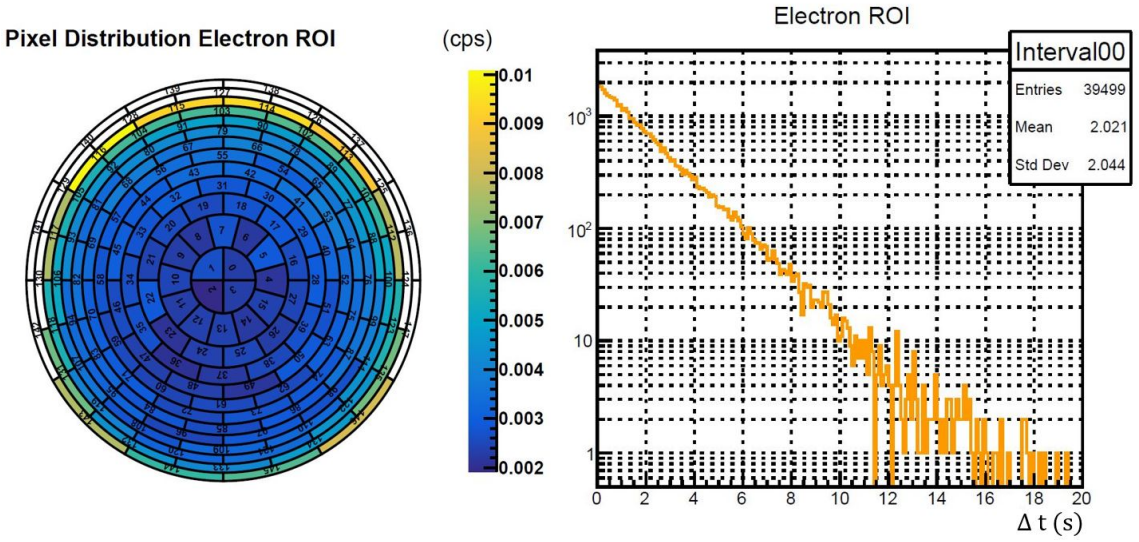

Figure 6.3.: Secondary electron rate from the volume before Light Hammer operation: Left: The pixel distribution of the focal plane detector is shown. Outer pixel have been excluded for the analysis of the volume background rate. **Right:** The logarithm of the secondary electron distribution is depicted over their interarrival time.

6.3.2. Operation of the Light Hammer

By opening the gate valve at pump port 100, UV irradiation of the inner wall of the spectrometer was started. The Light Hammer was turned on, at first step applying a power of 50%. The power was increased to 60% after running the measurement for approximately $t \approx 30\,\text{min}$. Besides the monitoring of the pressure, a residual gas analyzer was installed behind a cooled baffle to analyze the composition of the residual gas inside the main spectrometer volume. Figure 6.4 show the pressure distribution and the curves for different gas species. As expected, the pressure increases at all vacuum gauges and is dominant at pump port 1. The residual gas analyzer indicates an increase of the curve corresponding to molecules possessing a mass of 28 u and carbondioxide (CO_2) molecules, where the latter one shows a smaller increase. Since the amount of CO_2-molecules becomes higher, it is assumed that carbonmonooxide (CO) molecules mainly contributes to the increase of the darkgreen curve. In case of a leak, an increase due to nitrogen (N_2) molecules is conceivable.
It can be seen that the hydrogen curve shows a spike in the beginning. This observation can be explained by a short close and opening process of the gate valve. Due to the assumption of a leak, the gate valve was closed and opened again after a time period of approximately 10 minutes. A rapid increase of the curves corresponding to the elements contained in the air when opening the gate valve would have demonstrated the existence of such a leak: molecules stored in the volume between the gate valve and the sapphire window would have entered the spectrometer. The absence of such an observation led to the conclusion that no leak did exist. Due to heating and cooling effects of the baffles, a pressure increase can be seen in the corresponding curve for the next day. After 2-3 days of operation, the Light Hammer and the compressed air line were turned off.

6.3.3. Background measurement after Light Hammer operation

Soon after closing the gate valve and turning off the UV irradiator, a further background measurement was started. Targeting the estimation of the influence on the background, the measurement conditions were set equal to the reference measurement. Again, the analysis was performed seperately for the volume and the region near the inner wall of the main

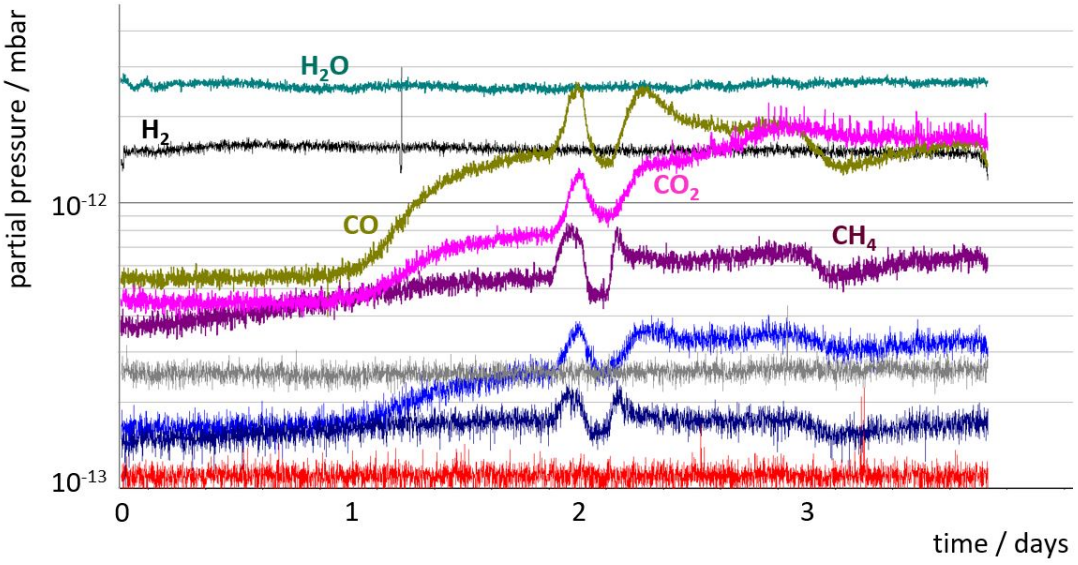

Figure 6.4.: Results of the residual gas analyzer: The partial pressure curves shown over the measurement time. Each color corresponds to a molecule species.

spectrometer.
The electron rate in the volume of the spectrometer after the irradiation is given by

$$\mathrm{R}_{\mathrm{volume_{after}}} = (0.497 \pm 0.002)\mathrm{cps} \tag{6.2}$$

and therefore equals to the backround rate before the Light Hammer operation within the scope of uncertainties, it can be concluded that the irradiation had no influence on the background level in the volume of the main spectrometer.
However, the number of background electrons generated in the region of the inner wall of the spectrometer shows an increase by a factor greater than 3:

$$\mathrm{R}_{\mathrm{wall_{after}}} \approx 50\,\mathrm{cps} \tag{6.3}$$

at the beginning. As shown in figure 6.5, the secondary electron rate decreases immediately. An exponential fit of the curve was performed with BEANS by means of the function

$$\mathrm{r(t)} = \mathrm{a} \cdot \exp\left(\frac{-\mathrm{t}}{\mathrm{b}}\right) + \mathrm{c} \tag{6.4}$$

where t describes the measurement time while b and c are dimensionless constants.
In addition, it is striking that the rate of the electrons decreases on a time-scale of hours after irradiation, as can be seen in figure 6.5. This phenomen does not agree with expectations. In order to further investigate these observations, the dependency of the electron rate originating from the inner surface of the main spectrometer on the pressure was studied. The corresponding curve depicted in figure 6.7 decreases and shows a similar dependency on the time as the secondary electron rate. Here, the events on the FPD which hit the pixels in the outer rings were in turn categorized in single and cluster events. As figure 6.7 shows, a correlation between single events and the pressure does seems to exist while cluster events do not show a significant explainable dependency. However, the pressure in the main spectrometer does not correlate with the background rate generated in the volume of the spectrometer.
To sum up, it can be concluded that the Light Hammer had no impact on the background rate on the volume of the main spectrometer, while the number of secondary electrons detected at the outer pixels of the FPD shows a significant increase after the irradiation process.

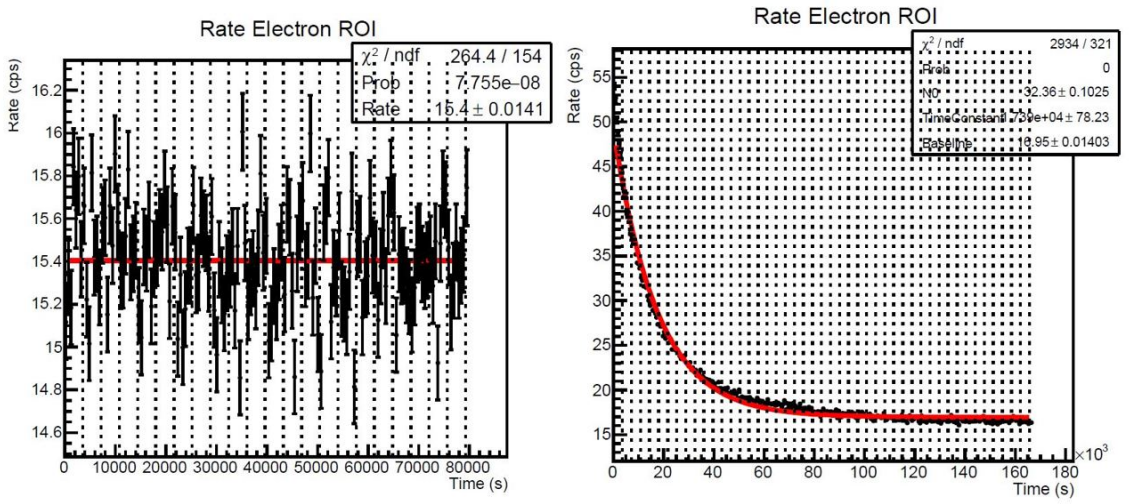

Figure 6.5.: Secondary electron rate on the outer pixels before and after Light Hammer operation: Left: The secondary electron rate before Light Hammer operation is shown for electrons emerging from the wall of the main spectrometer. As can be seen, the rate is constant over time. **Right:** The secondary electron rate after Light Hammer operation over the measurement time. It is striking that the rate behaves differently from before.

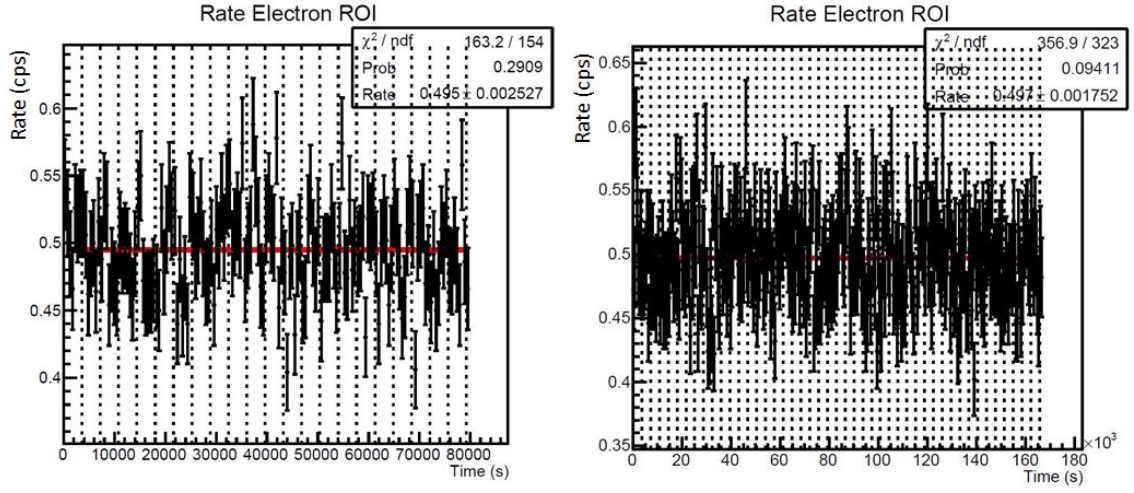

Figure 6.6.: Secondary electron rate from the volume of the spectrometer before and after Light Hammer operation: Left: Shown is the secondary electron rate over the time before the Light Hammer operation. The rate is constant. **Right:** The background rate after the irradiation process is illustrated.

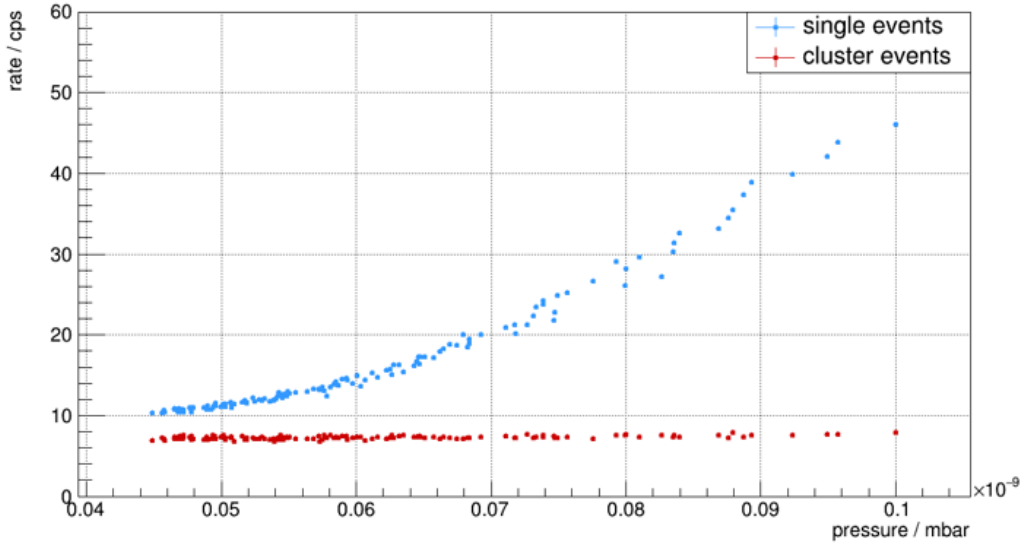

Figure 6.7.: Single and cluster events originating from the region of the spectrometer wall: The blue data points are single events, while the red points represent the cluster events. It can be seen that a correlation exists between the rate of single events and the pressure, while the cluster rate is not affected and therefore is constant.

6.4. Discussion of the results

The irradiaton of the inner surface of the main spectrometer did not lead to a change of the secondary electron rate of the volume. Analyzing secondary electrons originating from the surface distinguishing the events in single and cluster events by means of the inter arrival time of the electrons with

$$\Delta t < 0.1\,\mathrm{s} \tag{6.5}$$

show that the cluster events do not correlate with the pressure while single events do. Conceivable reasons for the occurence of this effect are given by the following:

1. The number of single events decreases due to the pressure.
2. The number of single events causes the drop of the pressure.
3. The correlation between the behaviour of the single events and the pressure show no causality.

One conceivable causality is the work function of the stainless steel surface of the inner wall of the main spectrometer. The high intensity UV light causes effects on the surface with regard to the work function . The surface properties of the vessel on the inner side have not been investigated and the exact work functions are not known. The impact on the work function of the Light Hammer could lead to a time-dependent variation of it and thus a change in the rate of single events over time.
Properties of the surface condition could further be investigated by precise measurements with respect to the time-dependent behaviour of secondary electrons emitted from the inner wall.

7. Conclusion

The KATRIN experiment aims for the direct measurement of the neutrino mass by a precise investigation of the energy spectrum of electrons originating from β-decay processes of molecular tritium close to the endpoint. In order to reach the required mass sensitivity of $0.2\,\mathrm{eV/c^2}$ with a confidence level of 90 %, the background rate during the neutrino mass measurement must not exceed 0.01 cps. The reduction of background sources as far as possible is required in order to achieve such a low background level. Therefore, a good understanding of background processes and their origin is crucial.

One focus of this thesis was the investigation of ion induced background processes in the spectrometer section. Employing the software Kassiopeia, ion trajectories were simulated targeting a comparison of simulated and measured data obtained through the ion measurements which were carried out during the First Light Plus measurement campaign. As a first step, appropriate simulation settings and their influence with regard to the accuracy of the simulation were verified. The impact of the step size control options were studied in detail with regard to the energy conservation which represents a measure for the accuracy. After identifying the appropriate settings by finding a compromise between the computation time and the accuracy, simulation of deuterium ion trajectories were carried out in the pre-spectrometer at different magnetic field settings. Thereby, parameter ranges which could not be experimentally determined during the First Light Plus measurement campaign were estimated by means of two approximation methods. The comparison of measured to simulated data with respect to the variation of the magnetic field shows a discrepancy: while the measured data can be described by an exponential increase, the simulation results show a saturation of the rate at higher magnetic fields. However, it has to be stated that the measurement data correspond to the secondary electrons caused by scattering processes of D_3^+-ions on residual gas molecules in the main spectrometer and are detected by the focal plane detector. In contrast, the simulation result refers to the number of ions that reached the z-position of the PS2 magnet. Therefore, the propagation of the ions in the main spectometer has been neglected in this comparison.
In order to study the correlation between the ion-induced secondary electron rate at the focal plane detector and the rate of ions entering the main spectrometer, the simulation software has been extended within the frame of this thesis to include additional scattering processes. The ionization cross section of protons on water molecules was implemented according to [62],[63]. Considering the energy range of ions occuring in the KATRIN experiment, the total cross section and the differential cross section describing the secondary electron energy were taken into account. Due to a lack of literature, the angular distribution of such electrons is assumed to be isotropic. Scattering simulations of protons on water molecules in the volume of the KATRIN main spectrometer were performed with the implemented cross sections. Thereby, the rate of secondary electrons which reach the focal plane detector and thus the ionization efficiency which is the fraction of the secondary electron rate to the ion rate were determined as a first approach to $k_{sim} = (2.55 \pm 0.06) \cdot 10^{-6}$ counts per ion at a pressure of $p = 1 \cdot 10^{-10}$ mbar.

Taking into account the measured ion rate by Pulcinella in the First Light Plus measurements, the ionization efficiency based on measurement data was calculated to a value of $k_{exp} = (4.75 \pm 0.17) \cdot 10^{-6}$ counts per ion. The comparison of the results from the simulation and the measurement led to the conclusion that the measured secondary electron rate per ion exceeds the simulated rate by a factor of 1.86. This discrepancy is assumed to be caused by various factors. First, the detected ion rate could have been reduced due to neutralization processes of ions on the inner wall of the spectrometer that in turn did not reach the ion measurement device. A second reason is based on the impact of the ion mass on its propagation in the main spectrometer. In contrast to simulations of D_3^+-ion trajectories in the pre-spectrometer, the scattering simulations in the main spectrometer were performed with H^+- ions. Further reasons include unknown systematic uncertainties of measurement devices (for example Pulcinella and vacuum gauges), the angular distribution of secondary electrons assumed to be isotropic and electrode settings that were not known in detail.

An important part of this thesis was the simulation of T_3^+-ion trajectories with regard to the tritium ion suppression efficiency of the KATRIN pre-spectrometer for different electro-magnetic configurations. Targeting the investigation of the transmitted tritium ion rate, simulations were performed at high voltage (-18.3 kV) and at grounded potential of the pre-spectrometer vessel. In each case, the downstream cone electrode was biased on potential U_{dc} according to $U_{vessel} - U_{dc} = -400V$. Considering 10^4 tritium ions starting in the center of the PS1 magnet distributed over a radius of 5 mm, the suppression efficiency was determined to 82 %.
Furthermore the possibility to directly measure the T_3^+- ion current with the downstream cone electrode was investigated via simulations. Tritium ions were started in the center of the PS1 magnet at z=-2.15 m[1]. In contrast to the previous case, 10^4 T_3^+-ions were distributed over a radius of 3.7 cm. The detection efficiency amounted to 83 %.
In both simulations, the initial energy of the tritium ions was set to 10 meV.

A further goal of this thesis was to study the impact of UV irradiation on the inner surface of the main spectrometer with respect to the background rate. Previous measurement indicated that the decay of ^{210}Pb-atoms is accompanied by the creation of Rydberg atoms which enter the sensitive volume of the spectrometer and create low-energy secondary electrons. In contrast to charged particles, Rydberg atoms are not shielded magnetically due to their electrical neutrality which enables them to propagate into the volume. The observation of selective field ionization processes supports the hypothesis of Rydberg atoms being responsible for the observed background.
In order to remove atoms which initiate the generation of such Rydberg atoms in the main spectrometer, the UV irradiation source Light Hammer was installed at pump port 100. The inner surface of the spectrometer was irradiated for approximately 90 hours continuously while a residual gas analyzer operated simultaneously during the whole measurement. The electron rate on the focal plane detector was measured and analyzed seperately for the volume and the spectrometer surface by investigating different pixel selection cuts. It was shown that the UV irradiation did not affect the volume background rate which amounted to (495.0 ± 2.5) mcps before and (497.0 ± 1.8) mcps after the Light Hammer operation. However, the secondary electrons originating from the wall had increased by a factor of >3 after the irradiation. In addition, it was observed that the secondary electron rate decreased on a time scale of hours after the end of the irradiation. A further distinction of such secondary electrons in single and cluster events led to the conclusion that a correlation between the pressure in the main spectrometer and rate of single events exists, while

[1]The center of the pre-spectrometer corresponds to z=0 m.

the rate of cluster events is not affected. The causality for the correlation could not be identified. Hence, further measurements focusing the behaviour of electrons in more detail are suggested to gain a better understanding of the impact of the UV irradiation on the background processes originating from the wall of the spectrometer.

Appendix

A. The TRIMS Experiment

Apart from background processes in the main spectrometer, excitations of the daughter molecules originating from β-decay process of molecular tritium affect the sensitivity of the neutrino mass measurement in KATRIN. For this reason, a good understanding and an accurate characterization of the molecular tritium source is required.
The Tritium Recoil-Ion Mass Spectrometer (TRIMS)-experiment, currently under construction at the University of Washington in Seattle, targets the measurement of the molecular-tritium β-decay branching ratio to bound molecular ion $^3HeT^+$. A schematic overview of the experimental setup is shown in figure A.1.

The experiment is based on the time-of-flight measurement principle. Applying a mass spectrometer and a silicon detector at each end, where one is responsible for the detection of β-electrons and one for the ion detection, electrons and ions are measured in coincidence. The spectrometer is filled with molecular tritium gas at a pressure of approximately 10^{-5} mbar. In order to accelerate the ions and β-electrons, a potential difference of 60 kV is applied between the two detectors. Magnetic fields in the axial direction ensure the guidance of particles to the detectors.
The ion energy and its time of flight can be calculated by

$$E_{ion} \propto \frac{q \cdot V_{chamber} \cdot \Delta D_{ion}}{L_{chamber}} \tag{A.1}$$

$$t_{ion} \propto \sqrt{\frac{2m \cdot L_{chamber} \cdot \Delta D_{ion}}{q \cdot V_{chamber}}} \tag{A.2}$$

where ΔD_{ion} describes the distance between the ion and the detector, $L_{chamber}$ the length of the chamber, $V_{chamber}$ the voltage drop and q the charge number of the ion. The derivation of equation A.2 and equation A.1 were performed neglecting the initial energy of the ion which amounts to a few eV. The difference in the time of flight between dissociated mass-3 ions $^3He^+, T^+$ and bound mass-6 ions $^3HeT^+$ is given by a factor $\sqrt{2}$.
The combination of the quantities calculated in above equations allows us to distinguish between mass states and therefore is applied to determine the branching ratio to the bound molecular ion in TRIMS.
However, it is of high interest to detect the β-electrons in coincidence since the branching ratio as a function of the energy of β-electrons allows a more detailed comparison with theoretical calculations. In addition, the detection β-electrons is required for the determination of t_{ion} since the time of the ion detection is measured relative to the β-detection time.
A previously performed experiment led by Wexler in 1958 of branching ratios yielded results that show large discrepancies to theoretical expectations [46]. By detecting the ion in coincidence with the β-electron, the variation of the dissociation fraction can be investigated with regard to the electron energy. Such a measurement would allow to check the dependence of the observable on beta energy, testing a possible explanation for this

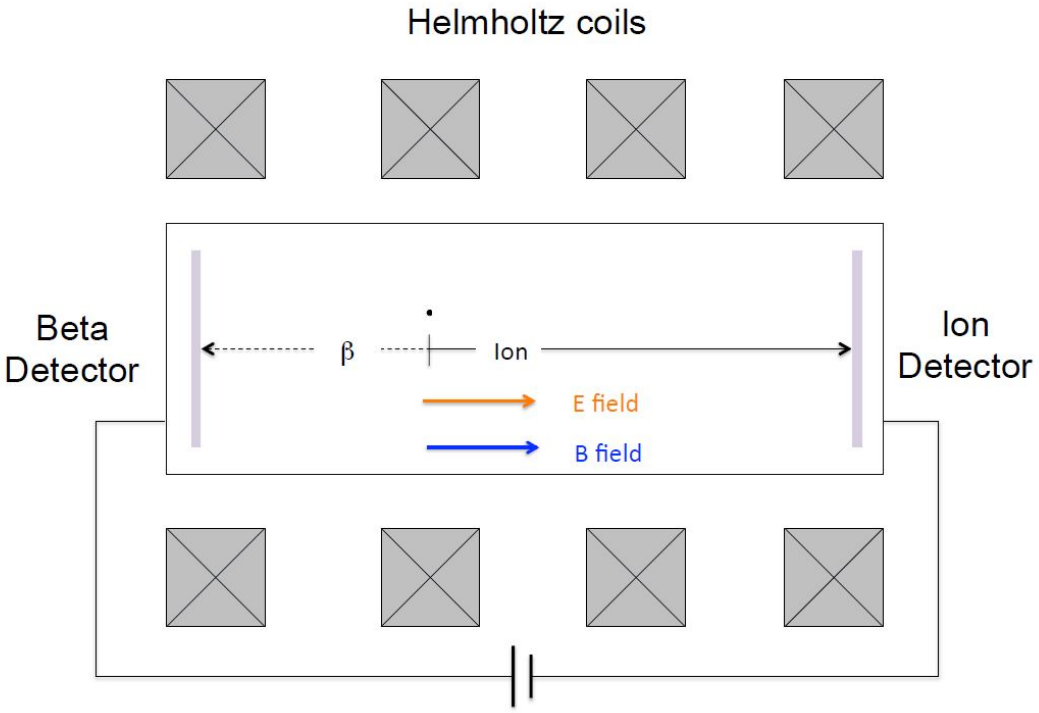

Figure A.1.: Schematic overview of the experimental setup of TRIMS: Ions and electrons caused by the β-decay of tritium are detected in coincidence. The solid line illustrates the direction of the ion while the dashed line corresponds to the movement of the electron. Figure adapted from [51].

discrepancy.
To do so, a good understanding of the electron energy resolution and therefore the properties of the employed silicon detector is required. Applying the software package KESS of Kassiopeia [61] introduced in chapter 3, corresponding simulations were carried out as will be highlighted in the following chapter.

B. Simulation of electrons in the silicon detector of the TRIMS experiment

As mentioned in chapter 3, the simulation software Kassiopeia primarily was written to fulfill the needs of the KATRIN collaboration. The silicon detector used in the TRIMS experiment for the detection of β-electrons however shows many similarities to the silicon detector employed in the KATRIN experiment.
The detection efficiency of a silicon detector strongly depends on the influence of its dead layer. Due to the fact that the energy of an incoming particle is not completely converted into voltage in the dead layer, the detected energy does not represent the energy of the electron. For this reason, it is crucial to investigate the influence of the dead layer on the initial energy of the electron. Therefore, simulations with regard to the energy loss behaviour of electrons within the dead layer were carried out.

B.1. Implementation of the TRIMS geometry in Kassiopeia

The geometry files in Kassiopeia have been designed to represent the experimental setup of the KATRIN experiment. Hence, the geometry of the TRIMS experiment had to be implemented before starting the corresponding simulations. An overview of the lines added to the configuration/XML-file is shown in figure B.2.
The TRIMS geometry is represented by four cylinders:

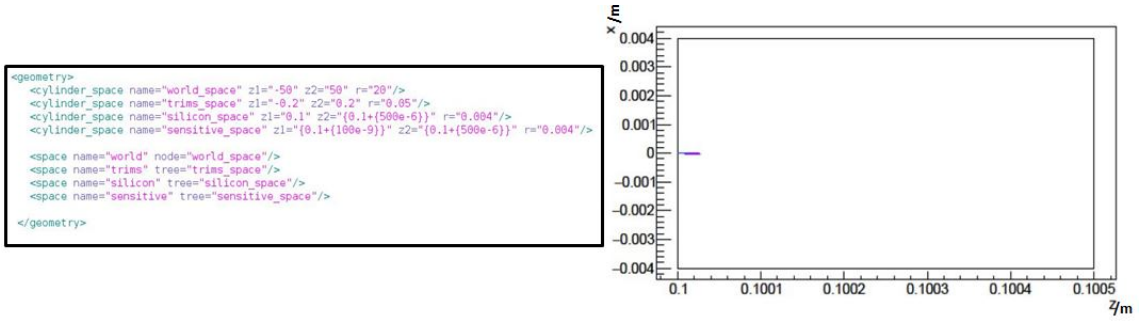

Figure B.2.: The TRIMS-geometry in Kassiopeia: Left: The geometry of TRIMS consists of four cylinder spaces in Kassiopeia. It is divided into the world space and the TRIMS space, which in turn includes the silicon space with its sensitive space. **Right:** A visualization of the silicon space geometry in Kassiopeia with one electron trajectory is shown.

- **World space:** The geometry of the experimental setup is confined in the World space.
- **TRIMS space:** The acceleration chamber of the TRIMS experiment has a length of approximately 0.2 m and a diameter of 0.1 m. The center of the vacuum chamber corresponds to z=0.
- **Silicon space:** The silicon space in Kassiopeia represents the Canberra PIPS [2] silicon detector with a radius of 0.004 m and a thickness of $500 \cdot 10^{-6}$ m.
- **Sensitive space:** The sensitive space corresponds to the active area of the silicon detector. The specified thickness of the dead layer amounts to $50 \cdot 10^{-9}$ m. However, it was decided to perform simulations with a specified thickness of $100 \cdot 10^{-9}$ m with a charge collection of 50 % in order to achieve a more accurate model based on [68]. The sensitive space starts at $z = 0.1 + 100 \cdot 10^{-9}$ m.

B.2. Simulation of electrons inside the silicon detector

In order to determine the electron energy loss due to the dead layer, event-based Monte Carlo simulations of electrons have been carried out for different energy ranges.
Electrons originating from β-decays of tritium possess energies up to 18.6 keV. As mentioned above, a potential difference of 60 kV is applied to accelerate the electrons to the detector. Hence, it is reasonable to carry out simulations for electrons in the range

$$E_{e^-,\mathrm{TRIMS}} \in [5; 80]\,\mathrm{keV}. \tag{B.1}$$

Targeting the investigation of the energy dependence behaviour of electrons in the dead layer, the energy range was split in 5 keV ranges. Therefore, 15 simulations were carried out in total where the electrons in each range were distributed homogeneously with regard to the energy.
Detailed simulation settings are shown in table B.1.

The following steps are performed in KESS in order to calculate the energy loss of a particle in the dead layer, where PDF describes the probability density function[3] which is pre-calculated for various kinetic energies in order to speed up the simulation:

1. Determination of the two closest PDFs $P_1(\Delta E, E)$ and $P_2(\Delta E, E)$ to kinetic energy E of the electron

[2] `http://www.canberra.com/products/detectors/pips-detectors.asp`
[3] The probability density function specifies the probability of the energy loss ΔE for an electron with kinetic energy E. Details can be found in [61].

Table B.1.: Settings for the simulation of electrons in the silicon detector of TRIMS: The parameter ranges and settings which were applied for the simulation of electron trajectories are shown. Each simulation was performed with 1000 electron.

Setting	**Value/Range**
Simulated events	10^4 events/energy range
initial energy	$E \in [5; 80]$ keV in 5 keV ranges
start position	z=0.1 m
initial radius	$r \in [0; 1 \cdot 10^{-6}]$ m
term backscattered	$z=0.1 - 2 \cdot 10^{-9}\, m$
term max steps	steps=$1 \cdot 10^6$
term radial escape	r=0.04 m
term stopped detector	energy=110 eV
Scattering	kess bethe fano, kess elastic
trajectory calculation method	kstraj linear inside silicon space kstraj exact inside vacuum, outside silicon space

2. Throw of a random number R with $R \in [0; 1]$
3. Estimation of two closest values of $P_1(\Delta E, E)$ to R
4. Interpolation of the two associated values for the energy loss $\Delta E \rightarrow$ Find out $\Delta E_1(R)$
5. Repetition of step 3 and step 4 for $P_2(\Delta E, E) \rightarrow \Delta E_2(R)$
6. Linear interpolation of $\Delta E_1(R)$ and $\Delta E_2(R) \rightarrow \Delta E(R)$

By employing ROOT, the Mean value of the energy loss in the dead layer was determined for each energy range. Figure B.3 shows the fraction of energy loss to the initial energy for 1000 events in the energy range of $E \in [5; 10]$ keV.
The calculation of the ratio was performed for each energy range. The mean values were estimated and plotted over the energy as illustrated in figure B.4.

It can be seen that the relative energy loss in the dead layer decreases with higher electron energies. In particular, the relative energy loss for the energy range $E \in [5; 10]$ keV is more than twice as high as for the following energy ranges. In the energy range $E \in [20; 25]$ keV, the energy loss decreases by about 5 % and increases afterwards again. Further simulations with higher statistics and performed in smaller energy ranges could provide a more detailed insight in this behaviour of the electrons.
Generally, the observation of the energy dependent decrease of the fractional energy loss is in accordance with expectations since the number of inelastic scattering processes depends on the dead layer thickness which stays constant for all energy ranges.

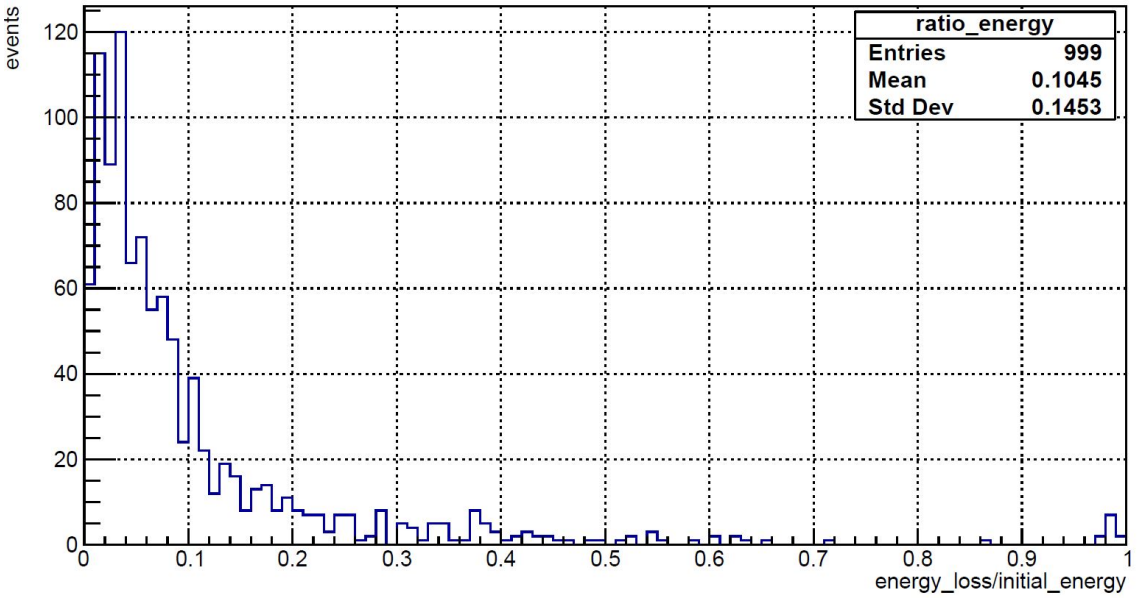

Figure B.3.: The ratio between the energy loss in the dead layer and the initial electron energy: The ratio between the energy loss in the dead layer and the initial energy was determined for each energy range by applying the software ROOT.

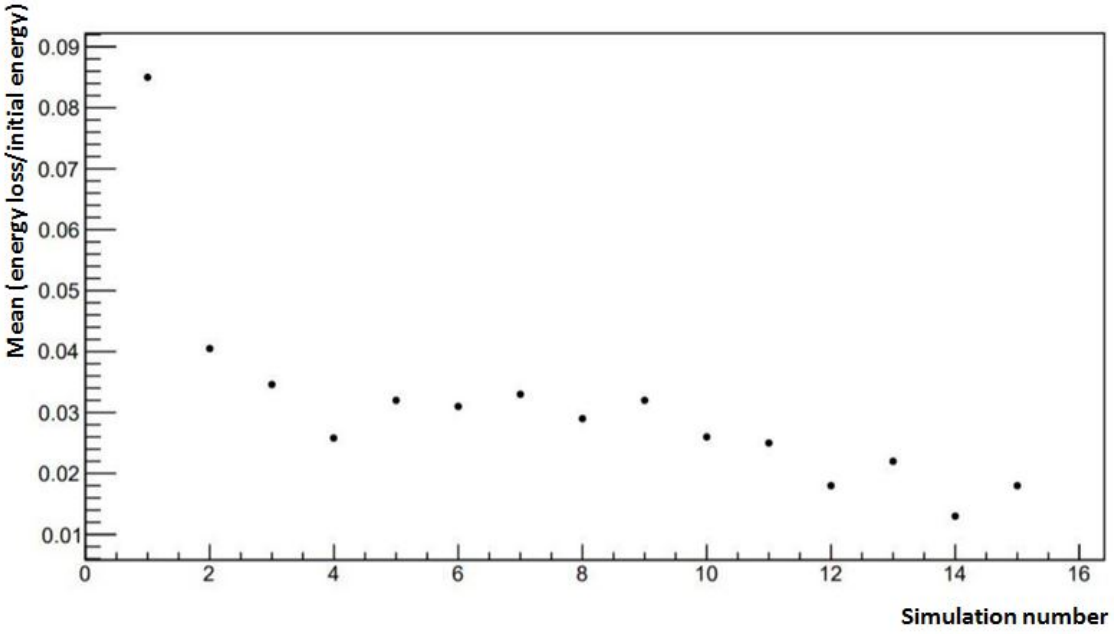

Figure B.4.: Relative energy loss of electrons for different energy ranges: The ratio between the energy loss of in the dead layer and the initial energy was determined for each energy range shown in table B.2. The mean value for each energy range was calculated via ROOT.

Table B.2.: Allocation of simulation number to energy range: Simulations were carried out for 5 keV ranges. The numbers represent the energy ranges in figure B.3.

Simulation number	**Energy range**
1	5-10 keV
2	10-15 keV
3	15-20 keV
4	20-25 keV
5	25-30 keV
6	30-35 keV
7	35-40 keV
8	40-45 keV
9	45-50 keV
10	50-55 keV
11	55-60 keV
12	60-65 keV
13	65-70 keV
14	70-75 keV
15	75-80 keV

C. Data sheet of Light Hammer

The Light Hammer 6 MARK II brings all of the benefits of microwave-powered UV curing to a 150 mm (6 in.) system.

Operating in the power class of 500 watts/inch (200 watts/cm), the Light Hammer 6 MARK II features two easy-to-service modular components: the microwave-powered irradiator and the solid-state power supply. At the heart of the microwave technology is the electrodeless bulb mounted in an elliptical reflector for focusing an intense strip of UV energy 53 mm (2.1 inches) below the face of the lamp.

Electrodeless Technology
The microwave-powered lamp and its electrodeless bulb technology have proven themselves over time and in hundreds of demanding applications. These long life bulbs are known for their stable performance, high intensity and low maintenance operation.

Popular Bulb Spectra Available
The standard bulb spectra are available: "H" spectral distribution is suited for clear-coats and varnishes; the "D" spectral distribution is popular and proven for inks and thick coatings or adhesives; and the "V" distribution is effective for UV curing white basecoats, through laminating materials and in other specialty applications.

Improved Cure
The ultimate benefit of the Light Hammer 6 MARK II is the achievement of higher degrees of conversion than is typically achieved with high ripple (AC) powered UV sources. (Patented)

Specifications: Light Hammer 6 MARK II

System Designations & Requirements

Available Input Voltages (50/60 Hz): 200 V–480 V ±10% auto-ranging.
System Ambient Operating Temperature: 0–50°C.
System Ambient Storage Temperature: -40°C–70°C.
Power Supply: LHP6 MARK II.
Altitude: 0–1,000 m.
Irradiator: I6 series.
Relative Humidity: 30–95% (non-condensing).
Mobility: Stationary, rack-mounted.
Environmental: Indoor use only.
Pollution Degree: 2.
Compliance: TÜV; CE.

Test Standards

Electrical Safety: EN 61010-1.
Emissions (CE): EN 55011 (CISPR-11) for Class A Group 2 device.
Immunity (CE): EN 61000-6-4; EN 61000-6-2; EN 61000-4-x.

Irradiator Models: I6P Series, I6S Series, I6 with Modular Blower (I6B)

Operating Voltage: Powered through the LHP6 MARK II power supply.
Exhaust: Recommend 130% of the nominal volume of cooling air.
Reflector Geometry: Semi-elliptical (with bulb at focus).
Mounting Position: Any angle.
Footprint: 168 mm (6.6 in.) x 168 mm (6.6 in.).
Focus Distance: 53 mm (2.1 in.) from face of lamp, for maximum irradiance.
Magnetron Output @ 100% Power: 184 W/cm (467 W/in.).
Bulb Spectra Types Available: D, H, V.
Cooling: Cooling recommended at 100% operation (rapid cycling mode and reduced cooling excluded).

- **I6P Series and I6S Series:** 3.7 m³/min. (132 scfm).
  Test point pressure: 0.9 kPa (3.7 in. H_2O).
- **I6B and I6B MARK II:** Integral.

Cooling Air Requirement Filtered:*

- **I6P Series (I6P1, I6P1LH):** 1.4 kPa (5.5 in. H_2O) (top air inlet).
  (I6P3, I6P3LH): 1.3 kPa (5.0 in. H_2O) (side air inlet).
- **I6S Series (I6S, I6SLH, I6SULC):** 1.3 kPa (5.0 in. H_2O) (side inlet).
  I6B and I6B MARK II: Integral.

NOTES:
*All I6 irradiator measurements assume 100% power and 100% duty cycle. If operating at different power levels or under rapid cycling conditions, please contact **Heraeus Noblelight** for the cooling air requirements.

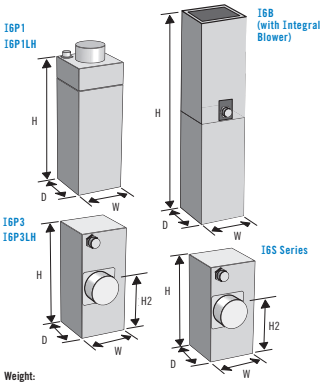

Weight:

- I6P1, I6P1LH: 9.7 kg (21.4 lbs.) (top air inlet).
- I6P3, I6P3LH: 9.1 kg (20.0 lbs.) (side air inlet).
- I6S, I6SLH, I6SULC: 10.8 kg (23.9 lbs.) (stainless steel housing).
- I6B: 13.1 kg (28.8 lbs.).
- I6B MARK II: 13.1 kg (28.8 lbs.).

LH6 MARK II – Power Supply Power Level Control Options

Method	Percent Control	Modes of Operation
DeviceNet™, Profibus®, EtherNet/IP™	1% steps	Remote/DeviceNet™, Profibus®, EtherNet/IP™ (additional module required)
4–20 mA input	1% steps, via master/slave operation	Remote/dry contact master/slave
0–10 V input	1% steps, via master/slave operation	Remote/dry contact master/slave
4-bit binary input	5% steps, via master/slave operation	Remote/dry contact master/slave
Front panel switched	1% steps, via master/slave operation	Local/front panel

Specifications subject to change without notice.

I6B MARK II Blower Specifications

Weight: Part of lamp unit: 13.1 kg (28.8 lbs.).
Max. Dimensions (W x D x H): Irradiator/blower: 168 mm x 168 mm x 757 mm (6.6 in. x 6.6 in. x 29.8 in.).
Operating Voltage: Powered through the LHP6B MARK II power supply.
Ambient Conditions: 45°C max. inlet temperature. 95% max. relative humidity, non-condensing.
Altitude: 0–1,000 m.
Performance: I6B MARK II blower delivers a minimum pressure of 900 (3.8 inches to the I6B MARK II irradiator test port. (Use non-swept reflectors only.).
Noise: 76 dBA @ 1 m.

Specifications subject to change without notice.

NOTE: The LH6B MARK II should be used in lightshields with unrestricted air flow. When a quartz plate assembly is used below the irradiator, a negative pressure exhaust system is required that eliminates back pressure at the base of the irradiator.

Legacy K6 Blower Specifications

NOTE: The K6 Blower is for Legacy systems. The LHP6B MARK II power supply is backward compatible with a legacy I6B Lamp system containing the K6 Blower.

Electrical: Powered through I6B irradiator.
Mechanical: Integral to I6B irradiator.
Noise: 78.5 dBA @ 1 m.
Filter: A replaceable polyester filter prefilters the cooling air entering the blower. Filters must be non-woven, bonded polyester fiber with a maximum continuous operating temperature of 250°F. The bonding agent must be flame and fungus retardant as well as moisture proof. The air velocity is 200–450 fpm. Replacement filters are available from **Heraeus Noblelight.**

Specifications subject to change without notice.

NOTE: The I6B should be used in lightshields with unrestricted air flow. When a quartz plate assembly is used below the irradiator, a negative pressure exhaust system is required that eliminates back pressure at the base of the irradiator.

LHP6 MARK II Power Supply

Weight: 18 kg (39 lbs.) (no blower control module) 20 kg (44 lbs.) with blower control module.
Dimensions (W x H x L): 419 mm x 217 mm x 777 mm with connector (16.5 in. x 8.5 in. x 30.6 in. with connector).
Cooling Air Flow: Air flow path: front to rear.
Input Voltages: 200 V–480 V (auto-ranging).
Mounting Position: Horizontal unit can be free standing, stacked, or rack mounted.
Line Power @ 100%: 5 kVA.
Clearance: Allow 305 mm (12 in.) clearance front and rear of the power supply for cooling air flow and cable connections.
Safety Interlocks: E-stop. External interlock (customer I/O). RF fault.
Mag. Current @ 100% Power: 840 mA/magnetron.
Mag. Current Output Accuracy: ±1%.
Output Range: 35% to 100%.
3-Phase: 50/60 Hz.
Max. Line Current: At 380–480 V: 7.25–5.8 (8.8–7.2 A with blower module installed). **At 200–240 V:** 13.3–11.1 A (17.1–14.0 A with blower module installed).
Stacking: 5 units maximum.
Enclosure Rating: IP20 (NEMA 1).
Front Panel Indicators/Controls: Lamp enable switch. USB port. OLED display unit with on/standby/off buttons and power level control buttons.
Rear Panel Connectors: J101: AC power input. J102: Master/slave.
J103: HV control. J104: Irradiator control. J105: RF detector.
J106: Customer I/O. J107: E-stop. J108: Optional blower.
J109/J110: Master/slave bus (option for LH6 legacy only).
J111: Optional comm bus.
Ventilation: Internal fans.
Filter: Polyurethane foam, 30 pores per inch (PPI).
Audible Noise Level: 65 dBA @ 1 m (at lamp off/reset).
Compliance: CE, TÜV.

Specifications subject to change without notice.

Contact your local Heraeus Noblelight office for an engineered solution for your specific requirements.

D. Parameter sets for ionization cross sections

Table D.3.: Ionization thresholds B_j, partitioning factors G_j and number of electrons N for different ionisation sub-shells in water vapour according to [63].

Shell j	B_j(eV)	N_j	G_j
$1a_1$	539.70	2	1.00
$2a_1$	32.20	2	0.52
$1b_2$	18.55	2	1.11
$3a_1$	14.73	2	1.11
$1b_1$	12.61	2	0.99

Table D.4.: Parameter set for total cross section from [62].

Parameter	Value
A	2.98
B	4.42
C	1.48
D	0.75
F	0

Functions with low and high energy parts $\mathrm{L}_1(\nu)$, $\mathrm{L}_2(\nu)$ of the differential cross section

$$\mathrm{L}_1(\nu) = \frac{\mathrm{C}_1\nu^{\mathrm{D}_1}}{1+\mathrm{E}_1\nu^{\mathrm{D}_1+4}}; \quad \mathrm{L}_2(\nu) = \mathrm{C}_2\nu^{\mathrm{D}_2}$$
$$\mathrm{H}_1(\nu) = \frac{\mathrm{A}_1\cdot\ln(1+\nu^2)}{\nu^2+\mathrm{B}_1/\nu^2}; \quad \mathrm{H}_2(\nu) = \frac{\mathrm{A}_2}{\nu^2}+\frac{B_2}{\nu^4} \tag{D.1}$$

Bibliography

[1] J.N. Abdurashitov, T.J. Bowles, M.L. Cherry, B.T. Cleveland, R. Davis Jr, S.R. Elliott, V.N. Gavrin, S.V. Girin, V.V. Gorbachev, T.V. Ibragimova, et al. Measurement of the solar neutrino capture rate by SAGE and implications for neutrino oscillations in vacuum. *Physical Review Letters*, 83(23):4686, 1999.

[2] S. Abe, T. Ebihara, S. Enomoto, K. Furuno, Y. Gando, K. Ichimura, H. Ikeda, K. Inoue, Y. Kibe, Y. Kishimoto, et al. Precision measurement of neutrino oscillation parameters with KamLAND. *Physical Review Letters*, 100(22):221803, 2008.

[3] Abe, K. et al. (T2K Collaboration). Observation of electron neutrino appearance in a muon neutrino beam. *Physical Review Letters*, 112:061802, 2014. doi:10.1103/PhysRevLett.112.061802.

[4] Abe, Y. et al. (Double Chooz Collaboration). Reactor $\overline{\nu}_e$ disappearance in the Double Chooz experiment. *Physical Review D*, 86:052008, 2012. doi:10.1103/PhysRevD.86.052008.

[5] N. Abgrall, Estanislao Aguayo, Frank T. Avignone, Alexander S. Barabash, F.E. Bertrand, M. Boswell, V. Brudanin, Matthew Busch, A.S. Caldwell, Y.-D. Chan, et al. The Majorana Demonstrator neutrinoless double-beta decay experiment. *Advances in High Energy Physics*, 2014, 2014.

[6] K.-H. Ackermann, M. Agostini, M. Allardt, M. Altmann, E. Andreotti, A.M. Bakalyarov, M. Balata, I. Barabanov, M. Barnabé Heider, N. Barros, et al. The GERDA experiment for the search of $0\nu\beta\beta$ decay in ^{76}Ge. *The European Physical Journal C*, 73(3):2330, 2013.

[7] Peter A.R. Ade, N. Aghanim, M. Arnaud, M. Ashdown, J. Aumont, C. Baccigalupi, A.J. Banday, R.B. Barreiro, J.G. Bartlett, N. Bartolo, et al. Planck 2015 results-XIII. Cosmological parameters. *Astronomy & Astrophysics*, 594:A13, 2016.

[8] Ade, P. et al. (Planck Collaboration). Planck 2013 results. XVI. cosmological parameters. *Astronomy and Astrophysics*, 571:66, 2014. doi:10.1051/0004-6361/201321591.

[9] Agostini, M. et al. (GERDA Collaboration). Results on neutrinoless Double-β decay of ^{76}Ge from phase i of the GERDA experiment. *Physical Review Letters*, 111:122503, 2013. doi:10.1103/PhysRevLett.111.122503.

[10] Aharmim, B. et al. (SNO Collaboration). Combined analysis of all three phases of solar neutrino data from the Sudbury Neutrino Observatory. *Physical Review C*, 88:025501, 2013. doi:10.1103/PhysRevC.88.025501.

[11] Ahn, J. K. et al. (RENO Collaboration). Observation of reactor electron antineutrinos disappearance in the RENO experiment. *Physical Review Letters*, 108:191802, 2012. doi:10.1103/PhysRevLett.108.191802.

[12] G. Alimonti, C. Arpesella, H. Back, M. Balata, D. Bartolomei, A. De Bellefon, G. Bellini, J. Benziger, A. Bevilacqua, D. Bondi, et al. The Borexino Detector at the Laboratori Nazionali del Gran Sasso. *Nuclear Instruments and Methods in Physics Research Section A: Accelerators, Spectrometers, Detectors and Associated Equipment*, 600(3):568–593, 2009.

[13] J.F. Amsbaugh, J. Barrett, A. Beglarian, T. Bergmann, H. Bichsel, L.I. Bodine, J. Bonn, N.M. Boyd, T.H. Burritt, Z. Chaoui, S. Chilingaryan, T.J. Corona, P.J. Doe, J.A. Dunmore, S. Enomoto, J. Fischer, J.A. Formaggio, F.M. Fränkle, D. Furse, H. Gemmeke, F. Glück, F. Harms, G.C. Harper, J. Hartmann, M.A. Howe, A. Kaboth, J. Kelsey, M. Knauer, A. Kopmann, M.L. Leber, E.L. Martin, K.J. Middleman, A.W. Myers, N.S. Oblath, D.S. Parno, D.A. Peterson, L. Petzold, D.G. Phillips II, P. Renschler, R.G.H. Robertson, J. Schwarz, M. Steidl, D. Tcherniakhovski, T. Thümmler, T.D. Van Wechel, B.A. VanDevender, S. Vöcking, B.L. Wall, K. L. Wierman, J.F. Wilkerson, and S. Wüstling. Focal-plane detector system for the KATRIN experiment. *Nuclear Instruments and Methods in Physics Research Section A: Accelerators, Spectrometers, Detectors and Associated Equipment*, 778:40–60, 2015. doi:10.1016/j.nima.2014.12.116.

[14] An, F. P. et al. (Daya Bay Collaboration). Observation of electron-antineutrino disappearance at daya bay. *Physical Review Letters*, 108:171803, 2012. doi:10.1103/PhysRevLett.108.171803.

[15] V.N. Aseev, A.I. Belesev, A.I. Berlev, E.V. Geraskin, A.A. Golubev, N.A. Likhovid, V.M. Lobashev, A.A. Nozik, V.S. Pantuev, V.I. Parfenov, et al. Upper limit on the electron antineutrino mass from the Troitsk experiment. *Physical Review D*, 84(11):112003, 2011.

[16] Ali Ashtari Esfahani et al. Determining the neutrino mass with cyclotron radiation emission spectroscopy—Project 8. *J. Phys.*, G44(5):054004, 2017. arXiv:1703.02037, doi:10.1088/1361-6471/aa5b4f.

[17] J.N Bahcall. Solar neutrinos: an overview. *Physics Reports*, 333-334(Supplement C):47 – 62, 2000. URL: http://www.sciencedirect.com/science/article/pii/S0370157300000156, doi:https://doi.org/10.1016/S0370-1573(00)00015-6.

[18] John N. Bahcall. Solar Neutrino Cross Sections and Nuclear Beta Decay. *Phys. Rev.*, 135:B137–B146, Jul 1964. URL: https://link.aps.org/doi/10.1103/PhysRev.135.B137, doi:10.1103/PhysRev.135.B137.

[19] G. Beamson, H.Q. Porter, and D.W. Turner. The collimating and magnifying properties of a superconducting field photoelectron spectrometer. *Journal of Physics E: Scientific Instruments*, 13(1):64, 1980.

[20] H.A. Bethe and R.E. Peierls. The neutrino. *Nature*, 133(3362), 1934.

[21] J. Chadwick. Intensitätsverteilung im magnetischen Spektrum der β-Strahlen von Radium B+C / The intensity of distribution in magnetic spectrum of β-Rays of Radium B+C. *Verhandl. Deutsch. phys. Ges.*, 16, 1914.

[22] GALLEX Collaboration. GALLEX solar neutrino observations: results for GALLEX IV. *Physics Letters B*, 447, no. 1-2:127–133, 1999. doi:10.1016/50370-2693(98)01579-2.

[23] Clyde L. Cowan Jr, F. Reines, F.B. Harrison, H.W. Kruse, and A.D. McGuire. *Detection of the free neutrino: a confirmation*. World Scientific, 1991.

[24] N. Trost et al. D. Furse, S. Groh. Kassiopeia: A Modern, Extensible C++ Particle Tracking Package. 2016.

[25] G. Danby, J-M. Gaillard, K. Goulianos, L. M. Lederman, N. Mistry, M. Schwartz, and J. Steinberger. Observation of High-Energy Neutrino Reactions and the Existence of Two Kinds of Neutrinos. *Phys. Rev. Lett.*, 9:36–44, Jul 1962. URL: https://link.aps.org/doi/10.1103/PhysRevLett.9.36, doi:10.1103/PhysRevLett.9.36.

[26] S. Dell'Oro, S. Marcocci, M. Viel, and F. Vissani. Neutrinoless double beta decay: 2015 review. *Adv. High Energy Phys.*, 2016:2162659, 2016. arXiv:1601.07512, doi:10.1155/2016/2162659.

[27] F. Di Capua. Recent results from the OPERA experiment. *Nuovo Cimento della Societa Italiana di Fisica. C, Geophysics and Space Physics*, 32(5-6):63–70, 2009.

[28] P. J. Doe et al. Project 8: Determining neutrino mass from tritium beta decay using a frequency-based method. In *Proceedings, 2013 Community Summer Study on the Future of U.S. Particle Physics: Snowmass on the Mississippi (CSS2013): Minneapolis, MN, USA, July 29-August 6, 2013*, 2013. URL: https://inspirehep.net/record/1255861/files/arXiv:1309.7093.pdf, arXiv:1309.7093.

[29] J. Ebert, M. Fritts, C. Gößling, T. Göpfert, D. Gehre, C. Hagner, N. Heidrich, T. Köttig, T. Neddermann, C. Oldorf, et al. Current status and future perspectives of the COBRA experiment. *Advances in High Energy Physics*, 2013, 2013.

[30] J. Barrett et al. Results of the first KATRIN SDS measurement phase. 2014.

[31] J.N. Bahcall et al. New solar opacities, abundances, helioseismology and neutrino fluxes. *The Astrophysical Journal Letters*, 621, no.1, 2005. doi:10.1086/428929.

[32] E. Fermi. Versuch einer theorie der β-Strahlen. *Zeitschrift für Physik*, 88(3–4):161–177, 1934. doi:10.1007/BF01351864.

[33] D.J. Fixsen. The temperature of the cosmic microwave background. *The Astrophysical Journal*, 707(2):916, 2009.

[34] Y. Fukuda, T. Hayakawa, K. Inoue, K. Ishihara, H. Ishino, S. Joukou, T. Kajita, S. Kasuga, Y. Koshio, T. Kumita, et al. Solar neutrino data covering solar cycle 22. *Physical Review Letters*, 77(9):1683, 1996.

[35] W.H. Furry. On transition probabilities in double beta-disintegration. *Physical Review*, 56(12):1184, 1939.

[36] T. F. Gallagher. Rydberg atoms. *Rep. Prog. Phys.*, 51:143–188, 1988. doi:10.1088/0034-4885/51/2/001.

[37] Thomas F. Gallagher. *Electric fields*, page 70–102. Cambridge Monographs on Atomic, Molecular and Chemical Physics. Cambridge University Press, 1994. doi:10.1017/CBO9780511524530.007.

[38] Gando, A. et al. (KamLAND-Zen Collaboration). Limit on neutrinoless $\beta\beta$-decay of ^{136}Xe from the first phase of KamLAND-Zen and comparison with the positive claim in ^{76}Ge. *Physical Review Letters*, 110:062502, 2013. doi:10.1103/PhysRevLett.110.062502.

[39] F. Glueck. Axisymmetric magnetic field calculation with zonal harmonic expansion. *Progress In Electromagnetics Research B*, 32, 2011. URL: http://www.jpier.org/pierb/pier.php?paper=11042108, doi:10.2528/PIERB11042108.

[40] M. Goldhaber, L. Grodzins, and A. W. Sunyar. Helicity of Neutrinos. *Phys. Rev.*, 109:1015–1017, Feb 1958. URL: https://link.aps.org/doi/10.1103/PhysRev.109.1015, doi:10.1103/PhysRev.109.1015.

[41] Stefan Groh. *Untersuchung von UV-laser induziertem Untergrund am KATRIN Vorspektrometer*. PhD thesis, Diploma thesis, Karlsruhe Institute of Technology, 2010.

[42] Fabian Harms. *Characterization and Minimization of Background Processes in the KATRIN Main Spectrometer*. PhD thesis, Karlsruher Institut für Technologie (KIT), 2015. URL: http://nbn-resolving.org/urn:nbn:de:swb:90-500274.

[43] Urs Hollenstein, Robert Seiler, Hansjürg Schmutz, Markus Andrist, and Frédéric Merkt. Selective field ionization of high Rydberg states: Application to zero-kinetic-energy photoelectron spectroscopy. *The Journal of Chemical Physics*, 115(12):5461–5469, 2001.

[44] Arkadiusz Hypki. BEANS-a software package for distributed Big Data analysis. *arXiv preprint arXiv:1603.07342*, 2016.

[45] I. I. Ryabtsev et al. I. I. Beterov, D. B. Tretyakov. Ionization of Rydberg atoms by blackbody radiation. *New J. Phys.*, 11:013052, 2009. doi:10.1088/1367-2630/11/1/013052.

[46] S. Jonsell, A. Saenz, and P. Froelich. Neutrino-mass determination from tritium β decay: Corrections to and prospects of experimental verification of the final-state spectrum. *Phys. Rev. C*, 60:034601, Jul 1999. URL: https://link.aps.org/doi/10.1103/PhysRevC.60.034601, doi:10.1103/PhysRevC.60.034601.

[47] M. Klein, F. Glück, and KATRIN collaboration. Tritium ion blocking and detection in the KATRIN experiment. *Journal of Physics: Conference Series*, 888(1):012073, 2017. URL: http://stacks.iop.org/1742-6596/888/i=1/a=012073.

[48] K. Kodama et al. Observation of tau neutrino interactions. *Phys. Lett.*, B504:218–224, 2001. arXiv:hep-ex/0012035, doi:10.1016/S0370-2693(01)00307-0.

[49] C. Kraus, B. Bornschein, L. Bornschein, J. Bonn, B. Flatt, A. Kovalik, B. Ostrick, E.W. Otten, J.P. Schall, T. Thümmler, and C. Weinheimer. Final results from phase II of the Mainz neutrino mass search in tritium β decay. *The European Physical Journal C - Particles and Fields*, 40(4):447–468, 2005. doi:10.1140/epjc/s2005-02139-7.

[50] P. Kruit and F.H. Read. Magnetic field paralleliser for 2π electron-spectrometer and electron-image magnifier. *Journal of Physics E: Scientific Instruments*, 16(4):313, 1983.

[51] R. G. H. Robertson L. I. Bodine, D. S. Parno. Assessment of molecular effects on neutrino mass measurements from tritium β-decay. *Physical Review C*, 91, 035505, 2015. doi:10.1086/428929.

[52] Andrew Liddle. *An Introduction to Modern Cosmology*. John Wiley & Sons, 2015.

[53] S. Lukic, B. Bornschein, G. Drexlin, F. Glück, O. Kazachenko, M. Schöppner, Ch. Weinheimer, and MCR Zoll. Ion source for tests of ion behavior in the Karlsruhe tritium neutrino experiment beam line. *Review of Scientific Instruments*, 82(1):013303, 2011.

[54] E. Majorana. Teoria simmetrica dell'elettrone e del positrone. *Il Nuovo Cimento (1924-1942)*, 14(4):171, 1937.

[55] R. Melhem. Parallel gauss-jordan elimination for the solution of dense linear systems. *Parallel Computing*, 4(3):339–343, 1987.

[56] S.P. Mikheyev and A. Yu Smirnov. Resonant amplification of ν oscillations in matter and solar-neutrino spectroscopy. *Il Nuovo Cimento C*, 9(1):17–26, 1986.

[57] W.E.F. Pauli, R. Kronig, and V.F. Weisskopf. *Collected scientific papers*. Interscience, New York, NY, 1964. Offener Brief an die Gruppe der Radioaktiven bei der Gauvereinstagung zu Tübingen (datiert 4. Dez. 1930).

[58] Bruno Pontecorvo. Neutrino experiments and the problem of conservation of leptonic charge. *Sov. Phys. JETP*, 26(984-988):165, 1968.

[59] G. Racah. Sulla simmetria tra particelle e antiparticelle. *Il Nuovo Cimento (1924-1942)*, 14(7):322–328, 1937.

[60] F. Reines and C.L. Cowan. Detection of the free neutrino. *Physical Review*, 92:830–831, 1953. doi:10.1103/PhysRev.92.830.

[61] Pascal Renschler. *KESS - A new Monte Carlo simulation code for low-energy electron interactions in silicon detectors*. PhD thesis, Karlsruher Institut für Technologie (KIT), 2011. URL: http://digbib.ubka.uni-karlsruhe.de/volltexte/1000024959.

[62] M. Eugene Rudd, Y.-K. Kim, Don H. Madison, and Jean W. Gallagher. Electron production in proton collisions: total cross sections. *Reviews of modern physics*, 57(4):965, 1985.

[63] Millard E. Rudd, Y.-K. Kim, Don H. Madison, and Timothy J. Gay. Electron production in proton collisions with atoms and molecules: energy distributions. *Reviews of modern physics*, 64(2):441, 1992.

[64] E. Rutherford. The Magnetic and Electric Deviation of the Easily Absorbed Rays from Radium. pages 177,187, 1903.

[65] Magnus Schlösser. *Accurate calibration of the Raman system for the Karlsruhe Tritium Neutrino Experiment*. PhD thesis, Karlsruher Institut für Technologie (KIT), 2013.

[66] M. Sisti, C. Arnaboldi, C. Brofferio, G. Ceruti, O. Cremonesi, E. Fiorini, A. Giuliani, B. Margesin, L. Martensson, A. Nucciotti, et al. New limits from the milano neutrino mass experiment with thermal microcalorimeters. *Nuclear Instruments and Methods in Physics Research Section A: Accelerators, Spectrometers, Detectors and Associated Equipment*, 520(1):125–131, 2004.

[67] The EXO-200 Collaboration. Search for majorana neutrinos with the first two years of EXO-200 data. *Nature*, 510:229–234, 2014. doi:10.1038/nature13432.

[68] B. Wall. *Karlsruhe Tritium Experiment: Detector System Commissioning and In-Situ PIN-Diode Array Dead-Layer Measurement*. PhD thesis, University of Washington, 2013.

[69] C.F. v. Weizsäcker. Zur Theorie der Kernmassen. *Zeitschrift für Physik A Hadrons and Nuclei*, 96(7):431–458, 1935.

[70] C.-S. Wu, E. Ambler, R.W. Hayward, D.D. Hoppes, and R Pl Hudson. Experimental test of parity conservation in β- decay. *Physical review*, 105(4):1413, 1957.

[71] Kai Zuber. *Neutrino Physics*. CRC press, 2011.

Acknowledgement

An dieser Stelle möchte ich meinen Dank denjenigen, die zum Gelingen dieser Arbeit beigetragen haben, zum Ausdruck bringen.

Allen voran gilt mein Dank Prof. Dr. Drexlin, der mir zusätzlich zur Bereitstellung dieser Masterarbeit in einem interessanten Themengebiet beim KATRIN-Experiment einen unvergesslichen Auslandsaufenthalt in den USA ermöglicht hat. Zugleich möchte ich mich bei Katharina Fischer für das Erledigen sämtlicher organisatorischer Angelegenheiten bedanken.

Bei Prof. Dr. Husemann bedanke ich mich für die Übernahme des Korreferats sowie die zeitnahe Beantwortung meiner Fragen diesbezüglich.

Ein besonderer Dank gilt Dr.Florian Fränkle für die exzellente Betreuung während des gesamten vergangenen Jahres, die neben zahlreichen Anregungen, der Diskussionsbereitschaft auf physikalischer Ebene, das Korrekturlesen dieser Arbeit auch die Einweisung in das Programmieren in ROOT sowie in die wissenschaftliche Arbeitsweise umfasst und somit zu der Entwicklung einer selbstständigen Arbeitsweise maßgeblich beigetragen hat.

Special thanks goes to Diana Parno for giving me the opportunity to join her group at Carnegie Mellon University for seven weeks and thus allowing me to gain insight into research beyond the KATRIN experiment. In particular, I'd like to thank her for her very supportive guidance, advices and encouragements.
Thanks also goes to Luke Kippenbrock for his support and helpful information on the implementation of cross sections in Kassiopeia.

Des Weiteren bedanke ich mich bei Nikolaus Trost für die schrittweise Einführung in Kassiopeia und Dr. Jan Behrens für die ausführliche Beantwortung hinsichtlich der Tracking-Verfahren. Zugleich möchte ich mich bei Marco Deffert und Dr. Daniel Hilk bedanken, die mir die Geometrien in Kassiopeia nahegelegt haben.

Ein großer Dank gilt Manuel Klein und Dr. Ferenc Glück für die aufschlussreichen Diskussionen, die mir den Zusammenhang zwischen Messungen und Simulationen verdeutlicht haben.

Außerdem danke ich Lutz Schimpf, Michael Nieslony und Fabian Block für die hilfreichen Tipps für ROOT und Git.

Bei der gesamten KATRIN-Arbeitsgruppe möchte ich mich für die angenehme, abwechslungsreiche und zugleich produktive Arbeitsatmosphäre bedanken.

Mein letzter Dank gilt meinen Eltern, die mich während der gesamten Studienzeit uneingeschränkt unterstützt haben.